2007

Synthesis, characterization, and applications of CVD micro- and nanocrystalline diamond thin films

Zhenqing Xu
University of South Florida

Synthesis, Characterization, and Applications of CVD Micro- and Nanocrystalline Diamond Thin Films

by

Zhenqing Xu

A dissertation submitted in partial fulfillment
of the requirements for the degree of
Doctor of Philosophy
Department of Mechanical Engineering
College of Engineering
University of South Florida

Major Professor: Ashok Kumar, Ph.D.
Rajiv Dubey, Ph.D.
Leonid C. Lev, Ph.D.
Frank Pyrtle, Ph.D.
Sarath Witanachchi, Ph.D.

Date of Approval:
November 03, 2006

Keywords: chemical vapor deposition, cutting tools, WC-Co, biosensor, nanowires

DEDICATION

This dissertation is dedicated to my parents, Mr. Qi Xu and Mrs. Ping Liu, and all my family members who always support me.

ACKNOWLEDGEMENTS

I would like to express my gratitude to several people who have helped me throughout my research work, without their assistance this work would not have been possible. First of all I wish to thank my advisor, Dr. Ashok Kumar, for his sponsorship and guidance throughout this research. I would like to thank all committee members, Dr. Rajiv Dubey, Dr. Frank Pyrtle and Dr. Leonid Lev, for their time and valuable advice.

I wish to acknowledge all research scientists and staff members in the Materials & Processes Lab, GM R&D center, including Dr. Y.T. Cheng, Mr. M. Lukitsch, Mr. A Waldo, and Mr. C.A. Wong for their support. Appreciation goes to all my group members and in particular Dr. Arun Siker, Dr. Arun Kumar, Dr. Makoto Hirai, Mr. S. Jeedigunta, and Mr. S. Mudhivathi for their suggestion and contribution to this thesis. I wish to acknowledge Dr. Jay Banerjee from University of Puerto Rico, who has been very helpful during his sabbatical year in USF.

Most of all, I would like to thank my parents for their encouragement, persistence support and love, without which I would not have been able to be where I am today. I wish to thank my grandparents, family members and all my friends who support and help me all the time.

This work was supported by USF-GM project #2105-099LO and NSF NIRT grant # ECS 0404137.

TABLE OF CONTENTS

LIST OF TABLES

LIST OF FIGURES

SYNTHESIS, CHARACTERIZATION, AND APPLICATIONS OF CVD MICRO- AND NANOCRYSTALLINE DIAMOND THIN FILMS

Zhenqing Xu

ABSTRACT

In this thesis, a systematic study has been carried out on the synthesis, characterization and applications of microcrystalline diamond (MCD) and nanocrystalline diamond (NCD) thin films deposited by the chemical vapor deposition (CVD) method. Firstly, an overview of diamond films synthesized from carbon-containing gas plasmas is presented. A parameter study was performed to grow diamond thin films. The transition from micro- to nanocrystallinity of diamond grains was achieved by controlling the Ar/Hydrogen gas ratio. The nanocrystallinity is the result of a new growth mechanism which involves the insertion of carbon dimmer into carbon-carbon and carbon-hydrogen bonds. Secondly, characterization of diamond films has been carried out by different techniques including electron microscopy, near edge X-ray absorption fine structure (NEXAFS), nanoindentation, and Raman spectroscopy. Unique properties of NCD, compared to those of MCD grown by conventional hydrogen rich plasma, have been observed and investigated. Thirdly, various applications of diamond films are discussed: a). Well-adhered MCD coatings have been deposited on WC-Co substrates with proper surface pretreatment. A diffusion barrier Cr/CrN/Cr was deposited on the cemented carbide substrate and the

substrate was short peened with 150 micron friable diamond powders to achieve higher nucleation density and stronger adhesion strength; b). A nitrogen doped NCD based biosensor was fabricated for glucose sensing. Carboxyl functional group and conducting polymer (polyaniline) have been utilized respectively to electrochemically functionalize the diamond surface. A linear response to glucose concentration has been obtained from the electrode with good sensitivity and stability; c). A novel approach to synthesize NCD wires has been developed for the first time. The NCD coating was successfully coated on Si nanowires (SiNWs) to form NCD wire with diameter around a few microns. This study opens a whole new area for applications based on diamond wires such as neural transmission electrodes, field emission emitters, and electrochemical electrodes with improved properties.

CHAPTER 1:

INTRODUCTION

1.1 Properties of Diamond

Diamond has been in an extremely important position for both scientists and the public at large. For ordinary people, the gemstones mean wealth and myth. To the scientists, because of its wide range of extreme properties, diamond is so impressive that research groups all over the world are doing different studies on the diamond. Sir Isaac Newton was the first to propose that diamond was an organic material. Then it was found by Smithson Tennant that diamond, graphite and coal were the same elements. The structure of these materials was then characterized after the invention of X-rays and the formulation of Bragg's law. It was discovered that carbon has three different structures: cubic, hexagonal and amorphous (*1*).

Though the initial work in the synthesis of diamond at low temperature and low pressure was carried out in 1960s (*2, 3*), the worldwide interest of diamond was triggered by a Japanese group who published several methods for diamond deposition on a non-diamond substrate at high rates (*4*). Almost 50 years ago, the industrial diamond was synthesized commercially using high-pressure high-temperature (HPHT) techniques, in which diamond is crystallized from metal solvated carbon at pressure ~50-100 kbar and temperature ~1800-2300 K. World interest in diamond has been further increased by the much more recent discovery that it is possible to produce polycrystalline diamond films

or coatings, by a wide variety of chemical vapor deposition (CVD) techniques using, as process gases, nothing but hydrocarbon gas (typically methane) in an excess of hydrogen. This CVD diamond can show mechanical, tribological, and even electronic properties comparable with those of natural diamond. There is currently much optimism that will prove possible to scale CVD methods to the extent that they will provide an alternative way to the traditional HPHT methods for producing diamond abrasives and heat sinks. Moreover, the possibility of coating large surface areas with a continuous film of diamond will open up whole new ranges of potential applications for the CVD methods. So with the development of CVD technology the diamond films can be successfully synthesized and used in a variety of fields from electronic to optical and mechanical applications.

Diamonds are exclusively of the face-centered diamond cubic structure, as shown in Figure 1.1. The structure of diamond unit contains eight corner atoms (shown in black), six face-center atoms (shown in light blue), and four other atoms (shown in gray). These gray atoms are from adjacent interpenetrating lattices and are spaced on quarter of a cube diagonal from the former. Every carbon atom is tetrahedrally coordinated to four other carbon atoms via σ bonds emanating from sp^3 hybrid atomic orbital. The four (111) directions in cubic diamond are in the bond directions. The lattice can be viewed as layers of six-membered saturated carbon rings stacked in an ABC ABC ABC…… sequence along all three (111) directions. Each six-membered ring is in the conformation as the "chair". In the cubic form, the layers of chair are joined by staggered bonds. In any (111) direction the lattice constant is 3.65 Å and the bond length is 1.54 Å (*1*).

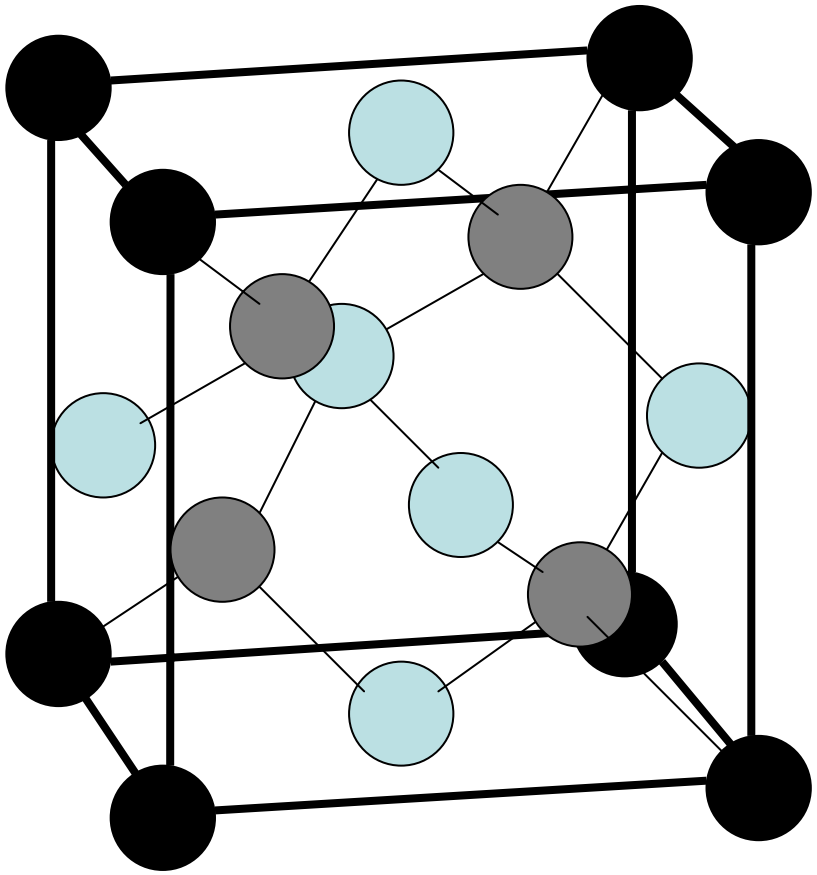

Figure 1.1: Face-centered cubic structure of diamond crystal.

As Table 1.1 shows, most of the diamond properties are the best; it is the hardest known bulk material, has the lowest coefficient of thermal expansion (CTE), is chemically inert and wear resistant, offers low friction, has high thermal conductivity, is electrically insulating and optically transparent from the ultra-violet (UV) to the far infrared (IR). Given these unique properties, it should come as no surprise to learn that diamond already finds use in many diverse applications including not only electrical but also mechanical and thermal applications. For example; it can be used as a heat sink, as an abrasive, and as inserts and/or wear-resistant coatings for cutting tools.

Table 1.1: Some of the outstanding properties of diamond.

Extreme mechanical hardness (~90 GPa).
Highest known value of thermal conductivity at room temperature (2 x 10^3 W/m/ K).
Strongest known material, highest bulk modulus (1.2 x 10^{12} N/m^2), lowest compressibility (8.3 x 10^{-13} m^2/ N).
Thermal expansion coefficient at room temperature (0.8 x 10^{-6} K) is comparable with that of invar.
Broad optical transparency from the deep UV to the far IR region of the electromagnetic spectrum.
Good electrical insulator (room temperature resistivity is ~10^{16} W cm).
Diamond can be doped to change its resistivity over the range 10-10^6 W cm, thus becoming a semiconductor with a wide bad gap of 5.5 eV.
Biologically compatible.
Very resistant to chemical corrosion.

The coefficient of friction (COF) of the natural diamond surface in air at 300K is approximately 0.1 which is equivalent to that of Teflon. Note that the coefficient of friction is a ratio between the magnitude of maximum frictional force and the magnitude of normal thrust. Optical properties include the index of refraction and optical absorption at a given wavelength and temperature.

The reflexive index of diamond is about 2.41-2.44. Due to the fact that diamond is transparent to both visible and infrared radiation, is abrasion resistant, is a good heat

conductor and is resistant to the chemical corrosion and radiation damage, it is considered as an excellent window and lens materials as well a protective coating for these materials.

Diamond is resist to all the acids, even at high temperatures. Due to this unique property, diamond can be used as a good corrosion resistant coating. However, diamond can be etched by fluxes of caustic alkalis, various crystals and metals.

As a semiconductor, the properties of diamond (expect for electron mobility) are virtually unexcelled. Table 1.2 shows the comparisons of the electrical properties among three different semiconductors.

Table 1.2: Electrical properties comparisons between diamond, silicon, and GaAs.

Property	Diamond	Silicon	GaAS
Band gap (eV)	5.4	1.1	1.4
Electron mobility (cm^2/volt-sec)	2,000	1,500	8,500
Hole mobility(cm^2/volt-sec)	1,800	600	400
Breakdown V/cm$*10^6$	10	5	6
Resistivity (ohm-cm)	1016	103	109
Dielectric function (eV)	5.7	11	12.5

Obviously, given its many unique properties it is possible to envisage many other potential applications for diamond as an engineering material, but progress implementing many such ideas has been hampered by the comparative scarcity of natural diamond. Moreover, to synthesize large area diamond thin films with smoothness and uniformity, it

becomes the most challenging part for worldwide researchers and scientists to use diamond in industrial applications.

1.2 Motivation of this Research

Diamond has some of the most extreme physical and chemical properties of any material, yet its practical use in science or engineering has been limited due its expense and difficulty to synthesis. With the recent development of techniques for depositing thin films of diamond (both MCD and NCD) on a variety of substrate materials, we now have the ability to develop diamond based research in many new and exciting applications. However, despite the rapid progress made in the past 10 years in the science and technology of diamond, the commercialization of this amazing material is still in its infancy.

There are some devices already in the marketplace, such as diamond heat spreaders, windows, cutting tools, and surface acoustic wave (SAW) filters. With the successful synthesis of nanocrystalline diamond which has extreme smoothness and ability to form a conformal coating for as thin as a couple hundred nanometers, we can expect to see diamond films appearing in many more applications, especially in micro-/nanomechanical electrical systems (MEMS/NEMS) in the next few years. Moreover, due to the development of biotechnology and the biocompatible nature of diamond film, the control and manipulation of the surface chemistry of NCD is essential in tailoring its surface properties for specific applications such as hard wear coatings, cold-cathode electron sources, chemical and biological sensing, and implantable biomedical devices. Therefore, in this thesis, diamond thin films will be synthesized, characterized, and

especially applied for different applications from wear resistant cutting tool coatings to electrochemical electrodes and biosensors. The potential of NCD based bio/organic-inorganic interfaces for biomedical implants and electrochemical biosensing applications will be discussed.

1.3 Organization of this Thesis

This thesis will report on the synthesis, characterization, and some applications of CVD deposited micro- and nanocrystalline diamond thin films. The research work done in this dissertation is divided into six main chapters. Chapter two will explain briefly about the chemical vapor deposition method and provide a literature review of the growth mechanism of both MCD and NCD films and the existing applications of these films. The transition of diamond crystal size from micro to nano will be explained and discussed in chapter three. Chapter three will also discuss the characterization work done on diamond films including electron microscopy, Raman spectroscopy, nanoindentation, etc. Three different applications of diamond films will be introduced in the following three chapters. Chapter four will propose a surface pretreatment method to deposit adherent MCD coating on WC-Co substrate for dry machining applications. Chapter five will explain a surface functionalization method to modify nitrogen doped NCD electrode for glucose detection via electrochemical setup. Chapter six will introduce a novel approach to fabricate NCD wires. Finally, chapter seven will summarize the work in this research and as well as discuss future work in this field.

CHAPTER 2:

BACKGROUND AND LITERATURE REVIEW

2.1 Overview of Chemical Vapor Deposition

As diamond is purely carbon, diamond growth could conceptually be affected by adding one carbon atom at a time to an initial template, so that a tetrahedrally bonded carbon network (diamond) can be formed. The low cost of the equipment and energy is the main advantage of this method since it can be accomplished at lower pressures technique. In essence, this is the logic behind the experiments of Derryagin (*3*) and Eversole (*5*). In these experiments, thermal deposition of carbon containing gases at less than 1 atmosphere pressure was used to grow diamond on natural diamond crystals heated to 900 °C. The rate of growth in such early CVD experiments was very low. Graphite was also co-deposited with the diamond.

An improvement was made by Angus *et al.* (*2*) who demonstrated that atomic hydrogen could etch graphite rather than diamond. Angus was also able to incorporate boron into diamond during growth, giving it semi conduction properties. Subsequent Russian work extended the possibilities of vapor phase diamond growth by showing that diamond could be grown on non-diamond surfaces (*3*). Japanese researchers at the National Institute for Research in Inorganic Materials (NIRIM) were able to bring all these findings together in 1981 by building a "hot filament" reactor in which good quality films of diamond could be grown, on non-diamond substrates, at significant rates (~1

μmh^{-1}) (*6*). The system operated using a few percent CH_4 in H_2 at 20 Torr (0.026 atm) pressure. Another method was also reported for growing diamond films in a "microwave plasma" reactor in the following years (*7*). These discoveries led to worldwide research interest in CVD diamond from the mid 1980s, in both industry and academic, which continues to the present day. Numerous methods for diamond film growth have been developed since then, such as D.C. Plasma, Radio Frequency (RF) Plasma, Microwave Plasma jet, Electron Cyclotron Resonance (ECR), Microwave Plasma, and also the combustion flame synthesis (*1*).

A tentative ternary carbon allotropy diagram based on carbon valence bond hybridization is shown in Figure 2.1 (*8*). We consider diamond, graphite, fullerenes, and carbyne as four basic carbon forms. The classification is based on the types of chemical bonds in carbon, including three bonding states corresponding to sp^3 (diamond), sp^2 (graphite), and sp (carbine) hybridization of the atomic orbitals. All other carbon forms are so called transitional forms such as diamond like carbon, fullerenes and nanotubes. The inorganic carbon family consisting of these four members has also been classified by Inogaki (*9*). The scheme suggested by Inogaki demonstrates interrelations between organic/inorganic carbons.

It is widely known that diamond is metastable while graphite is the most stable carbon form at the macroscale. Very interesting transformation between carbon forms at the nanoscale had been discovered in the mid-1990s. It was found that nanodiamond particles could be transformed to carbon onions after annealing at around 1300 to 1800 K (*10*). Moreover, carbon onions could be transferred to nanocrystalline diamond under electron irradiation (*11*). The phase diagram of carbon has been reconsidered several

times and the recent version is shown in Figure 2.2. It includes some of the recently observed phase transitions such as rapid solid phase graphite to diamond conversion, fast transformation of diamond to graphite, etc (*12*).

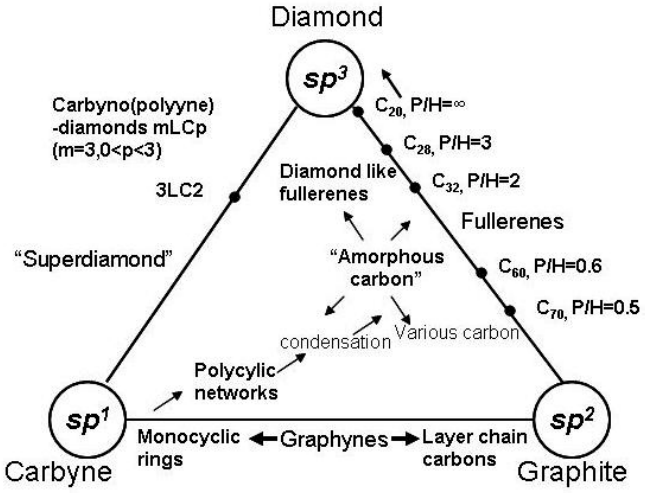

Figure 2.1: Ternary "phase" diagram of carbon allotropes. P/H corresponds to the ratio of pentagonal/hexagonal rings (*8*).

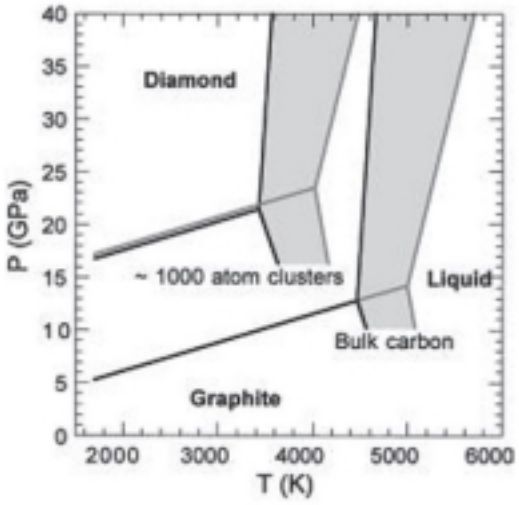

Figure 2.2: Approximate phase diagram for 1000 atom carbon clusters. Shadowed region corresponds to estimated uncertainties in location of equilibrium lines derived from available experimental data (*12*).

Most of the methods for CVD diamond share the same characteristics (*13*):

a) A gas phase must be activated, either by a high temperature or by plasma.

b) The gas phase must contain carbon-containing species such as hydrocarbon, alcohol, carbon dioxide or carbon monoxide.

c) A sufficiently high concentration of a species that etches graphite and suppresses gaseous graphite precursors (e.g., polycyclic aromatic hydrocarbons) must be provided. The atomic hydrogen is most commonly used. However, additional "anti-graphite" species have been proposed, including H_2, OH, O_2.

d) The substrate surface must be pretreated to support the nucleation and growth of diamond from the vapor phase. This means that any catalysts that promote formation of graphite could not exit on the substrates surface and the surface should be at or near the solubility limit for carbon so that it support the precipitation of diamond on the surface instead of the diffusion of carbon.

e) A driving force must exist to transport the carbon-beating species form the gas phase to the surface of the substrate. In most CVD method, the temperature gradient is used to be the driving force for the motion of diamond-producing species via diffusion because the activated gas phase is typically much hotter that the substrate surface.

f) The ability to produce a large variety of diamond films and coatings on different materials in either a crystalline or a vitreous form is the main reason why the CVD method is the most popular diamond growth method.

The microwave plasmas were first used for diamond synthesis in 1982 at National Institute for Research in Inorganic Materials (NIRIM), Japan. Because of its simplicity,

flexibility and low cost, the microwave plasma enhanced CVD (MPECVD) system is the most widely used reactor among all of the diamond deposition approaches. In order to explain the operation of such reactor a brief explanation of microwave propagation in waveguides will be given as basic knowledge of how to operate the microwave plasma reactor. The whole system includes the microwave plasma generator, the waveguide and tuning, the vacuum and the pump, the mass flow system, the substrate heater, the temperature readout system and the exhaust system will be introduced in the following paragraph. Microwaves are nothing but the electromagnetic radiation. So we can use the wave equations and reflective boundary (waveguide) conditions to form an analogue of the particle (wave) in a box problem. The solution of this problem is to provide an integer number of half wavelengths into the box. So, as the result, a spatially repeating electromagnetic field pattern can produce the waveguide. Hence the electric field strength E and the magnetic field strength B vary periodically along the waveguide. A microwave frequency of 2.45 GHz (that used by microwave ovens) is most commonly used in CVD reactors. However the 915 MHz reactors are now becoming more attractive because that the lower frequency allows reactor size to be increased.

Unfortunately, in the NIRIM-type reactor, the substrate temperature cannot be independently controlled by changing the plasma parameters because the substrate is immersed in the plasma. In order to solve this problem, an 'ASTeX'-type reactor is designed by a commercial manufacturer of plasma systems based in the US. By using this design, the plasma inside the chamber can be generated above the substrate. Hence, we can control the substrate temperature independently without the effect of the plasma heating on the coating surface.

The ASTeX–type reactor uses a microwave generator and rectangular waveguide, with a mode converter to convert the transverse electric mode in the rectangular waveguide to a transverse magnetic mode in a cylindrical waveguide (the reactor vessel). A moveable antenna maximizes energy coupling between the two-waveguide sections. Generation of the plasma occurs by the same mechanisms as discussed above for the NIRIM-type reactor, in the region(s) where the local electric field strength is highest. The ASTeX-type reactor is the most common microwave plasma CVD reactor type encountered. Of course, in reality, reactors are much more complex than simple cylinders due to the presence of service ports, welds, diagnostic probes, etc. Figure 2.3 shows the schematic drawing of the ASTeX-type MPECVD reactor.

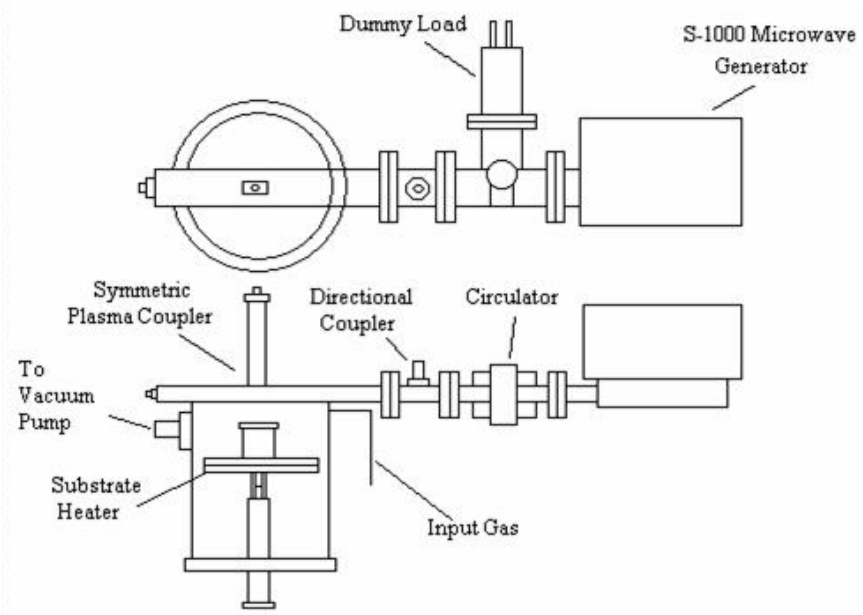

Figure 2.3: Schematic drawing of ASTeX-type microwave plasma enhanced chemical vapor deposition system.

In our lab, two different MPECVD system are dedicated for diamond growth, One is the ASTeX 1000 (shown in Figure 2.4a) and the other is the IPLAS system (shown in

Figure 2.4b) from German. The ASTeX system has a 1KW power supply and has the ability to coat 1 inch area sample while the IPLAS system has a 6 KW power supply and is able to deposit diamond film on 4 in Si wafer.

Figure 2.4: Two MPECVD systems at USF. (a) ASTeX; (b) IPLAS.

2.2 Growth Mechanisms of Microcrystalline Diamond (MCD)

The conventional diamond deposition process utilizes temperature and pressure conditions under which graphite is clearly the stable form of carbon, but kinetic factors allow crystalline diamond to be produced by the typical net reaction of

CH_4 (g) => C (diamond) + 2 H_2. (i)

The reaction mechanism is shown in Figure 2.5.

The chemistry of diamond deposition is complex in comparison to most CVD systems because of the competition for deposition among sp^2 and sp^3 types of carbon, and because of the many chemical reactions that can be involved as a result of the complexity

of organic systems in comparison to the typical inorganic CVD systems. Instead of only one reaction or important precursor species always dominating the deposition, several reactions, whose importance depends on experimental conditions such as temperature, pressure, gas composition, residence time, activation mode, and reactor geometry, happen inside the chamber at the same time (*1*).

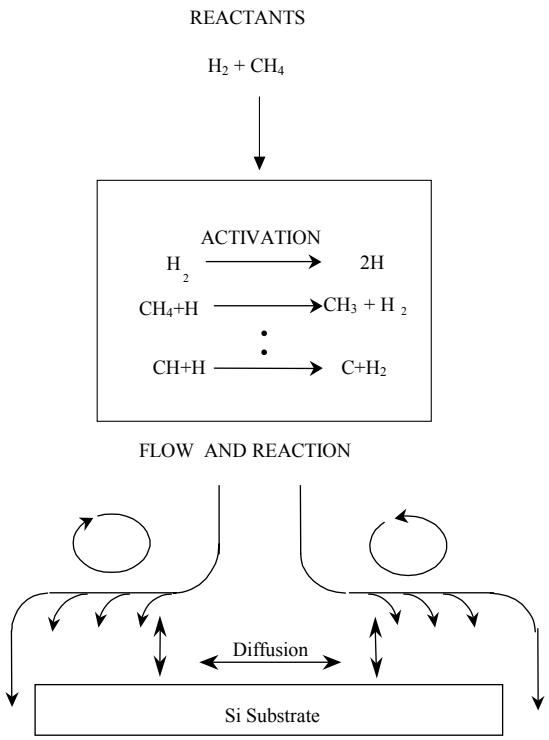

Figure 2.5: Schematic reaction mechanisms of conventional diamond deposition (*1*).

In order to understand diamond growth behaviors, general kinetics have to be considered. Regardless of specific growth mechanisms, there appears to be a growing consensus on two general features of diamond growth reaction kinetics. First, the principal element of diamond growth is the formation of an active site--a surface carbon

sp^3 radical--followed by the addition of a carbonaceous gaseous species to the surface radical formed. Second, the density of carbon surface radicals is determined primarily by the balance between the abstractions of hydrogen from surface C-H bonds by gaseous hydrogen atoms,

$$C_dH + H \Rightarrow C_d\bullet + H_2 \qquad \text{(ii)}$$

and the combination of the carbon surface radicals with free gaseous hydrogen atoms,

$$C_d\bullet + H \Rightarrow C_dH \qquad \text{(iii)}$$

first revealed by Frenklach and Wang (*1*). The notations C_dH and $C_d\bullet$ denote the surface sites of C-H bond and surface radicals, respectively. The reverse of the reaction (ii),

$$C_d\bullet + H_2 \Rightarrow C_dH + H \qquad \text{(iv)}$$

is too slow to compete with the reaction (iii) under typical diamond conditions. The density of the surface radicals is determined by the addition of the growth species to the surface radicals, and by the thermal deposition of the sp^3 diamond surface radicals to sp^2 surface carbons, and vice versa. Typical reaction conditions are: highly diluted gas mixtures of hydrocarbons in hydrogen, substrate temperatures of about 800 to 1000 °C, and a large super-equilibrium of H atoms. With a deficit of hydrogen atoms, the density of active sites is dependent on the concentration of H atoms.

The following are some major observations of conventional diamond growth chemistry:

a) Activation of gas is required for achieving an appreciable diamond growth rate. Activating the gas prior to the deposition increases the diamond growth rate from Å/h to μm/h. In this thesis, microwave is used for gas activation.

b) The carbon-containing precursor is needed in the deposition.

c) Atomic hydrogen has to be present in the gas phase in a super-equilibrium concentration. The activated hydrogen etches sp^2 graphite at a much higher rate than it does on sp^3 diamond.

d) Oxygen added in small amounts to hydrocarbon precursor mixtures enhances the quality of diamond deposits.

e) Graphite and other non-diamond carbons usually are deposited simultaneously with diamond.

f) The deposition parameter such as temperature, pressure, and gas combination are related to the diamond growth rate and quality.

g) A substrate pretreatment of substrate surface with a diamond powder is common to enhance nucleation rates and densities. Electrical biasing of substrates can also influence nucleation rates.

2.3 Growth Mechanisms of Nanocrystalline Diamond (NCD)

With the development of the nanomanufacturing and nanomaterials, the nanotechnology is considered the next generation technique with huge influence on the modern science and technology. For diamond, with the ability to decrease the grain size to nanometer range, the nanocrystalline diamond is considered for a wide variety of structural, biomedical, and microelectronical applications due to its unique electrical, chemical, physical, and mechanical properties. So the fabrication of NCD films by CVD method is of great interest because of its potential experimental and theoretical applications. The drastic changes in mechanical and electrical properties of the phase-pure diamond films, such as going from an insulating to an electrically conducting

material as a result of reductions in crystallite size (the grain boundaries appear to be conducting, and because their numbers dramatically increase with decreasing crystallites size, the entire film becomes electrically conducting and function as an excellent cold cathode (*14*)), are largely due to the fact that the grain boundary carbon is π-bonded. Also, because of the small crystallite size of NCD films, film surface becomes smooth, and they can function extremely well in tribological applications.

In conventional CVD diamond film growth, hydrocarbon-hydrogen gas mixtures consisting typically of 1% CH_4 in 99 % H_2. Atomic hydrogen is generally believed to play a key role in the various diamond CVD process. Just as mentioned in previous section, the atomic hydrogen is generated from the collision process inside the microwave plasma. With a hydrocarbon precursor such as CH_4 that we used in MCD deposition, gas-phase hydrogen abstraction reactions lead to the generation of methyl radical -CH_3 and additional hydrogen abstraction reactions form carbon-carbon bonds resulting in diamond lattice. The methyl radical CH_3 and the acetylene molecule C_2H_2 are the dominant growth species in CH_4/H_2 systems (*15*). However, hydrogen is not totally the only one that can be used to produce diamond. Deposition of carbon films from 5% CH_4, 95% Ar microwave plasma has been shown by several groups of researches to result in graphite or amorphous carbon deposition with only small amounts of diamond inclusions (*16*). The presence of carbon dimer, C_2, in the plasma is believed to be responsible for the formation of graphite or amorphous carbon. Phase-pure diamond films have been grown from C_{60}/Ar microwave plasmas and it was found that the sizes of diamond grains are in nanometer range. The deposition was carried out under the following conditions: total argon pressure of 98 torr, C_{60} partial pressure of 10^{-2} torr, flow rate 100 sccm, and microwave power of

800 W. A new growth mechanism then has been proposed that C_2 dimer is the growth species to form diamond films with nanocrystalline microstructure (*14*).

Carbon dimer is known to be a highly reactive chemical species and it is produced in microwave plasma under highly non-equilibrium conditions. High C_2 concentrations in the plasma, achieved by using C_{60} as the precursor, appear to increase heterogeneous nucleation rates and result in small diamond grain size. Emission spectroscopy study shows that the transition in crystallite size and morphology is correlated with C_2 concentrations in the hydrogen-rich or hydrogen-poor plasmas (*17*). The schematic diagram of growth of the diamond lattice by insertion of C_2 into C-H bands on the (110) surface is shown in Figure 2.6. It can be seen that the insertion of C_2 into C-H bonds on the hydrogenated (110) surface has small activation barriers of less than 5 kcal/mol and is highly exothermic. Subsequent steps involving linkage of C_2 units also have low barriers and lead to growth (*18*). Further, nanocrystalline diamond films have also been grown from CH_4/Ar plasma(*19*). It was also observed that the diamond grain size decreased as more argon was included to replace hydrogen. Further characterization will be discussed in the next part of this chapter. Optical emission studies of the plasma have shown intensive green Swan-band radiation indicating the presence of large number of C_2 dimers in CH_4/Ar plasma (*20*). Interestingly, the C_2 concentration decreases about an order of magnitude upon the addition of 20 % H_2, which is from the reaction of C_2 with H_2 to form hydrogen carbons. Therefore, this reaction will drastically lower the C_2 concentrations in high hydrogen-content plasmas.

The million-fold difference in crystallite size means that secondary nucleation rates associated with growth in hydrogen-poor plasmas are 10^6 times higher than

conventional hydrogen-rich plasmas. The basic idea of the secondary nucleation is that the unattached carbon atom can react with other C_2 molecules from the gas phase to nucleate a new diamond crystallite. Extensive theoretical work has been done over the past years to understand the growth mechanisms from $CH_4/H_2/Ar$ plasma. Sternberg (*20*) *et al*. demonstrated that stable C_2 adsorption configurations which lead to diffusion-assisted chain growth have been found on hydrogen-free (110) surface. Diamond (100) surfaces are the most typical growth surfaces and a density-functional based tight-bonding study has been carried out by on a non-hydrogenated diamond (100)-(2x1) surface by Sternberg (*20*) *et al*. They have simulated diamond growth steps by studying isolated and agglomerated C_2 molecules adsorbed on a reconstructed non-hydrogenated diamond surface. Their calculations suggested that the most stable configuration is a bridge between two adjacent surface dimers along a dimer row, and there are many other configurations with adsorption energies differing by up to 2.7 eV. The (110) face is the fastest growing one in the C_2 regime while (100) faces are slow growing. However, both type of growth and nucleation are possible during diamond growth results in small grain sizes in NCD.

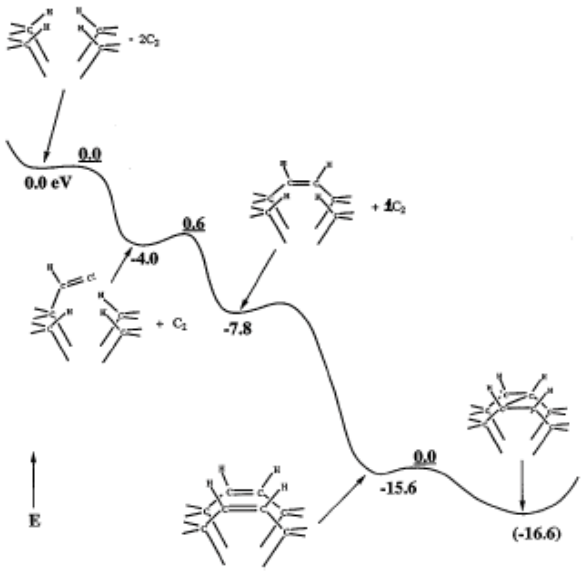

Figure 2.6: Potential energy surface for C_2 addition to diamond (110) surface (barriers are underlined) (*14*).

Overall, diamond could nucleate and grow using carbon dimers as the growth species without the intervention of hydrogen. This new way of diamond synthesis results in very small diamond grains ranging from 5 to 20 nm and very smooth surface. Moreover, the cost of diamond CVD would be dramatically reduced since hydrogen is no longer needed. Diamond obtained from this method contains very high content of sp^3-bonded carbon compared to sp^2-bonded carbon and remains the outstanding properties as of those deposited form hydrogen rich plasma.

2.4 Applications of MCD and NCD Films

2.4.1 Diamond coating for cutting tool applications

The outstanding tribological and mechanical properties make diamond film as a promising coating for cutting tools and inserts. Composites materials and high silicon-content aluminum alloys are extremely abrasive and corrosive which are difficult to be

machined with conventional high speed steel or tungsten carbide cutting tools. Soft and chemically active nonferrous metals have a strong tendency to adhere to the surface of the tool during machining. This increases the friction between the tool and the work piece and results in high specific energy losses during machining. As a result, this leads to high temperatures generated during machining with resulting softening of the work pieces. The standard approach to alleviate these problems is to use material removal fluids during the machining of nonferrous alloys. These tendencies are even more pronounced during dry machining. Under dry machining conditions, soft and chemically active nonferrous alloys strongly adhere to the entire tool surface, forming a strong chemical bond. As a result, in order to machine these kind of materials, efficient and energy saving cutting tools are required to reduce tool's down-time, increase cutting productivity and improve the quality of machined surface.

The most suitable substrate material for producing diamond coated tool is Co-cemented tungsten carbide (WC-Co). Diamond coated WC-Co inserts would result in a cutting tool which is extremely resistant to abrasion while retaining high fracture toughness. Numerous studies have been done over the years to develop diamond coated cutting tools. However, the poor adhesion of CVD diamond is still the main issue preventing useful application of diamond films as wear resistant coatings for carbide tools. Co in the carbides is hostile to diamond adhesion.

R. Haubner (*21*) *et al.* studied diamond deposition on chromium, cobalt and nickel substrates and found that non-diamond carbon layers can be formed with too high a concentration of CH_4. According to phase diagram of the Co-C system, at typical CVD temperatures (700-1000 °C) carbon is soluble in Co up to 0.2-0.3 wt. % C (*22*).

Therefore, the diffusion of C to Co leads to a weak graphite layer between the diamond coating and the substrate. K. Shibuki (*23*) *et al.* deposited diamond coating by hot filament CVD by removing Co from the substrate surface. It was found that the coating layer is mainly composed of diamond with a small amount of non-diamond carbon. F. M. Pan (*24*) *et al.* performed auger studies at the interface between the diamond coating and the WC-Co substrate. A carbon layer, possibly amorphous carbon, with a thickness less than 120 Å was present at the interface. The cobalt in the cemented tungsten carbide may be ascribed to the formation of the interfacial amorphous carbon layer for the hot filament assisted CVD grown diamond film (*25*).

The most widely used method to prevent the Co catalyst effect is to remove the binder phase form the substrate surface with a chemical solution (*26*). The most common etching solutions are aqueous solutions of strong oxyacids or hydrochloric acid. A slightly more complex etching procedure, first introduced by Peters and Cummings (*27*) and whose effectiveness in adhesion enhancing has been widely recognized, makes use of a first treatment with Murakami's reagent ($K_3Fe(CN)_6$: KOH : H_2O = 1 : 1 : 10) and then of etching with Caro's acid (H_2SO_4–H_2O_2 solution). Murakami's reagent attacks WC grains, thus roughening the substrate surface. Caro's acid oxidizes the binder to soluble Co^{2+} compounds, thus reducing the surface Co concentration. However, removal of the binder phase leads to the formation of a brittle, Co-free surface layer of carbide grains which reduce the effectiveness of the cemented carbide tools.

Instead of Co etching, use of interlayer material was shown to be an effective way of improving the adhesion. Many researchers have reported enhanced adhesion properties of diamond coating using various interlayers, ranging from amorphous carbon, to metallic

materials and ceramics. F. Deuerler *et al.* (*28*) sputtered metallic interlayers of different thicknesses and arc-ion plated amorphous carbon films to improve the adhesion of the diamond coating on hard metal cutting tools.

Ti–Si interlayers have been developed by C. R. Lin *et al.* (*29*) to improve film adhesion and inhibit diffusion of Co to the substrate surface on diamond nucleation. Due to the formation of strong TiC and SiC bonding to enhance film adhesion; Si acts as a promoter for diamond nucleation, and the residual stress with application of interlayer is much lower than that interlayer-free. The results also show the existence of an optimum Ti thickness for the best film adhesion.

Multiple interlayer systems composed of Si_3N_4, Si and WC, with Si_3N_4 have been simulated using finite element analysis by J. K. Wright et al. (*30*) to reduce the thermal residual stress for better adhesion. TiC or DLC interlayer using metal plasma immersion ion implantation and deposition has been also used to improve coating's adhesion. M. Nesladek (*31*)et al. investigated the adhesion of diamond coatings on WC-Co by using Rockwell-C indentation. Various surface modifications were studied: Co leaching; replacement of Co by Cu; WC-Co decarburization and deposition of Ti intermediate layer prior to diamond CVD.

Not only microcrystalline, but also nanocrystalline diamond coating has been developed to improve the performance of cemented carbide tools due to its outstanding mechanical properties. Along with great wear resistance, the advantages of NCD coating include high surface hardness, high thermal conductivity, reduced friction, better corrosion protection, low coefficient of friction and improved optical properties. Jian (*32*) *et al.* has developed ultra-fine diamond composite coatings on tungsten carbide. The

mechanical and tribological properties of the films have been studied. Low COF of the film has been measured using pin on disk tests as 0.122, 0.143, 0165 for SiC PRAMC, Cu-1, and Al-0 respectively.

Overall, diamond coating will be an idea candidate for energy-efficient dry machining of nonferrous alloys. Although substrate pretreatment represent a necessary step for depositing adherent diamond films on WC-Co cutting tools and further investigate need to be done to improve the properties of the coating.

2.4.2 Diamond films for MEMS/NEMS applications

Micro/Nano-electro-mechanical systems (MEMS/NEMS) devices are currently fabricated mainly using silicon. Complex shapes and devices, such as gears, pinwheels, micromotors, etc. have been produced using stand lithographic patterning and etching techniques (*33, 34*). However, a major problem with the Si-based MEMS devices is that Si has poor mechanical and tribological properties due to its hydrophilicity, high friction, poor brittle fracture strength and poor wear properties. Rotating devices such as microturbines (*35*) has been fabricated, but are frequently subjected to stiction problems or wear-related failure after a few minute of operation (*34*). Until now, there are no commercially available MEMS devices that involve sliding interfaces. With the rapid development of micro- and nanosystems (MEMS/NEMS) such as optical switches, radio-frequency resonators, pressure sensors, a new type of material with significantly improved mechanical and tribological properties is of great need for MEMS applications involving rolling or sliding contact in harsh and hostile environment.

Diamond is a super hard material with extreme mechanical strength, outstanding thermal stability and conductivity, and chemical inertness. Relevant mechanical properties of Si, SiC and diamond are shown in Table 2.1. Moreover, diamond has much lower COF than Si and SiC. The COF of Si has a relatively high and constant value of ~ 0.6 throughout the temperature ranges; whereas the COF of diamond is exceptionally low ~ 0.05-0.1 at room temperature. The COF of Si is high at room temperature ~0.5, and then drops to a value of ~0.2 as the temperature exceeds 200°C. The COF of diamond drops to 0.01-0.02 was the temperature increase due to the formation of a stable adsorbed oxygen layer on the diamond surface that saturates the diamond dangling bonds and minimizes bonding between contacting diamond surface.

Table 2.1: Selected mechanical properties of Si, SiC, diamond.

Property	Si	SiC	Diamond
Lattice Constant (Å)	5.43	~4.35	3.57
Cohesive Energy (eV)	4.64	6.34	7.36
Young's Modulus (Gpa)	130	450	1200
Shear Modulus (Gpa)	80	149	577
Hardness(kg/mm^2)	1000	3500	10000
Fracture Toughness	1	5.2	5.3
Flexural Strength (Mpa)	127.6	670	2944
Coefficient of friction (COF)	0.6	0.5	0.01-0.02

Numerous NCD based MEMS components and devices have been developed in recent years. There are several ways to fabricate these devices by taking advantage of the extraordinary properties of nanocrystalline diamond. Among them, one of the most apparent ways is to form a conformal NCD coating on existing Si products. Modern Si fabrication technology can produce all kinds of devices in nanometer scale. The basic idea is to form a thin, continuous, and conformal coating with low roughness on the Si component. However, this could not be realized until the recent development of nanocrystalline deposition technique. Conventional diamond CVD deposition results in discontinuous films with large grains and rough surface.

Selective deposition has been used for fabrication of NCD micro-devices, shown in Figure 2.7 (*36*). Nanocrystalline diamond deposition process needs a nucleation layer, usually achieved by mechanical seeding with fine diamond particles or by bias enhanced nucleation. So NCD films could be selectively deposited by selective seeding the substrates. Selective seeding could be achieved by i) remove part of the seeded layer; ii) mask the film during seeding to produce a patterned seeded layer. Note that it is hard to achieve high feature resolution by selective seeding since precise control of seeding is hard to define. Instead, a more advanced method has been developed by lithographic patterning technique. A continuous NCD films were deposited on SiO_2 layer, followed by a sacrifice SiO_2 layer deposited by CVD. Photoresist is deposited onto the top SiO_2 layer and it is patterned by RIE. The NCD film is then etched by oxygen plasma.

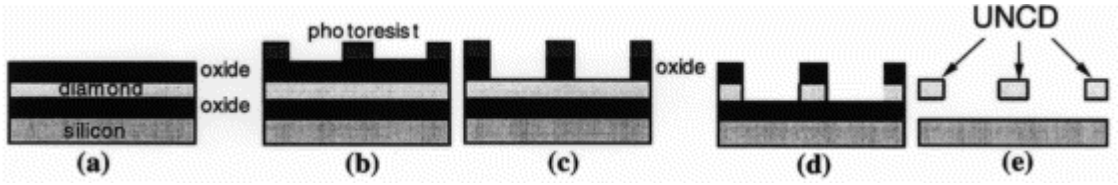

Figure 2.7: Etching scheme for producing a freestanding NCD film (*36*).

Surface acoustic wave (SAW) devices are critical components in wireless communication systems. Diamond exhibits high acoustic phase velocity which makes it an attractive material for high frequency (GHz range) SAW devices. However, high surface roughness and large grain sizes prevent the application of diamond for SAW applications. Time consuming post deposition is required to smooth the MCD surface in order to obtain free standing smooth surface. Moreover, MCD based SAW devices suffer from relatively low performances due to the propagation losses in polycrystalline structures. It is reported that the propagation losses decreases while the diamond grain size diminishes (*37, 38*). Therefore, NCD based SAW devices are expected to have better performance than MCD films. Elmazria (*39*) *el at.* utilized AlN/NCD/Si layered structure to determine the acoustic phase velocity (V) and the electromechanical coupling coefficient (k^2) as a function of NCD thickness. NCD films are grown on (100)-oriented silicon substrate and smooth piezoelectric AlN films with columnar structures and (002) orientations are deposited on top of NCD. Aluminum IDE of 16 and 32 um wavelengths on AlN/NCD/Si is developed by photolithography technique. Devices working at frequency f_0=2.5 GHz can be achieved with the acoustic velocity as high as 9500 m/s and K^2=1.4%. Note that the experimental values and the theoretical values agree very well and the phase velocity strongly increases with the NCD normalized thickness.

The wide band gap, small (or negative) electron affinity, high breakdown voltage, high saturation drift velocity, high carrier mobility, radiation hardness and high thermal conductivity make diamond a promising material for fabrication of high power, high frequency and high temperature solid-state microelectronic devices, sensors/MEMS and vacuum microelectronic devices (*40*). Polycrystalline diamond based RF electronics have been fabricated by various groups. Gerbi (*41*) *et al*. has reported high temperature Schottky diode with thin film diamond. Diamond field effect transistors (FETs) has been investigated by Aleksov (*42*) *et al*. Prins reported the first diamond bipolar junction transistor (BJT) in 1982 on natural, p-type single crystal diamond (*43*). Aleksov (*44*) *et al*. presented the p-n diodes and p^+np BJT structures using nitrogen and boron doping during CVD process. It was thought that only polycrystalline diamond films could be used for RF MEMS devices due to the difficulty of producing large area of NCD films. Surface area is needed for RF structures including active devices, passive components, waveguide circuits and heat dissipation. Until recently, large area deposition of nanocrystalline diamond becomes possible by Ar/CH_4 reactants with microwave chemical vapor deposition technique. Due to the unique properties of nitrogen doped nanocrystalline diamond, a nanocrystalline/dingle crystal diamond heterostructure diode has been fabricated and characterized by K. M. Zimmermann *et al* (*45*). N-type doped NCD films have been deposited on top of a p- active layer (on top of a p+ contact layer) where all the structures are built based on a single crystal diamond substrate. The diode characteristics show rectification and high temperature stability. It is demonstrated that the device has been successfully tested at 1050 °C which represented the highest temperature measurement of any semiconductor up to date. Low forward losses combined

with high breakdown strength have been achieved which is not possible for any other polycrystalline diamond diodes.

Kusterer (*46*) *et al*. demonstrated a Bi-stable micro actuator based on stress engineered nanocrystalline diamond. The NCD film was compressively pre-stressed controlled by different growth conditions. After released from Si substrate, NCD film could buckle into two quasi-stable positions, downwards or upwards. The transition between these two positions could be realized by combining the diamond film with Ni/Cu strips acting as thermal bi-metal elements. Thus, a 10 μm deflection could be achieved with film thickness ~ 2 μm resulting in a 12 V threshold voltage to switch between two stable positions. The first hybrid structure based on NCD as a RF switch was fabricated recently (*46*). NCD actuator is fixed on Al_2O_3 substrate including an interrupted co-planar waveguide. The actuator is fixed in the center of the waveguide, and moves during operation up- and downwards between two stable positions. In down-state position, the micro bridge acts as signal contact connecting the segments of the line. Numerical simulations show the diamond based actuator and base plant can deliver large forces in the range of hundred μN. Therefore, this NCD actuator could also be used for numerous purposes such as micro-squeezer, micro-punch or micro-anvil.

2.4.3 Electrochemistry applications of NCD films

Diamond was first reported for electrochemical applications by Iwaki (*47*) *et al*. Conducting diamond were obtained by ion implantation of natural diamond with argon and zinc. With the development of the CVD technology, CVD diamond electrodes have been widely used in electrochemistry. Pleskov (*48*) and co-workers first extensively

studied the electrochemical properties of diamond electrodes. The diamond electrodes grown by CVD were normally un-doped, but had sufficient conductivity by using specific growth conditions during deposition to introduce defects in diamond films for electrochemical measurements. Moreover, boron doped diamond electrodes have been studied by Swain (*49, 50*) and co-workers. Diamond electrodes exhibit low capacitance and featureless background current which are highly desirable for electro-analytical and sensor applications.

The electrochemical response of diamond electrodes is determined by the nature of the diamond film as well as the surface termination of diamond. The chemical inertness of diamond is remarkable compared to that of other electrode materials. However, the diamond electrodes are not completely electrochemically inert. The electrode surface can change from hydrophobic to hydrophilic and chemically bound oxygen is found on a diamond surface after anodic polarization (*51, 52*). Furthermore, cyclic voltammetry shows that polycrystalline diamond has a redox couple at 1.7 V vs. standard hydrogen electrode (SHE) whereas single crystal diamond doesn't (*53*).

As-deposited diamond electrodes that have been cooled down in a hydrogen-rich environment are terminated with hydrogen. These hydrogen terminated surfaces result in a wide potential range, which is demonstrated in Figure 2.8. Note that various types of electrodes have been evaluated. A wide potential range has been obtained for high quality diamond. Low quality diamond electrodes have a potential window similar to glass carbon and graphite. With this wide 'window', other electrochemical reactions can be observed which makes diamond electrodes attractive for sensor applications (*51*).

Most of the previous electrochemical applications of diamond uses boron doped diamond electrodes. The electrical conductivity induced by boron has been widely studied and its reviews can be found elsewhere (*53*). During deposition diamond changes its nature from a dielectric, then a wide gap semiconductor and finally a quasi-metal when boron is doped to diamond electrodes. Thus, it is possible to tune the electrical properties of diamond by changing the doping concentrations. It has been observed that as the doping levels are increased, the potential window of water stability decreases and the crystalline quality decreases (*54*).

Nitrogen and phosphorus are two deep donors to make the diamond n-type. Recently, sulfur has been reported to five n-type diamond. Eaton (*55*) *et al*. have doped diamond with sulfur and small quantities of boron to produce diamond electrodes with n-type conductivity in the near surface region.

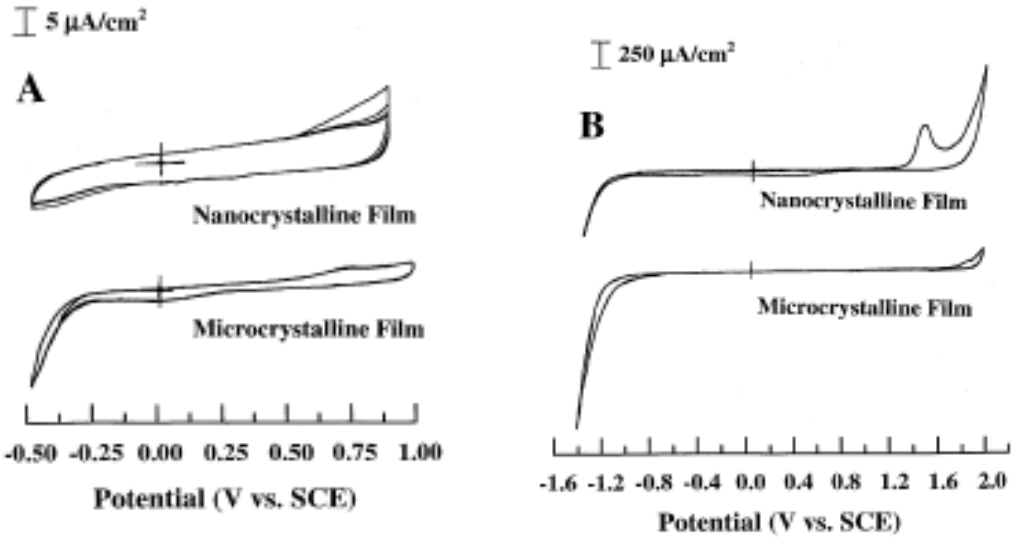

Figure 2.8: Cyclic voltammetric i-E curves of micro and nano diamond films (51).

The electrochemical properties of nanocrystalline diamond were first investigated by Fausett (*56*) *et al*. The electrochemical activity of the NCD electrodes was probed using $Fe(CN)_6^{-3/-4}$, $Ru(NH_3)^{+2/+3}$, methyl viologen and 4-tert-butylcatechol. It was suggested by Fausett that the advantages of using NCD electrodes in electrochemistry compared to microcrystalline diamond included: i) the ability to deposit continuous films at nanometer thicknesses rather than micrometer thicknesses leading to time and cost savings, ii) easier coating of irregular geometry substrates like fibers and high surface area meshes, and iii) the different film morphology and characteristic electronic properties might lead to unique electrochemical behavior (*57*).

2.4.4 Biomedical applications of diamond films

Diamond is known as a biocompatible material which is a good candidate as a biointerface with soft materials for biomedical applications. However, NCD biomedical applications require control of its surface properties such as surface chemistry, wettability, optical properties, etc. the surface modification of synthetic diamond has been investigated by several methods: i) direct chemical functionalization of hydrogen-terminated surface (*58*); ii) application of pretreatment methods that results in the surface hydrophobillic by generation of oxygen-containing surface functionalities (*59*); iii) electrochemical modification of diamond surface by functional groups (*60*). In particular, due to its unique chemical and physical properties, NCD films have been widely investigated as a material for biosensors and biointerface.

The first DNA modification of NCD thin film was reported by Yang (*58*) *et al*. In order to chemically modify clean, H-terminated NCD surfaces grown on silicon

substrates, the H-terminated substrates were photochemically reacted with a long-chain ω unsaturated amine, 10-aminodec-1-ene, that has been protected with the trifluoroacetamide functional group (TFAAD), producing a homogeneous layer of amine groups for DNA attachment.. The protected amine was then deprotected, leaving behind a primary amine. The primary amine was reacted with a heterobifunctional crosslinker sulphosuccinimidyl-4- (N-maleimidomethyl) cyclohexane-1-carboxylate (SSMCC) and finally reacted with thiol-modified DNA to produce the DNA-modified diamond surface.

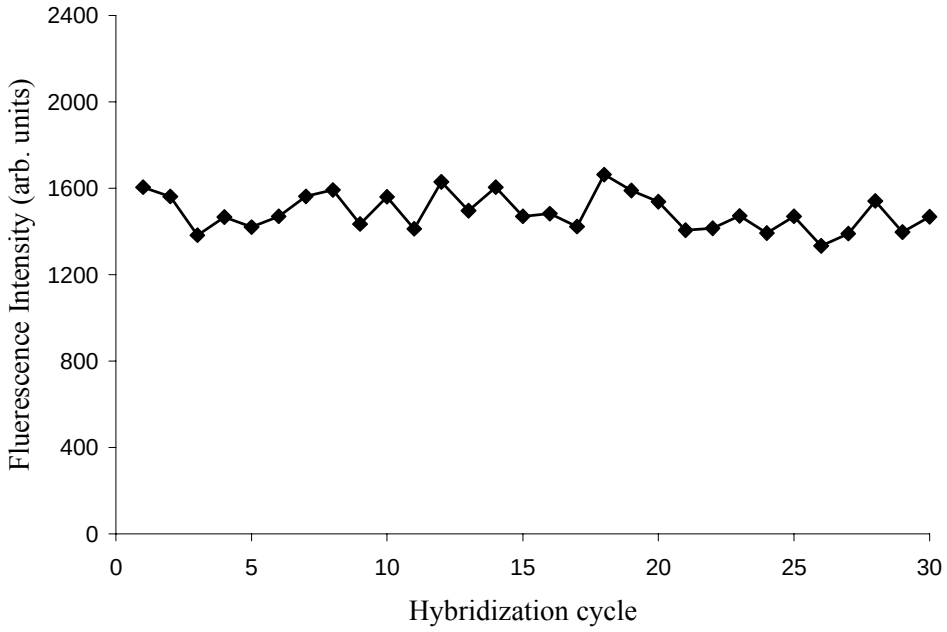

Figure 2.9: Stability of DNA-modified NCD and other materials during 30 successive cycles of hybridization and denaturation (*58*).

Hybridization reactions with fluorescently tagged complementary and non-complementary oligonucleotides showed good selectivity of NDA modified NCD films with matched and mismatched sequences. Comparison of NCD with other substrates including gold, silicon, glass, and glassy carbon showed that diamond surfaces exhibited

extremely good stability, and without loss of selectivity (in Figure 2.9). No decrease in intensity from a complementary sequence, and no increased background after exposure to a non-complementary sequence has been found by the end of 30-cycle stability test (*58*).

Not only DNA but other proteins have been covalently attached to NCD films by chemical functionalization (*60*). H-terminated NCD films were modified by using a photochemical process and green fluorescent protein was covalently attached. A direct electron transfer between enzyme's redox centre and the diamond electrode was detected. An enzyme-based amperometric biosensor was fabricated by functionalizing the surface of a NCD film with the enzyme catalase (from bovine liver). The device was fabricated on top of the hydrogenated NCD film. Two small Ti/Au coated contacts were oxidized on top of the diamond surface. The contacts and the hydrogenated area in between were isolated from the rest of the sample surface by second oxidation step. Then another layer of gold was evaporated to establish good electrical contact between the hydrogenated area and the contacts. The sample was then functionalized by a serious biofunctionalization process. Detailed functionalization step could be found from the paper published by Hartl (*60*) *et al*. They have demonstrated that biomolecules can be covalently immobilized on NCD surfaces and these immobilized biomolecules retained their functionality. The strong C-C covalent bond at the diamond/biolayer interface provides an important advantage over normally used metal electrodes such as gold.

Yang (*61*) *et al.* have reported the fabrication and characterization of a biologically sensitive field-effect transistor (Bio-FET) using a NCD thin film. Biomolecular recognition capability was provided by linking human immunoglobulin G (IgG) to the diamond surface. The biomolecular recognition and specificity characteristics

were tested using two different antibodies anti IgM and anti IgG. The results showed that the bio-FET device responded only to the anti-IgG antibody. The diamond surfaces were first terminated with hydrogen in a radio frequency plasma system. An organic protection monolayer film was covalently linked (step 1) to the surface via photoexcitation at 254 nm. De-protection in 0.36 M HCl/methanol (step 2) flowed by reaction with 3% solution of glutaraldehyde in a sodium cyanoborohydride coupling buffer for 2 h (step 3) then produced a diamond surface with some exposed aldehyde groups. Gold was then sputtered on the diamond surfaces to form ohmic source and drain contacts. The metal channel was coved with epoxy to insulate them from the solution. The modified diamond surfaces were immersed in human immunoglobulin G (IgG) solution for 8 h (step 4) which binds the IgG to the surface. The top electrodes were finally deposited by sputtering a thin Pt layer. The results show that the modification of diamond surface with IgG yields the ability to selectively recognize and detect the corresponding anti IgG. The sensitivity of the sensor is estimated to be ~7 μg/ml of anti IgG (*61*).

Lu (*62*) *et al*. reported a newly developed DNA-modified diamond surface showed excellent chemical stability compared with modified gold and silicon surfaces using similar chemical attachment under high temperature (60°C). Detection sensitivity was improved by a factor of ~ 100 by replacing the DNA-modified gold surface with a more stable DNA-modified diamond surface. Experiments by Remes (*63*) *et al*. demonstrated the amino-functionalization of NCD diamond surface in RF plasma of vaporized silane coupling agent N-(6-aminohexyl) aminopropyl trimethoxysilane. NCD films were grown on low alkaline glass substrates at lower temperature below 700°C. The surface functionalization was performed for time ranging from 3 to 180 min in two RF

reactors with standard excitation frequency of 13.56 MHz. It was found that low temperature and low RF plasma power were two key factors to successfully functionalize the NCD film. Uniform coverage with a high density of the primary amines has been achieved. Adsorption and immobilization of cytochrome C on nanodiamonds has been achieved by Huang (*64*) *et al*. The immobilization started with carboxylation/oxidization of diamonds with strong acids, followed by coating the surfaces with poly-L-lysine (PL) for covalent attachment of proteins using heterobifunctional cross-linkers. The functionalization was proved with fluorescent labeling of the PL-coated diamonds by Alexa Fluor 488 and subsequent detection of the emission using a confocal fluorescence microscope.

2.4.5 Field emission devices

Metal field emission diode and triode are the first developed field emission devices (*65-67*). However, these field emission devices have limited applications because of their high work functions and high turn-on electrics. Furthermore, the impurity adsorption on metal surfaces lead to instable current and high turn on voltage. Several approaches have been proposed such as Si and W emitters although no significant improvement has been achieved (*68-70*). With the discovery of the diamond negative electron affinity (NEA) surfaces, diamond and related materials have attracted extensive investigation of their electron field emission properties (*71*). NEA means that electrons can exit from conduction band edge into vacuum without further energy barrier. A NEA occurs when the vacuum level lies below the conduction band minimum at the semiconductor/vacuum interface. The presence of a NEA for a semiconductor allows

electrons in the conduction band to be freely emitted into vacuum without a barrier. Experiment results show that electron field emission from diamond or diamond coated surface yield large currents at low electric fields. The chemical inertness of diamond allows diamond based field emitters to work in relatively low vacuum compared to other materials. In addition, strong crystal structure ensures the devices to be operated with long life. Furthermore, due to it high electrical breakdown field and high thermal conductivity, diamond can operate at high temperature or at high power. Thus, diamond emitters possess promising performance for potential application such as flat panel displays or other field emission devices.

Wang (*72*) *et al*. was the first to report field emission from diamond surfaces. Zhu (*73*) *et al*. demonstrated a correlation between the defect density present in un-doped and p-type doped diamond films and the require field for emission. It was proposed that defects in the film created sub-bands just below the conduction band and facilitated the promotion of electrons to the conduction band for subsequent emission. Although diamond has negative electron affinity surface, it plays minor role in enhancing the field emission in previous mentioned models for un-doped or p-type doped polycrystalline diamond films. All the electron emissions do not involve the conduction band for these films(*73*). However, n-type doping could solve this problem. The electrons could be supplied to the diamond conduction band via a low resistance ohmic contact and they will be emitted at the NEA surfaces. From previous discussions, we have known that n-type doping could be incorporated into nanocrystalline diamond films and make them n-type, which results in a large number of researches on NCD based field devices.

Nitrogen has a high solubility in diamond and is found in both natural and synthetic diamonds. Geis (*74*) *et al*. reported enhanced field emission properties of nitrogen-doped single crystal doped diamond. Okano (*75*) *et al*. have reported threshold fields less than 1 V/μm for nitrogen doped diamond films. Zhou (*76*) *et al*. studied the field emission properties of nanocrystalline diamond prepared from C_{60} precursors. Their results showed that the field emission characteristics strongly depended on film's microstructure that can be controlled by growth conditions.

Krauss (*77*) *et al*. have investigated the field emission properties of UNCD films coated Si tips. The NCD were grown by CH_4-Ar plasma on sharp single Si microtip emitters. Field emission results show that CND coated tips exhibit high emission current (60 -100 μm/tip). The emission turn-on voltage for diamond coated tips decreased dramatically compared to uncoated Si tips. For uncoated Si tips, the threshold voltage was proportional to the tip radius. For NCD coated tips, the threshold voltage becomes nearly independent of the diamond coating thickness, the tip radius and the surface topography. A model which field emission occurs at the grain boundaries of NCD has been proposed.

Subramanian (*78*) *et al*. have reported enhanced electron field emission properties of NCD tip array prepared from $CH_4/H_2/N_2$ gas mixtures. NCD films grown by this protocol had grain size as small as ~5nm. The improved field emission behavior was attributed to their better geometrical shapes, increased sp^2 bonded carbon content and high electrical conductivity by incorporation of nitrogen impurity in the diamond. The NCD field emission cathode array was fabricated by FIB nano-mold transfer technique (*79*). N-type silicon was nano-molded by high precision milling using a focused ion beam, where a focused beam of gallium ions is used to form arrays of high-respect ratio

conical cavities of controlled diameter and depth. The mold could also be created by anisotropic etching of Si with KOH solution although the aspect ration of this method is relatively low. NCD films were then deposited with $CH_4/H_2/N_2$ plasma on top of the mold followed by thick MCD layer (~30μm) growth with conventional CH_4/H_2 plasma. A metal layer such as Ti/Ni (1 μm) was deposited on diamond film followed by silicon etching using KOH solution to yield diamond nano-tips with high aspect ratio. The radius of curvature of the diamond nano-tips is about 25 nm and the aspect ratio of the nano-tips is found to be as high as ~120.

The effect of gases on the field emission properties of NCD films has been studied by Hajra (*80*) *at el.* A significant reduction of turn-on voltage and an increase in the emission current has been observed with the exposure of hydrogen. Tips exposed to Ar and N_2 showed less emission current at pressure ~10^{-5} Torr while the current reached its original value after the chamber was pumped down to $8x10^{-10}$ Torr.

CHAPTER 3:

SYNTHESIS AND CHARACTERIZATION

3.1 Experiments to Synthesize Diamond Films from Micro to Nano

From previous section, we have discussed that the microstructure of diamond films changes dramatically with the continued addition of Ar to reacting gas mixtures during CVD process. The transition from micro- to nanocrystallinity by systematically adding argon to hydrogen-rich plasma will be characterized by SEM micrographs as a function of argon content in the following section. Different combinations of gas mixtures have been listed in Table 3.1. (100) silicon samples (1 inch by 1 inch) were used as the substrates. Surface pretreatment was employed before the deposition to enhance the nucleation density of diamond. 4 to 8 nm diamond powders were used to polish the sample surface by hand scratching and the substrates were ultrasonically cleaned in ethanol for 2 min. The diamond films were deposited in a 1 KW 2.45-GHz ASTeX system. A mixture gas of Argon, hydrogen and methane was used as source gas. The first set of samples was deposited using different $Ar/H_2/CH_4$ gas combination. Detailed growth conditions are shown in Table 3.1. Growth length is around 3 hours. Then based on the results, several sets of samples were grown with different growth parameters. High percentage of methane (up to 5 %) and different pressure was select to investigate the parameter effect on the NCD growth to optimize the system. Note that when adding Ar gas, the CH_4 was kept at 1% all the time and the volume percentages of H_2 were changed.

Table 3.1: Summary of reactant gases used for diamond deposition.

Sample No.	Ar (vol %)	H_2 (vol %)	CH_4 (vol %)
1	0	99	1
2	50	49	1
3	75	24	1
4	95	4	1
5	98	1	1

The most apparent difference in the films grown by hydrogen-poor plasmas compared with conventional hydrogen-rich plasmas is the smaller diamond grain sizes in nanometer range. The nanocrystallinity of the films grown by CH_4/Ar plasma has been extensively characterized by various techniques. The surface morphologies have been studied by scanning electron microscopy (SEM), transmission electron microscopy (TEM), and atomic force microscopy (AFM). Raman spectroscopy and near edge x-ray absorption fine structure (NEXAFS) have been used to characterize film's bonding structures. Nanoindentation has been employed to measure the mechanical and tribological properties. Results of characterization studies on the nanocrystalline diamond films are discussed below.

3.2 Characterization Results

3.2.1 Scanning electron microscopy

Scanning electron microscopy has been a very useful technique in the characterization of diamond thin films. Conventional light microscopes use a series of glass lenses to bend light waves and create a magnified image. The SEM creates the

magnified images by using electrons instead of light waves. In a SEM system, an electron gun emits a beam of high energy electrons, and this beam travels downward through a series of magnetic lenses designed to focus the electrons to a very fine spot. As the electron beam hits each spot on the sample, secondary electrons are knocked loose from its surface and a detector counts these electrons and sends the signals to an amplifier. The final image is built up from the number of electrons emitted from each spot on the sample. The SEM could show very detailed 3-dimensional images at much higher magnifications than is possible with a light microscope.

Plan view SEM micrographs are shown in Figure 3.1. It can be seen that the surface morphology of diamond films changes dramatically with the continued addition of Ar. Figure 3.1a shows the surface morphology of a diamond film grown with 0 % Ar. Well faceted microcrystalline diamond grains with grain sizes ranging from 0.5 to 2.0 μm have been deposited. (111) and (110) planes could be found and the surface is very rough. The plan-view SEM micrograph of a film grown with 50 % Ar, 49 % H_2, and 1 % CH_4 mixture shows that small diamond particles start to form during the deposition process, shown in Figure 3.1b. For films grown with 75 % Ar, shown in Figure 3.1c, the number density of the small crystals increases significantly and most of these small crystals nucleate and grow between boundaries of large diamond crystals. Large diamond crystals begin to disappear and well faceted microcrystalline diamond grains no longer exit. Diamond crystals change from microcrystalline to nanocrystalline when 95 % Ar is added to the Ar/ H_2/CH_4 plasma, shown in Figure 3.1d. Faceted microcrystalline diamond crystals have disappeared and diamond crystals at nanometer scale have been formed.

For films deposited with 98% Ar, the crystals are further reduced to less than 20 nm, shown in Figure 3.1e.

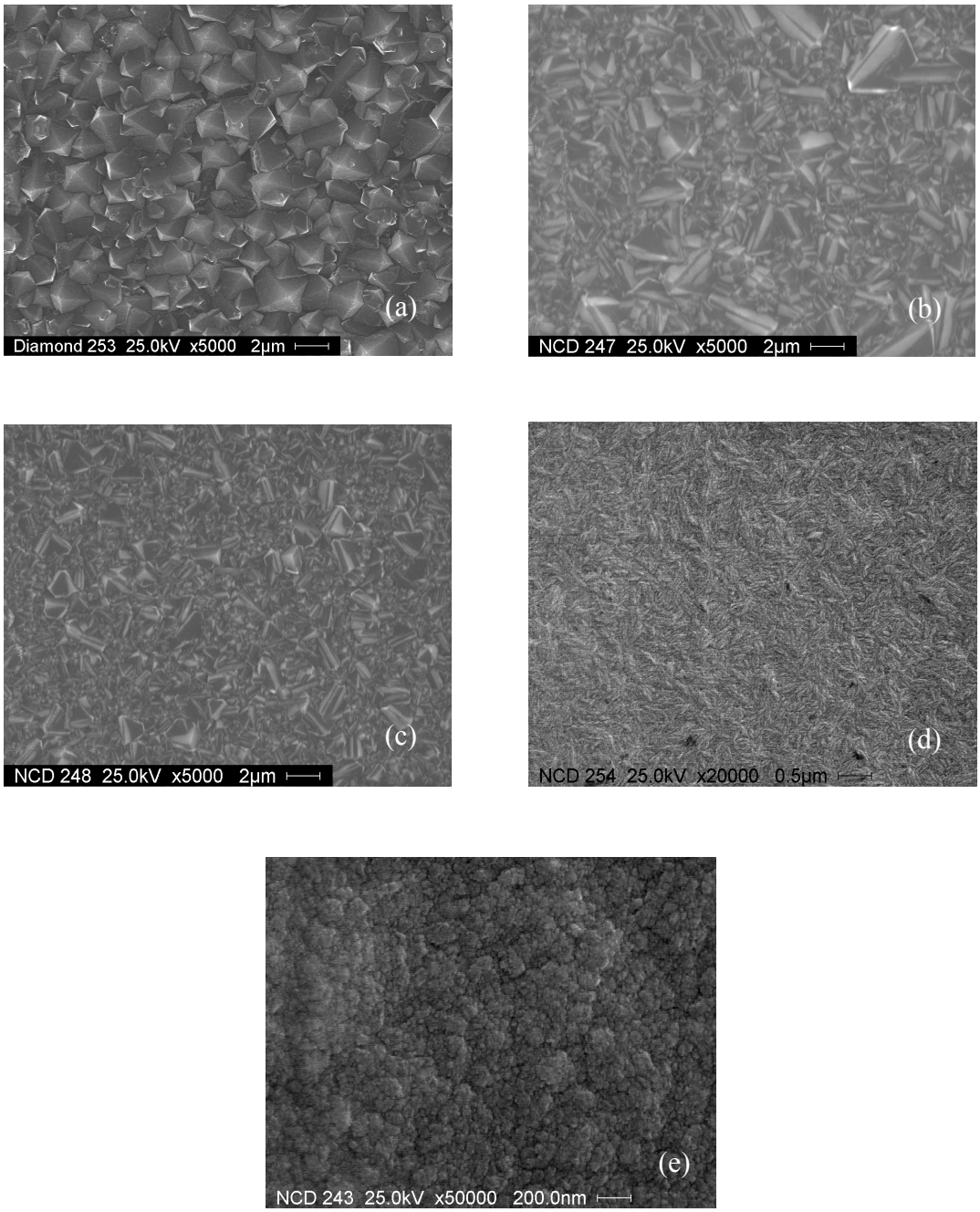

Figure 3.1: SEM images of diamond films grown with different Ar: (a) 0%, (b) 50%, (c) 75%, (d) 95%, and (e) 98%.

Therefore, it is demonstrated that the microstructure of the diamond film could be controlled by varying the gas mixtures. The more the content of Ar in the reactant gases, the smaller the diamond grain sizes and the smoother the surfaces are.

In order to obtain information on the development of the growth morphology, the cross-section SEM micrographs of diamond films with different Ar volume percentages are shown in Figure 3.2. Columnar growth structures can be observed in film grown without Ar, shown in Figure 3.2a. This type of surface morphology could be explained by van der Drift growth mechanism (*81*). During conventional diamond growth, hydrogen prevents diamond crystals from secondary nucleation by regasfying small or nondiamond phase. Therefore, after a period of time, only large diamond crystals can survive to form columnar crystallites, which are so called the "evolutionary selection of crystallites". For films deposited with more than 98% Ar, the columnar structure totally disappears, shown in Figure 3.2b. Very fine and smooth surfaces are observed from the SEM micrographs, suggesting that the nanocrystalline diamond does not grow from the initial nuclei at the substrates during nucleation but from the second nucleation with C_2 as the nucleation species.

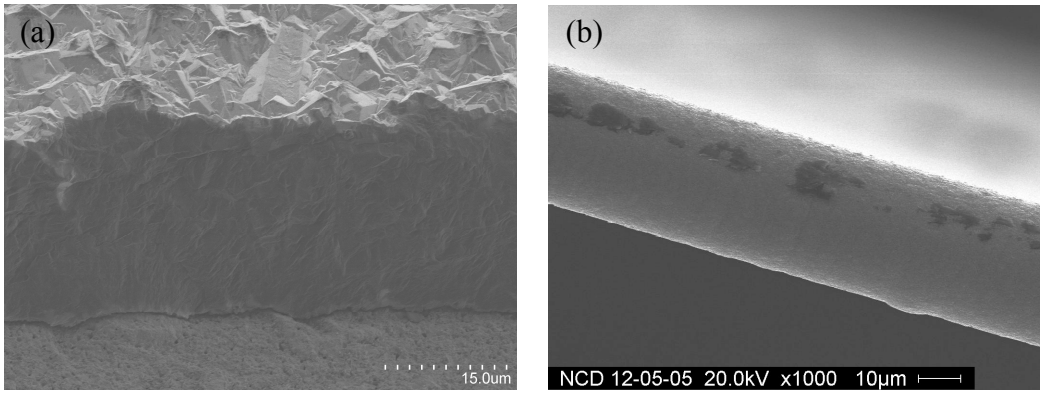

Figure 3.2: SEM cross section images of diamond films grown (a) with or (b) without Ar.

So far it is demonstrated the changes of diamond microstructure are the reflections of the changes in the plasma chemistry. During NCD growth, the C_2 dimmer and atomic hydrogen concentrations in the microwave discharges were monitored. Increasing the Ar content in the reactant gas mixtures significantly promotes the concentration of C_2 dimer, which is the nucleation species for NCD growth. Besides the growth mechanism, surface morphology and microstructure, the growth rate of diamond film has also been found to depend on the ration of Ar to H_2 in the plasma.

3.2.2 Transmission electron microscopy

TEM is a powerful technique due to its high spatial resolution (~0.2nm) in imaging. A TEM works much like a slide projector. A projector shines a beam of light through (transmits) the slide, as the light passes through it is affected by the structures and objects on the slide. This transmitted beam is then projected onto the viewing screen, forming an enlarged image of the slide. TEM works the same way except that it shines a beam of electrons (like the light) through the specimen (like the slide). Whatever part is transmitted is projected onto a phosphorous screen for the user to see. Materials for TEM must be specially prepared to thicknesses which allow electrons to transmit through the sample. Because the wavelength of electrons is much smaller than that of light, the optimal resolution of TEM images is many orders of magnitude better than that from a light microscope. Thus, TEM can reveal the finest details of internal structure as small as individual atoms.

Since MCD has grain size as large as several microns, SEM micrograph can successfully shows the structure of the film. However, NCD has very small crystals

compared to MCD and it is necessary to use TEM to analyze these nano sized crystals. Figure 3.3 shows a bright-field TEM image revealing the plan-view morphology of the NCD thin film. The grain boundary width estimated from the TEM micrograph is 0.2 to 0.5 nm. The insert image shows a selected area (over 10 μm in diameter) electron diffraction pattern. Sharp Bragg reflections are located in concentric circles, indicating the random orientation of nanocrystalline diamond grains. Due to the limitation of the small objective aperture, results obtained by tradition TEM might be incorrect as grain size decreases to the nanometer scale diamond grains will overlap on each other (*82*). Therefore, high resolution electron microscopy (HREM) offers a high resolution and more reliable results. Figure 3.4 shows a HREM image of an Ar/1%H_2/1% CH_4 NCD film, it is estimated that the grain size of diamond crystals is around 10 to 15 nm and the grain boundary thickness ranges from 0.2 to 0.4 nm. The inset image shows a sharp ring pattern of the selected area electron diffraction (SAED), indicating that the diamond grains have a random orientation. Diamond crystallization of (111), (220), and (311) can be observed from this image. No graphite or amorphous carbon reflections can be observed from indicating the film is phase pure diamond. We can measure the lattice distance of NCD grains from this HREM image. The lattice of the (111) diamond is around 0.205 nm. Different pressure and different methane concentration of diamond films have been also synthesized and the detail characterization has been reported in my Master thesis.

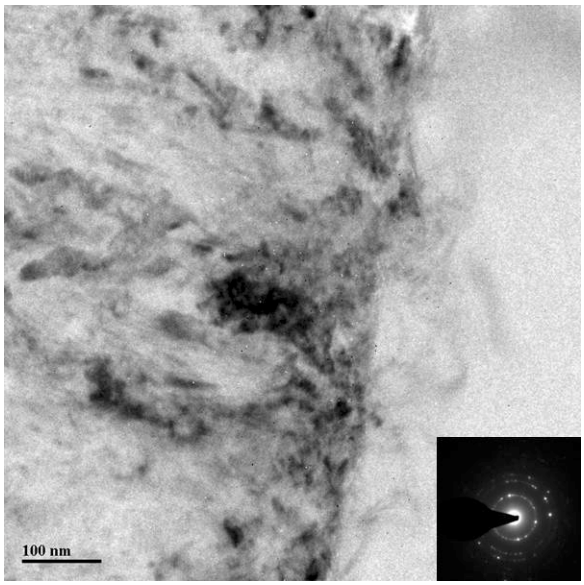

Figure 3.3: A plan view TEM image of the diamond film. Film was prepared from an Ar/CH_4 plasma at 100 Torr. It shows that the diamond film consists of nanocrystalline grains ranging from 3 to 20 nm. The inset image shows a SAED pattern image.

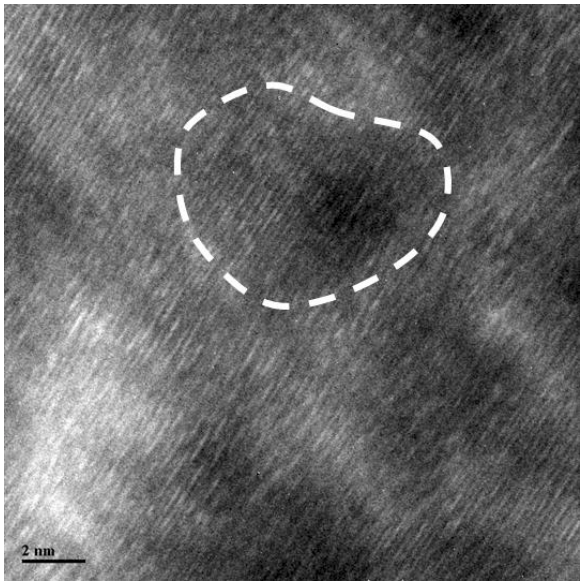

Figure 3.4: HREM image of an $Ar/1\%H_2/1\%$ CH_4 NCD film. Typical grain size is around 5-15 nm.

3.2.3 Raman spectroscopy

Raman spectroscopy is a method of chemical analysis that enables real-time reaction monitoring and characterization of compounds in a non-contact manner. The

sample is illuminated with a laser and the scattered light is collected. The wavelengths and intensities of the scattered light can be used to identify functional groups in a molecule. It has found wide application in the chemical, polymer, semiconductor, and pharmaceutical industries because of its high information content and ability to avoid sample contamination.

When light is scattered from a molecule most photons are elastically scattered. The scattered photons have the same energy (frequency) and, therefore, wavelength, as the incident photons. However, a small fraction of light (approximately 1 in 107 photons) is scattered at optical frequencies different from, and usually lower than, the frequency of the incident photons. The process leading to this inelastic scatter is then termed the Raman Effect. Raman scattering can occur with a change in vibrational, rotational or electronic energy of a molecule.

Especially, Raman scattering is about 50 times more sensitive to π-bonded amorphous carbon and graphite than to the phonon band of diamond. Hence, Raman spectroscopy could be used to establish the crystalline quality of diamond thin films by estimating the amount of sp^2 bonded carbon in the films. Figure 3.5 shows the plots of micro Raman spectra obtained of diamond films grown with H_2/CH_4 and with $Ar/H_2/CH_4$ plasma. For film grown without Ar, a sharp diamond characteristic peak is observed at 1332 cm^{-1}. No Raman scattering can be found in the range from 1400 to 1600 cm^{-1} suggesting that the diamond film contains very little sp^2 bonded carbon. With addition of argon the sharp diamond peak at 1332 cm^{-1} no longer exits, and it is significantly broadened as a result of decreasing the grain size to the nanometer scale.

A broad peak in the 1400-1600 cm^{-1} is observed due to the presence of sp^2 bonded carbon at the grain boundaries in the nanocrystalline diamond films.

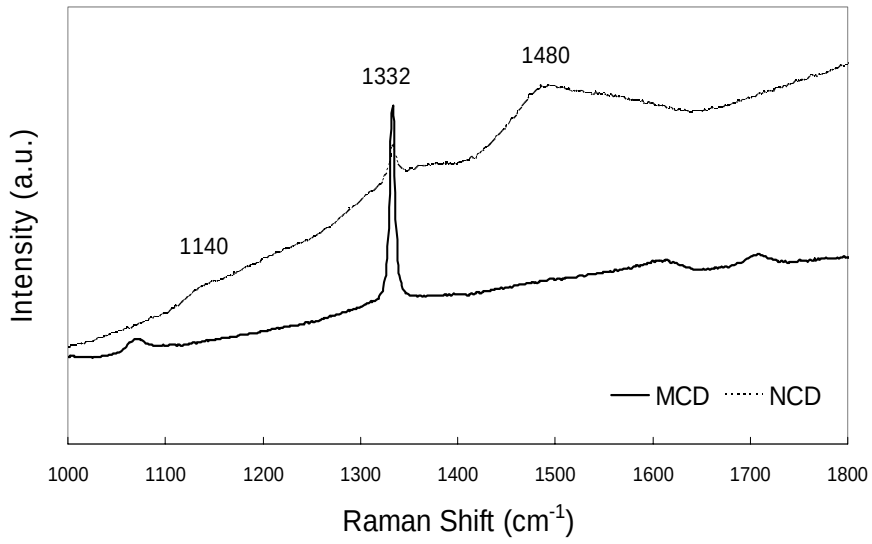

Figure 3.5: Raman spectra of micro- and nanocrystalline diamond films.

3.2.4 Near edge x-ray absorption fine structure (NEXAFS)

A technique that can distinguish between sp^2-bonded carbon (graphite) and sp^3-bonded carbon (diamond) would be very useful for characterizing the nanocrystalline diamond films. X-ray core level reflectance and absorption spectra is site and symmetry selective and the magnitudes and energy positions of spectral features contain bonding information of the films. Particularly, the near edge region of the core-level photoabsorption has been used to relative quantity of sp^2 or sp^3 bonding in BN powders and thin films (*83*). Its sensitivity to the local bond order in a material arises from the dipole-like electronic transitions from core states, which have well-defined orbital angular momenta, into empty electronic (e.g., antibonding) states. Therefore, the symmetry of the final state can be determined and the difference between sp^2 and sp^3 can be distinguished.

Besides, NEXAFS with a photon beam of the size of millimeter has the ability to investigate the film over a large area.

NEXAFS measurements has been carried out on MCD and NCD films as well as a reference samples, highly oriented pyrolytic graphite (HOPG) that is 100% sp^2 bonded. The spectrum of single crystal diamond that is 100% sp^3 bonded is also shown in (*84*).

Figure 3.6 and Figure 3.7 shows the total electron yield (TEY) C (1s) photoabsorption data from four different samples, natural diamond, graphite, microcrystalline diamond deposited with H_2/CH_4 and nanocrystalline diamond deposited with Ar/CH_4. From previous studies, we have found that amorphous carbon shows the characteristic transition to sp^2 bonded π^* orbitals at ~285 eV and bulk diamond shows a sharp peak at ~290 eV due to the bulk C-1s core exciton and characteristic transitions to sp^3 bonded σ^*orbitals (*85*). These two features are directly related to the bonding structures of diamond and graphite and could be used to determine the sp^2 to sp^3 ratio in a film. A second band gap at 302.5 eV is also a characteristic peak of diamond, which can not be observed from graphite. The graphite absorption spectrum is distinct from single crystal diamond, and shows a prominent feature at 285 eV corresponding to the π^* antibonding state. The graphite spectrum also shows a σ^* peak at 291 eV and does not show the second band gap feature at 302.5 eV.

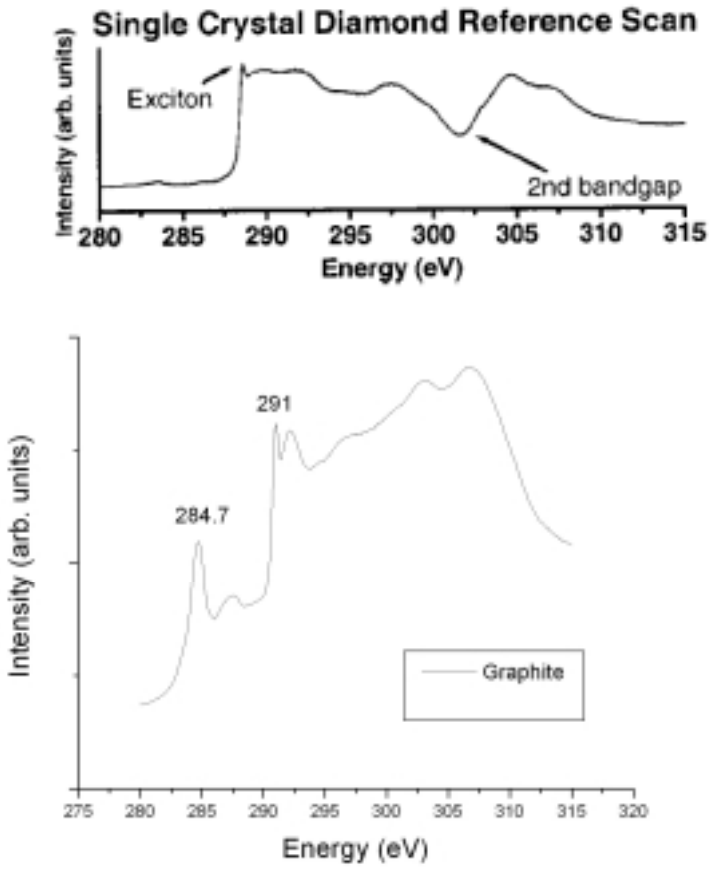

Figure 3.6: TEY analysis by NEXAFS. (a) Single crystal diamond reference scan (*84*); (b) graphite reference scan.

From Figure 3.7 we can clearly see that all of the qualitative features of sp^3 bonding are presented in NCD film. Quantification of the amount of sp^2-bonded carbon is given by the following equation:

$$f_{sp^2} = \frac{I_{sam}^{\pi^*}}{I_{ref}^{\pi^*}} \cdot \frac{I_{ref}(\Delta E)}{I_{sam}(\Delta E)} \qquad \text{(v)}$$

Where $I_{sam}^{\pi^*}$ and $I_{ref}^{\pi^*}$ are the areas of the π* peak of the diamond sample and the graphite reference sample, respectively; and the $I_{ref}(\Delta E)$ and $I_{sam}(\Delta E)$ are the areas evaluated over the remainder of the graph. Note that the reference graphite consists of

100% sp^2-bonded carbon. Based on the qualitative line shape of the spectra, it is estimated that around 8 % of sp^2 bonded carbon exists in the NCD film while the MCD film contains around 4.9 % of sp^2 bonded carbon.

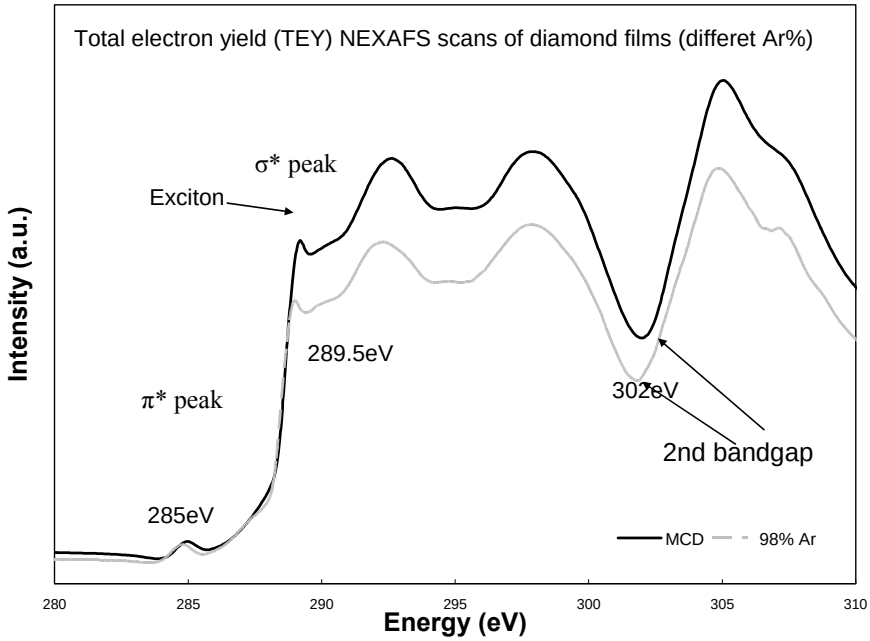

Figure 3.7: TEY NEXAFS spectra of diamond films deposited with and without Ar.

3.2.5 Atomic force microscopy

Microcrystalline diamond films have relatively high surface roughness that precludes the immediate application of diamond films in machining and tool wear applications. High surface roughness results in high friction and severe wear losses on mating surfaces. Polish of these MCD are often applied to smooth the film surface although it is costly and impractical in some circumstances such as complex geometries. However, with the development of growing smooth NCD films, low COF ~0.05-0.1 and fine finish of the sample surface (20-40 nm, rms) have been achieved. We have studied the surface roughness of both MCD and NCD films by AFM. Higher surface roughness

(100-300 nm) was obtained for film seeded by mechanically polish and deposited in Hydrogen rich plasma, while as lower surface roughness (20 nm) for film seeded ultrasonically with fine diamond powders and deposited under Ar rich plasma, as shown in Figure 3.8. Clearly, NCD film has much better surface smoothness with no obvious porosity.

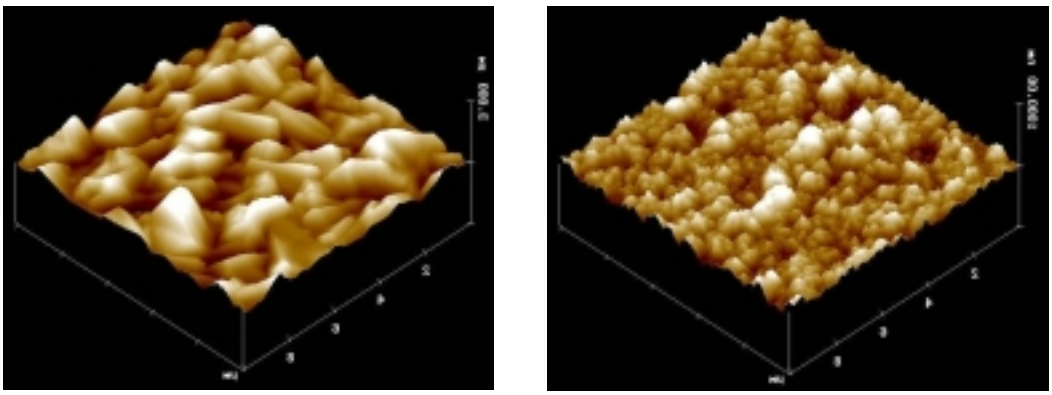

(a) MCD (1% CH_4 in H_2) (b) NCD (1% CH_4, 1% H_2, 98% Ar)

Figure 3.8: Roughness analysis of MCD and NCD films by AFM. (a) MCD has a root mean square root (rms) roughness of 107 nm and a distance from peak to valley of 250–300 nm. (b) NCD has an rms of 20 nm with a distance from peak to valley of ~70 nm.

3.2.6 Mechanical properties

The mechanical properties of NCD film has been evaluated by nanoindentation system (Nano XP). . Indentation tests are perhaps the most commonly applied means of testing the mechanical properties of materials. In such a test, a hard tip, typically a diamond is pressed into the sample with a known load. After some time, the load is removed. The area of residual indentation in the sample is measured and the hardness, H, could be calculated from the maximum load, P, divided by the residual indentation area, A. Figure 3.9 shows the nanoindentation test results of NCD films. The average hardness of the NCD film is ~ 75±3.8 GPA and the average modulus of the film is ~ 908±86 GPA.

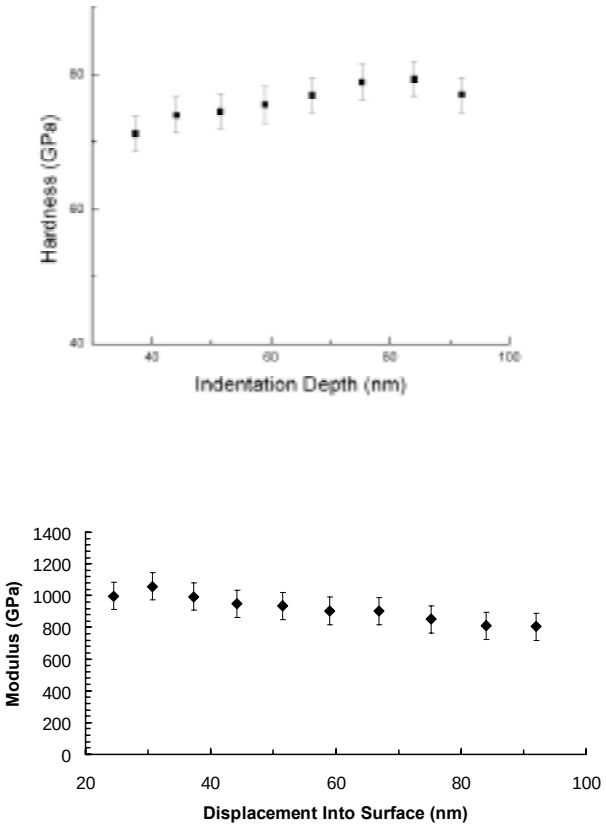

Figure 3.9: Nanoindentation of NCD films. (a) Hardness and (b) Young's Modulus of NCD film. The average hardness is about 75±3.8 GPa and the modulus is about 908±86 GPa.

CHAPTER 4:

DIAMOND COATING ON WC-Co SUBSTRATE

4.1 Introduction

The cemented tungsten carbide cutting tools are used widely in the machining, mining and stone cutting industry. However, these tools are found to wear rapidly when machining some particular materials such as green ceramics, abrasive composites or high silicon-filled aluminum. Especially, in today's automotive industry, lightweight materials such as aluminum and magnesium alloys, high-strength steels, and composites are developed to reduce vehicle weight and improve vehicle's strength in the same time. As a result, in order to machine these materials, efficient and energy saving cutting tools are required to reduce tool's down-time, increase cutting productivity and improve the quality of the machined surface. In our study, diamond coating has been proposed to improve the performance of cemented carbide tools due to its outstanding mechanical properties. Along with great wear resistance, the advantages of the diamond coating include high surface hardness, high thermal conductivity, reduced friction, better corrosion protection and improved optical properties.

Poor adhesion of diamond coating is the main technical barrier for commercialization of diamond-coated tools (*86-89*). During the high temperature diamond deposition process, the presence of cobalt in cemented carbide suppresses diamond growth. Co leaching from the WC-Co substrate catalyzes the formation of non-

diamond carbon (sp^2 bonded), instead of sp3 bonded diamond. The weak graphite layer at the interface results in poor adhesion between the diamond coating and the substrate (*90*). Various approaches have been reported to avoid or reduce the catalytic effect of cobalt on the growth of diamond films. Removing the Co binder from the substrate using Murakami reagent and acid etching is usually conducted to grow adhered diamond coatings (*87, 91-94*). However, substrate's mechanical properties and toughness are significantly reduced after etching. In addition, a large amount of residual stress will be produced due to mismatch of the coefficient of thermal expansion (CTE). The film could easily delaminate from the substrate right after deposition. Diffusion barriers such as Cu (*95*), Cr (*96*), Ti-based layer (*97*) and CrN (*98*) have been developed to prevent the Co catalyst effect but the adhesion of the diamond coating still needs to be improved.

In our study, a new method consisting of two step substrate surface pretreatments has been developed to improve the adhesion strength. Prior to the diamond deposition, a thin Cr/CrN/Cr multi-interlayer system has been pre-deposited to work as a diffusion barrier between the substrate and the diamond coating. The buffer layer coated substrate was shortly peened by friable diamond powders afterwards. Short peening roughened the substrate and possibly imbedded the particles of the diamond powder into it, providing the anchors for the deposited coating. Note that the top Cr layer was used as a soft protective layer for CrN during short peening. Moreover, the interlayer not only works as a diffusion barrier but also reacts with carbon containing gaseous species to produce an additional compound layer for bonding with the diamond film.

4.2 Experimental

Commercial cemented tungsten carbide gears and rectangle bars were selected for this investigation. The first set of experiments was conducted to establish the effect of acid etching on the adhesion on cemented carbide substrates. The substrates were ultrasonically cleaned in acetone for 15–20 min to remove any chemical residue prior to conducting the experiments. Samples were etched by hydrochloride acid for 15 and 60 min, respectively before being scratched with diamond powder for nucleation. Diamond films were deposited afterwards.

The second set of samples was deposited with interlayers to improve the adhesion. Cemented carbide coupon samples (WC-6%Co) were first cleaned by acetone and methanol in an ultrasonic bath for 10 min. A very thin Cr layer (~100 Å) was deposited on the substrate. A 2.5 μm thick layer of CrN was then deposited followed by a 2.5 μm thick Cr surface film. The interlayer depositions were done by a K.J. Lesker CMS-18 sputtering system at room temperature with Ar pressure around 10 mTorr. 150 W DC and RF power were used for Cr and CrN deposition respectively. The growth rate of the interlayer deposition is around 1 μm/h. This Cr/CrN/Cr multi-interlayer system acted as a diffusion barrier, preventing C/Co inter-diffusion during CVD process. In order to improve diamond nucleation and adhesion, short peening of the buffer layer coated substrate by friable diamond powders was carried out by a Raytech RB-6BC sandblasting machine at a pressure ~ 2000 Torr for 30 sec. Friable diamond powders with an average grain size about 150 μm were selected for peening to achieve a proper surface roughness for higher nucleation and better adhesion.

Diamond films were synthesized by an ASTeX Microwave Plasma Enhanced Chemical Vapor Deposition (MPECVD) system. Hydrogen and methane were used under the following conditions: microwave power, 800 W; substrate temperature, 700 °C; pressure, 80 Torr; gas composition, H2:CH4 (mass flow rate: 500/5 sccm); deposition time, 6 h. The process conditions utilized here ensure the formation of a continuous diamond film on the substrate with union film thickness of approximately 9 μm.

The substrate surface roughness before and after short peening was measured by atomic force microscopy (AFM) using a Digital Instruments Dimension 3000 system. The surface morphology of the deposited diamond films was investigated by a Hitachi s-800 scanning electron microscopy (SEM). Energy dispersive spectroscopy (EDS), attached with the SEM, was used to study the film composition along the cross section of the diamond coated sample. X-Ray diffraction (XRD) patterns have been recorded before and after the diamond deposition by a Philips Xpert diffractometer equipped with a copper x-ray tube operated at 45 kV and 40 mA. Data were collected at 30-100° 2θ using an integrating time of 4 s per step and a step size of 0.01 ° 2θ. Rockwell indentation tests were conducted by a Wilson/Rockwell Hardness Tester (Series 500) to evaluate the coating adhesion with a load of 1470 N. Film compositions in the indentation zone were determined by electron probe microanalysis (EPMA) with a Camera Instruments model SX100 electron probe. Electron beam conditions were typically 15 kV and 40 nA during the analysis.

4.3 Results of Surface Pretreatment

4.3.1 Acid etching

Figure 4.1shows SEM micrographs of WC–Co etched with hydrochloric acid for 0, 15, and 60 min. Figure 4.1a shows the SEM image of the bare WC-Co sample. Figure 4.1b shows that the binder phase is selectively removed exposing the WC grains only in some regions while at other regions they are still covered with cobalt. Figure 4.1c is a SEM micrograph of the same substrate after prolonged etching 1 h showing that the cobalt binder phase is etched completely leaving an isotropic rough surface. Compare these two pictures, we found that a long time etching could result in removing more cobalt in the substrate surface and the polycrystalline WC particles were exposed.

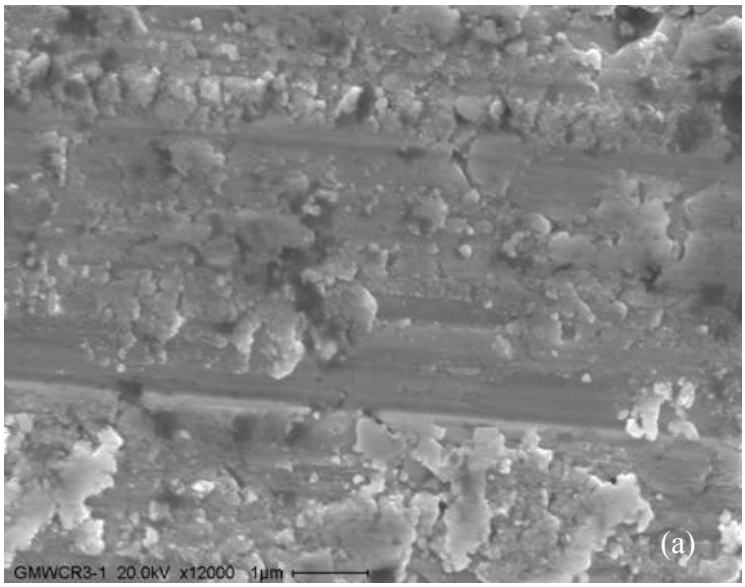

Figure 4.1: SEM micrographs of WC-Co substrates etched with hydrochloride acid for (a) 0 min (b) 15 min (c) 1 hour.

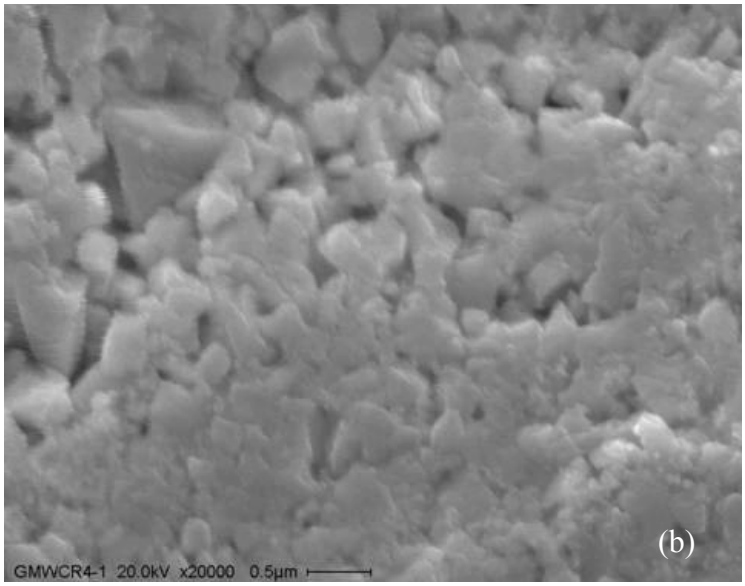

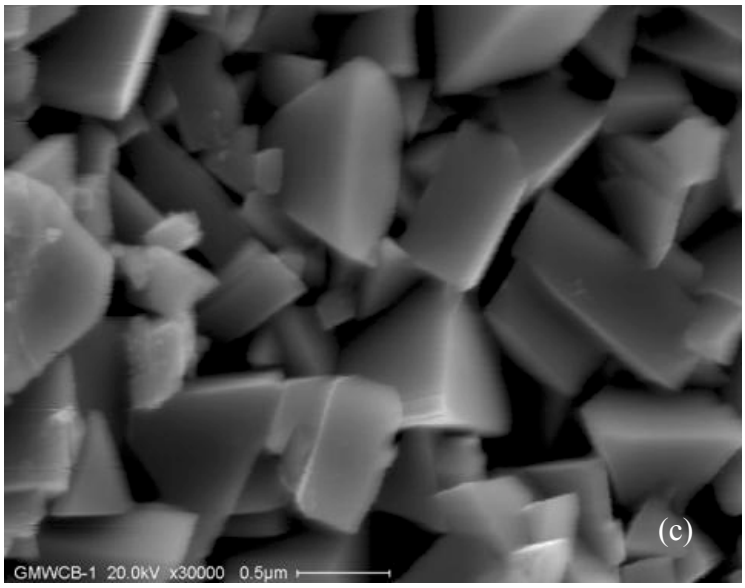

Figure 4.1: (Continued).

Diamond deposition was conducted on these samples after acid etching. Although uniform coating has been deposited all over the substrate surface as well as the side wall, all three samples showed some film delamination right after the deposition, shown in Figure 4.2. The poor adhesion problem was mainly due to the weak graphite interlayer

and the different thermal coefficient of the diamond film and the tungsten carbide substrate. Moreover, as mentioned before, the acid etching leads to a very brittle WC-Co substrate. So the conclusion is that only using the acid pretreatment is not enough to deposit adherent diamond film on the WC-Co substrate.

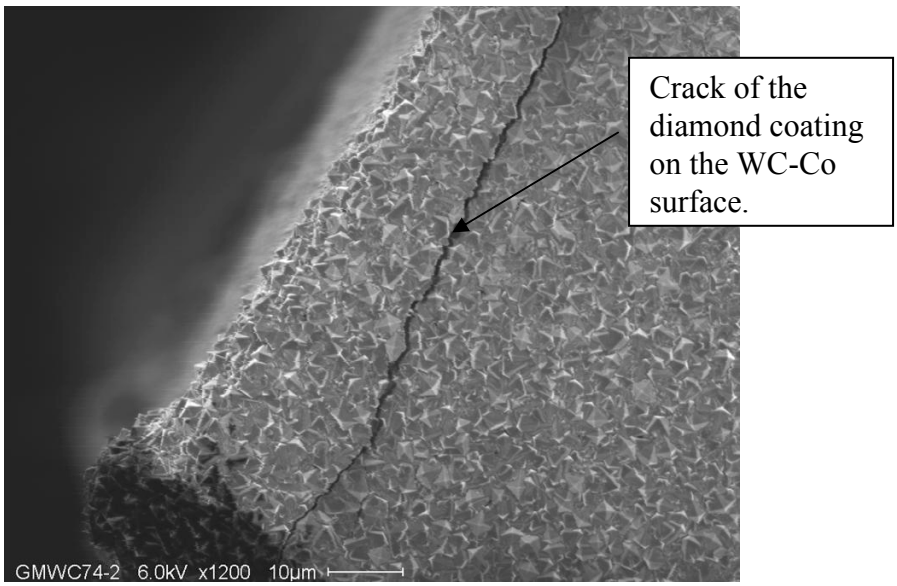

Figure 4.2: SEM micrograph shows the crack of diamond coating.

4.3.2 Substrate roughening

Figure 4.3a and Figure 4.3b show the surface view AFM images of a Cr/CrN/Cr coated substrate before and after surface roughening. Surface roughness (Rms) of the interlayer coated sample is 42 nm while that of the blasted sample increased to 274 nm. Figure 4.3c shows the AFM section analysis on the blasted sample. It can be observed that short peening significantly roughened the sample surface, leaving craters as deep as 832 nm. Since the top Cr layer is about 2.5 μm thick, it will be thick enough to protect the CrN layer during sandblasting. Short peening also broke the diamond powders and hence

possibly imbedded small diamond particles or seeds into the substrates, shown in Figure 4.3d, resulting in a strong mechanical interlocking between the film and the substrate.

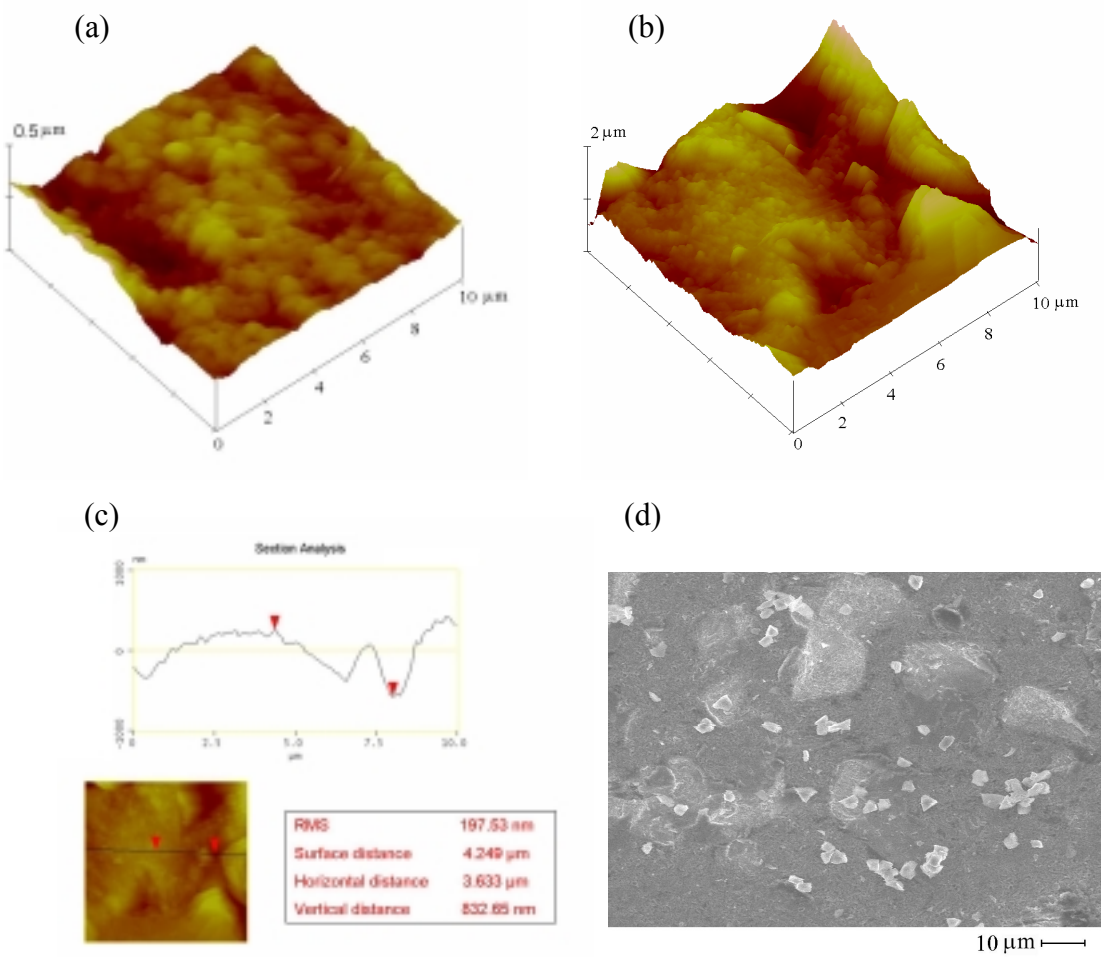

Figure 4.3: Comparison of substrate before and after surface treatment. (a) AFM surface view of a Cr/CrN/Cr coated WC-Co substrate. (b) AFM surface view of the substrate after short peening with diamond powder. (c) Cross section analysis of the peened surface. Craters as deep as 830 nm have been obtained. (d) SEM micrograph of the peened substrate.

4.3.3 Diamond deposition

Diamond depositions have been done on a bare WC-Co substrate and substrates with different surface treatments. Four different kinds of samples, bare WC-Co, shortly peened WC-Co, WC-Co coated with Cr/CrN/Cr interlayer, and WC-Co with interlayer

and peening were prepared for diamond deposition. It was observed that diamond films grown on first two samples delaminated from the substrates right after the deposition. On the other hand, no delamination could be observed for last two samples. Therefore, the Cr/CrN/Cr interlayer successfully prevented the Co catalyst effect and diamond films grown on samples with interlayer had much better adhesion properties. Growth has been conducted for different time to investigate the nucleation and growth of depositing diamond film on WC-Co substrate.

For all substrates, the growth of diamond from the vapor phase begins with nucleation. In order for nucleation to proceed, an incipient nucleus must form and be stable long enough for lattice growth to occur. Diamond nucleation during CVD occurs as a result of some combination of suppression of graphite nucleus formation, stabilization of diamond nuclei and surfaces and preferential etching of sp^2 carbon. In order to obtain these conditions, most current diamond CVD growth methods use large amounts of atomic hydrogen that inhibits graphite nucleation and selectively etches graphite nuclei.

After some growth, the entire substrate surface is covered with crystals and a polycrystalline diamond film will form. Such film often contains small, uniform diamond crystals suggesting that nucleation occurs during the early stage of growth. Figure 4.4 shows the SEM image of the film grown after 1 h. Continuous film with very small crystals has been formed. The average grain size is around 0.5 μm and the growth is quite regular while <111> crystals could be observed all over the surface.

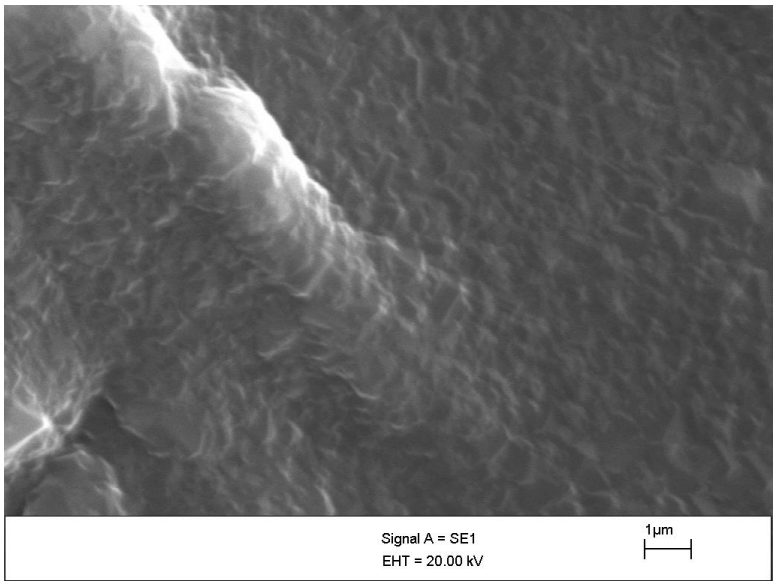

Figure 4.4: SEM micrograph of diamond coating deposited on WC-Co substrate with Cr/CrN/Cr interlayer for 1h.

Nucleation then ceased, whereas diamond crystals continue to grow by carbon diffusion on the substrate or crystal surface. The crystal size is usually inversely related to the nucleation density. Crystals are isolated and tend to be larger with low nucleation density. The growth is limited by the maximum carbon diffusion distance on the substrate. The nature and timing of nucleation depends on the substrate and its pretreatment prior to growth. For our cutting tool applications, WC-Co substrate is selected for diamond deposition due to its good mechanical properties and low thermal expansion coefficient.

Figure 4.5 shows the diamond film deposited 3 h. The surface shows quite similar features compared to the previous one. Homogeneous diamond crystals covered all the substrate. The grain size of most crystals is around 1 µm.

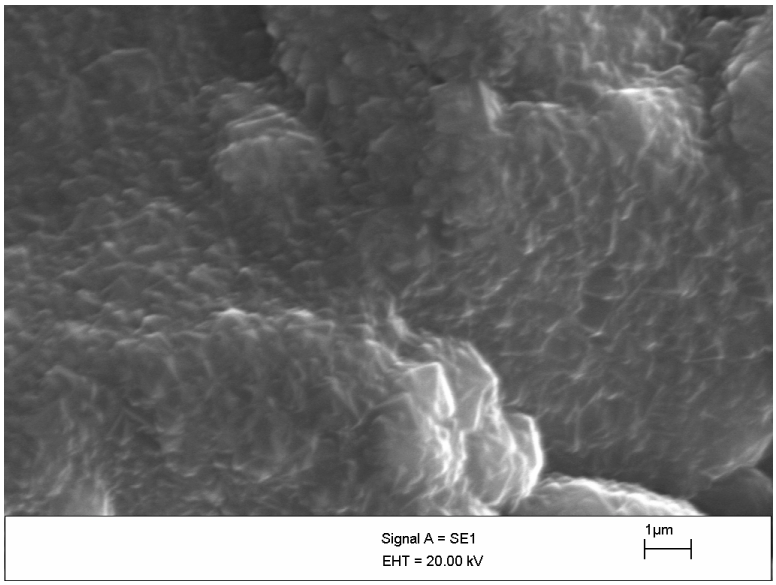

Figure 4.5: SEM micrograph of diamond coating deposited on WC-Co substrate with Cr/CrN/Cr interlayer for 3h.

Figure 4.6 shows the SEM image of film grown for 6 h. Large diamond crystals with grain size around a few microns can be observed. In what Van Der Drift called 'evolutionary selection', grains in a polycrystalline film with the highest vertical growth velocity with respect to the substrate surface will have the highest probability of survival. As growth continues these grains will dominate and ultimately determine the texture of the film. So as a result this grain growth competition not only dictates the film's internal fiber structure, but its final surface morphology as well.

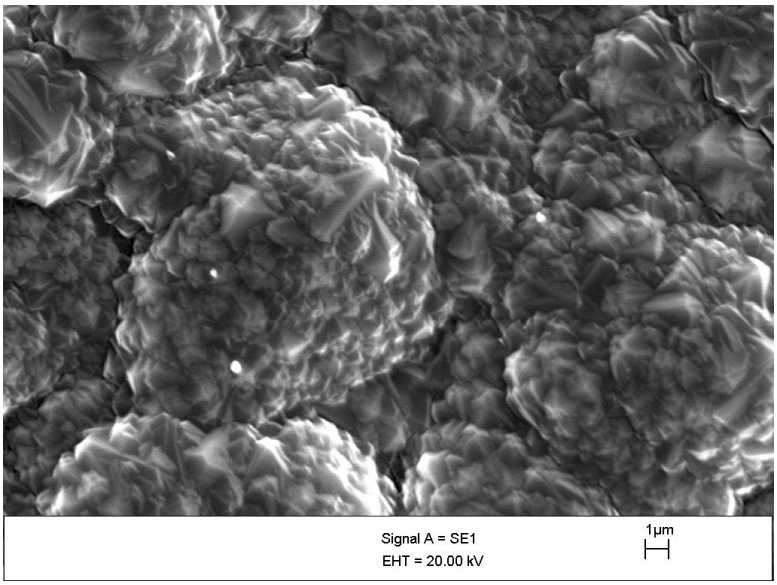

Figure 4.6: SEM micrograph of diamond coating deposited on WC-Co substrate with Cr/CrN/Cr interlayer for 6h.

Diamond films grown for 9 h and 12 h are shown in Figure 4.7a and Figure 4.7b, respectively. From Figure 4.4 to Figure 4.7 we have observed that with the increase of deposition time some diamond grains become larger and larger while the others remain the original size and stop growing. The apparent different grain size increasing with film thickness is a result of 'evolutionary selection' between grains. Grains that grew most normal to the silicon substrate propagated and survived while grains that grew in off-normal directions were overgrown, buried and their growth terminated.

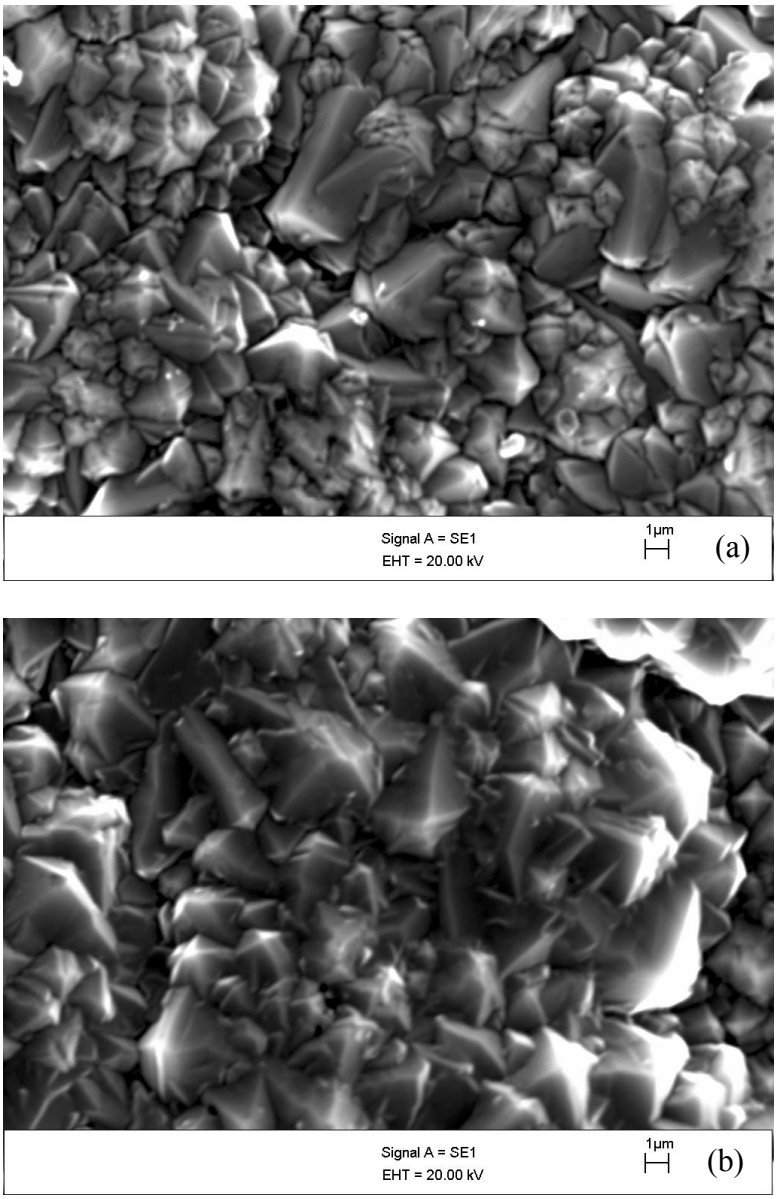

Figure 4.7: SEM micrograph of diamond coating deposited on WC-Co substrate with Cr/CrN/Cr interlayer for (a) 9h; (b) 12h.

A Cr/CrN/Cr coated WC-Co sample was partially peened and a 9 µm thick diamond film was deposited afterwards. SEM micrograph of the film is shown in Figure 4.8a. Relatively smooth diamond coating has been grown on the untreated surface (top part) while the surface roughness of the coating is found much higher in the roughened area (bottom part), shown in Figure 4.8b. Sharp diamond crystals with an average grain

size of 2 to 3 μm can be observed. It is well known that nucleation density plays an important role on the adhesive properties of thin film coating. Therefore, small diamond particles left on the substrate during surface roughening could possibly increase the nucleation rate in the early stage of deposition. Moreover, surface roughening can increase the interfacial area between the film and the substrate, resulting in stronger mechanical interlocking between the coating and the substrate, and leading to effective adhesion of diamond films.

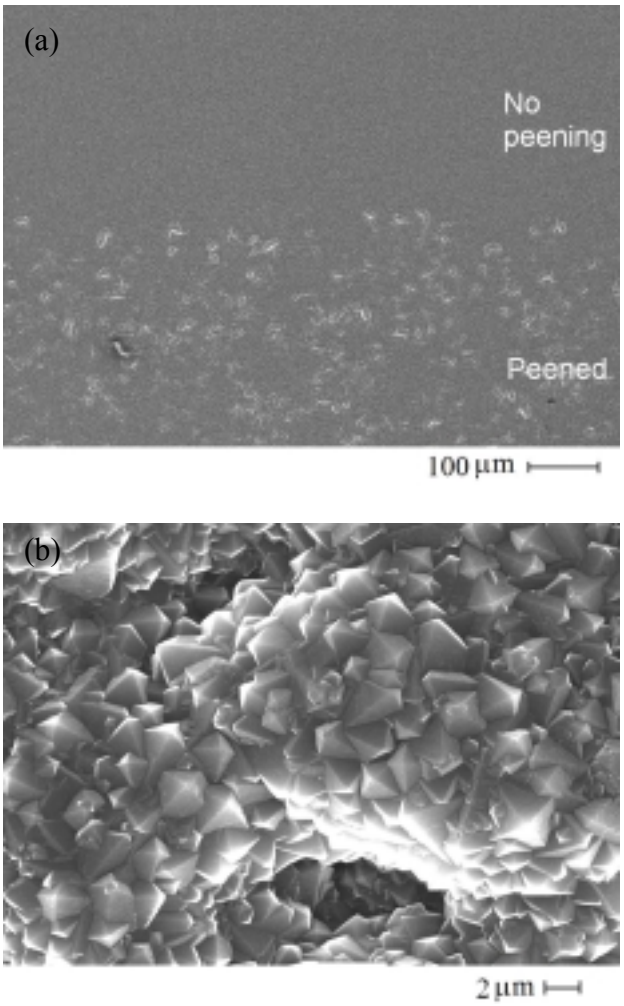

Figure 4.8: SEM micrographs of diamond coating. (a) SEM micrograph of a diamond coating deposited on a partially blasted WC-Co substrate coated with Cr/CrN/Cr. (b) High magnification SEM micrograph of diamond crystals grown on the short peened substrate side.

Figure 4.9 shows the XRD patterns of a roughened and interlayer coated WC-Co sample before and after diamond deposition. Before the deposition, a Cr peak and two small CrN humps along with several WC peaks are presented in the XRD pattern. After the deposition, two diamond peaks, corresponding to <111> and <311> crystallization, are presented at 44.0° and 91.7° respectively. A possible diamond <220> peak might overlap with a WC peak at 75.6°. Note that two additional peaks representing Cr_3C_2 and one peak representing Cr_7C_3 have been observed in the spectrum, suggesting a chromium carbide intermediate layer was formed during diamond deposition process.

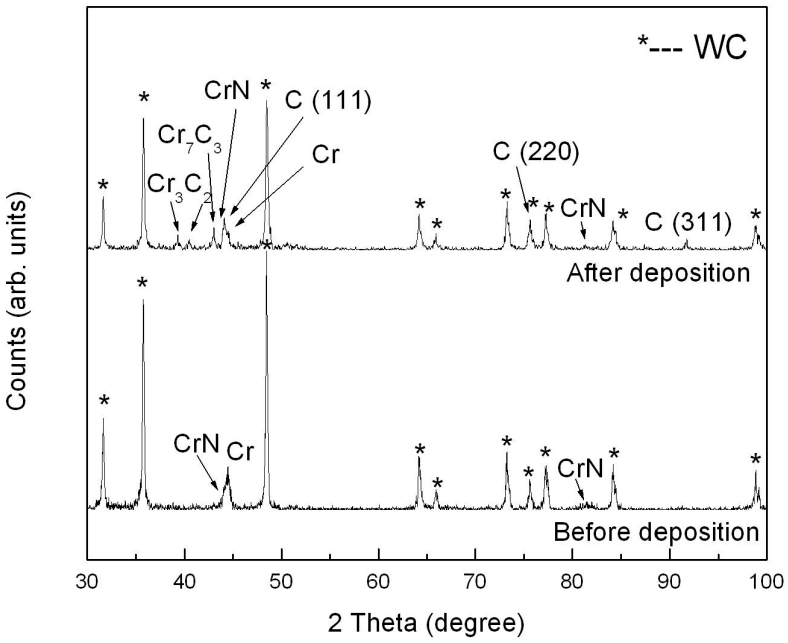

Figure 4.9: XRD patterns of an interlayer coated and short peened WC-Co substrate before and after diamond deposition.

Cross section analysis of the diamond coating on a blasted and interlayer coated WC-Co substrate was performed by EDS. Figure 4.10a shows the EDS analysis at the bottom of the interlayer where a small amount of Co was detected. However, at the top of

the interlayer, shown in Figure 4.10b, nearly no Co could be detected from the EDS spectrum, indicating the Cr/CrN/Cr interlayer successfully prevented Co/C inter-diffusion during diamond deposition. Note that the peak at 1.5 kV in Figure 4.10b origins from the Al sample holder.

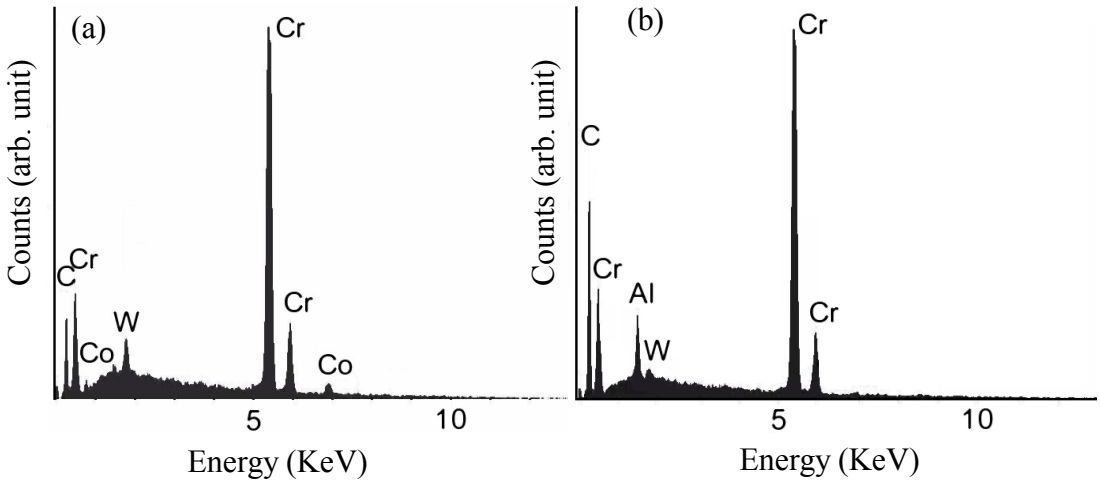

Figure 4.10: EDS cross section analysis of the diamond coating deposited on a WC-Co substrate with Cr/CrN/Cr interlayer. (a) Co peaks are presented at the bottom part of the interlayer; (b) Nearly no Co pattern is observed at the top part of the interlayer.

4.3.4 Rockwell indentation tests

In order to investigate the coating failure mechanism and films' adhesion strength, diamond coated samples were indented by a Rockwell C indenter with a load of 1470 N. Indentation tests have been performed on two samples. Both samples were coated with buffer layers, one being shortly peened while the other one was not peened at all. For the film deposited on the substrate without surface peening, a large area of the diamond film got peeled off, as shown in Figure 4.11a. No remnants of the coating are observed on the failure surface, suggesting that the delamination took place entirely along the interface between the diamond coating and the interlayer, as shown in Figure 4.11b.

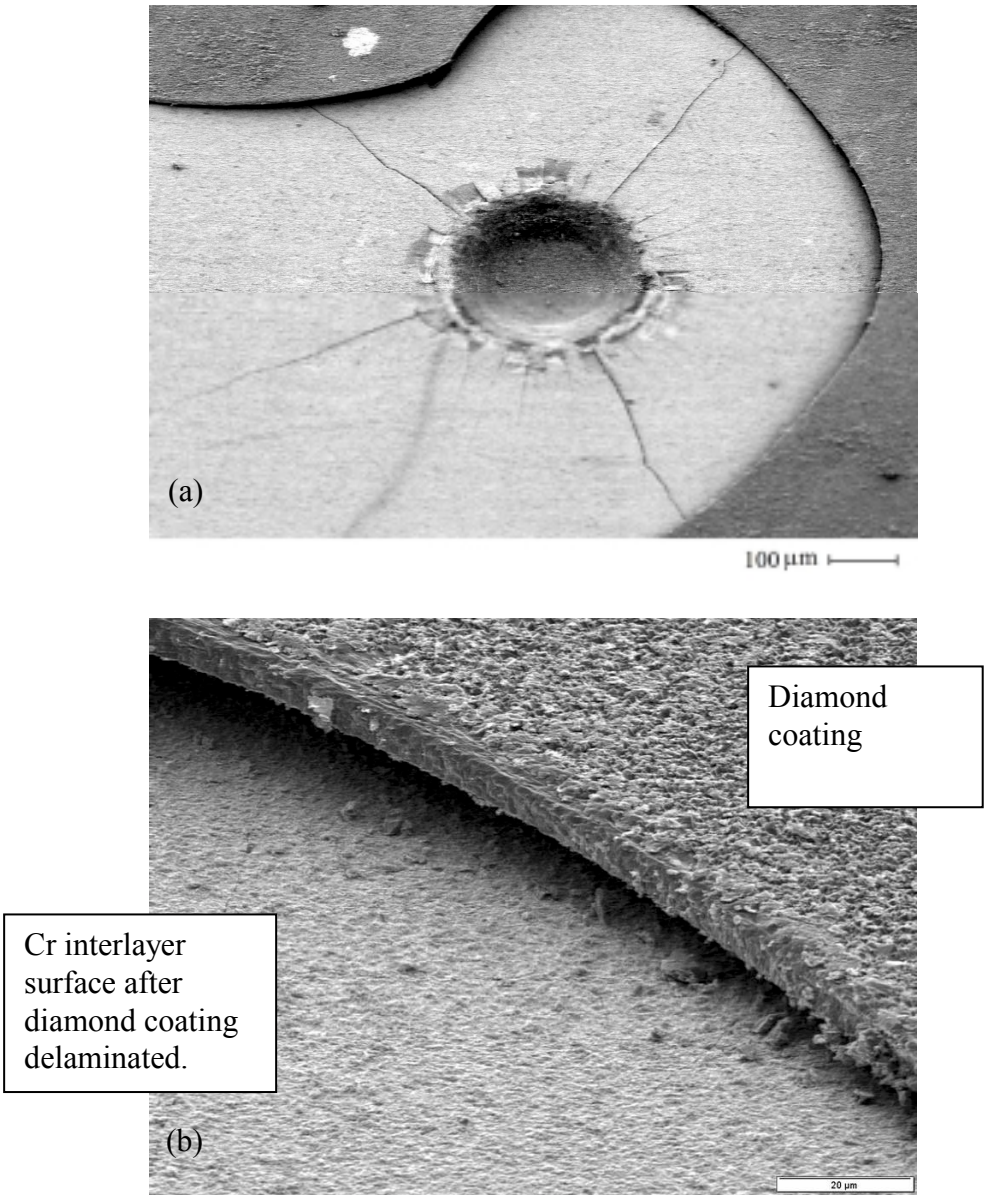

Figure 4.11: SEM micrographs of the Rockwell C indentations without surface peening pretreatment.

Figure 4.12 shows the SEM micrograph of the Rockwell indented region on the peened sample. Compared to the previous one, the extension of delamination was much lower in the case of peened sample. Nearly no diamond film flaked off or detached outside the indentation zone, indicating strong adhesion strength. During indentation, the film and the substrate deformed together up to the point of adhesive failure of the

interface. Two kinds of cracks, concentric and radial, are initiated and propagated due to the different deformation response of the coating/interlayer/substrate system upon indentation. Upon further loading, the crack growth can occur towards the interface and lead to interface delamination (*99*). It is known that the crack length reflects the ease with which the lateral crack propagates (*100, 101*). The crack length of the diamond film on un-peened sample is around 400 μm while that of the diamond film on peened sample is only 150 μm. Much higher adhesion strength has been obtained from the short peened sample.

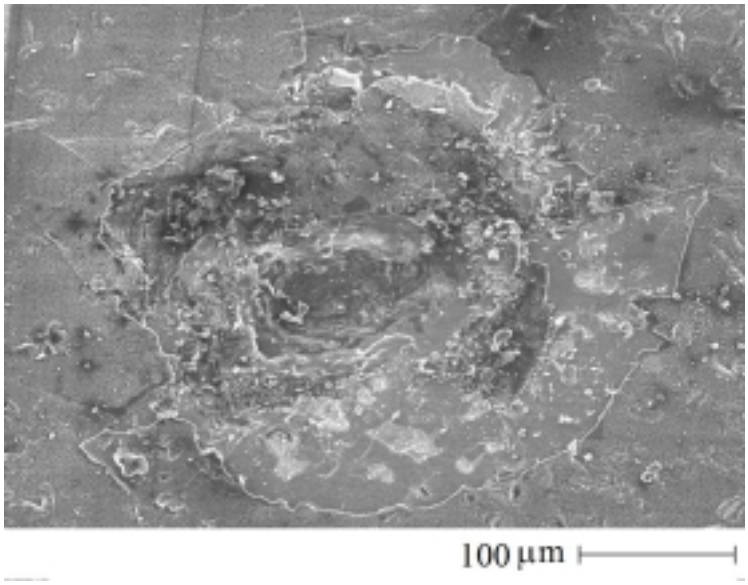

Figure 4.12: SEM micrographs of the Rockwell C indentations with surface peening.

Coating adhesion can be investigated qualitatively using Rockwell indent method. The diamond-coated surface was indented by a Rockwell indenter with a force of 60, 100, and 150 kg. The slopes of the indentation load versus the lateral crack diameter are generally used to evaluate the adhesion of the films because the lateral cracks are proportional to 1/Gc, where Gc is the critical strain energy release rate. Higher slopes

indicate lower adhesion level. From SEM micrographs, shown in Figure 4.13, the lateral crack length is about 240, 370, 620 μm for 60, 100, 150 Kg load, respectively. The residual stress in the coating was found independently to be approximately 3 GPa. According to Drory and Hutchinson's model (*100*), for 9 μm thick film with 3 GPa residual stress, it can be calculated that the effective interface fracture toughness, Gc, is around 48 J m-2. This toughness value represents a reasonably strong interface bonding and is comparable with that of diamond coating deposited on Ti alloy substrates.

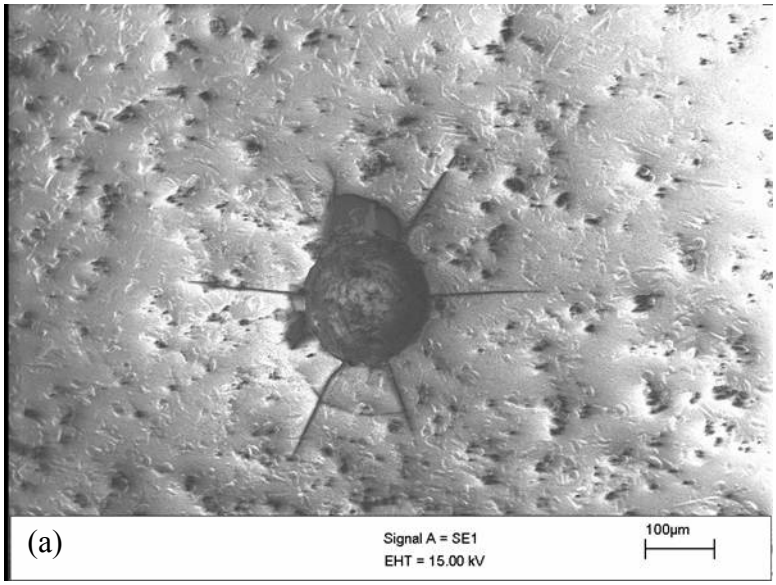

Figure 4.13: SEM micrographs of diamond coating indented by a Rockwell indenter under a load of (a) 60 kg; (b) 100 kg; (c) 150 kg.

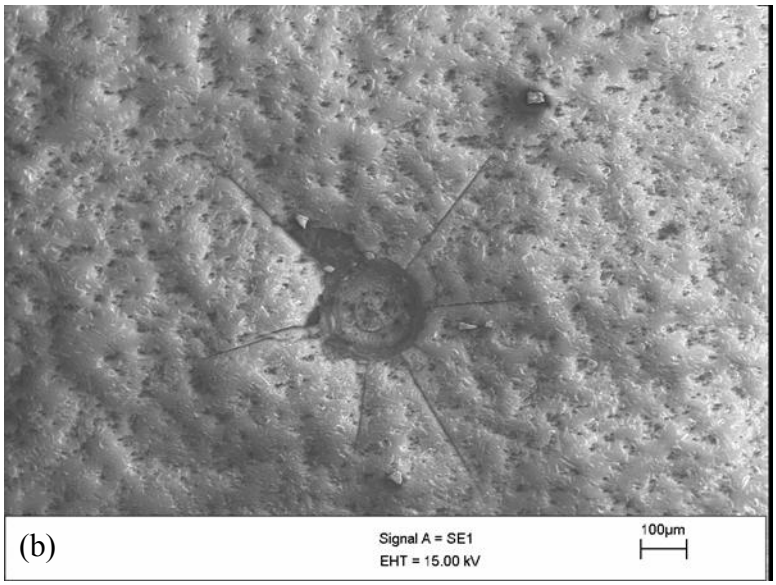

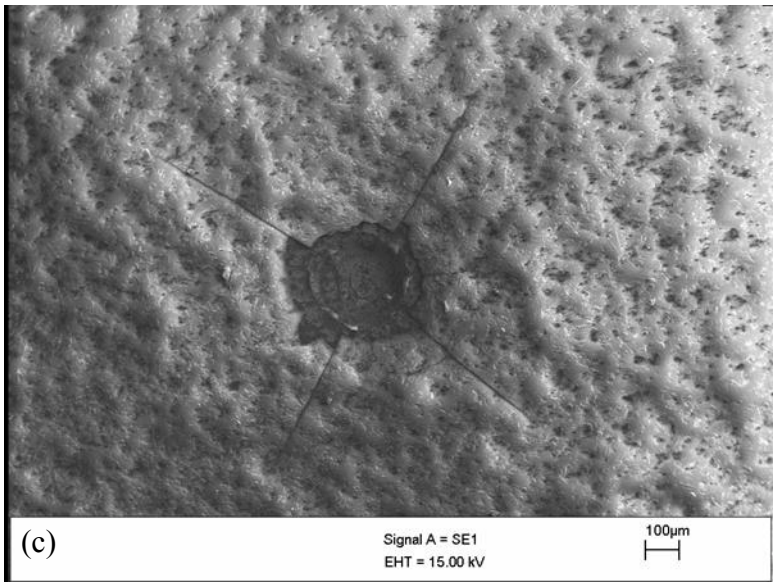

Figure 4.13: (Continued).

The indentation area, shown in Figure 4.12, with the associated delamination surface of the short peened and interlayer coated sample was analyzed by EPMA. C, Cr, W and Co Ka x-ray mappings are shown from Figure 4.14 a-d, respectively. Figure 4.14a shows that after the indentation test the major part of the diamond coating is still left on

the surface. Figure 4.14b shows that the majority of the delamination area is covered with Cr suggesting that the delamination occurs at the diamond/Cr interface. Thus, the adhesion between the interlayer and the substrate is probably stronger than the adhesion between the interlayer and the diamond coating. Neglecting the contribution of C and N, the semi-quantitative compositions of some of the failure surfaces contain more than 99 wt.% of Cr with less than 1 wt.% of Co and W. This suggests that delamination of the coating occurred mainly at diamond/Cr interface (not the Cr/CrN or Cr/WC-Co interface). Figure 4.14c and Figure4.14d show that Co enrichment could be observed only in the area where the WC-Co substrate is exposed. The exposure of cemented carbide is probably due to the damage of the interlayer during short peening since at pressure ~2000 Torr small diamond particles might penetrate the whole multi-interlayer and leave the substrate exposed. The condition of the short peening should be further optimized so that a proper surface roughness could be achieved whereas the interlayer should not be damaged at all.

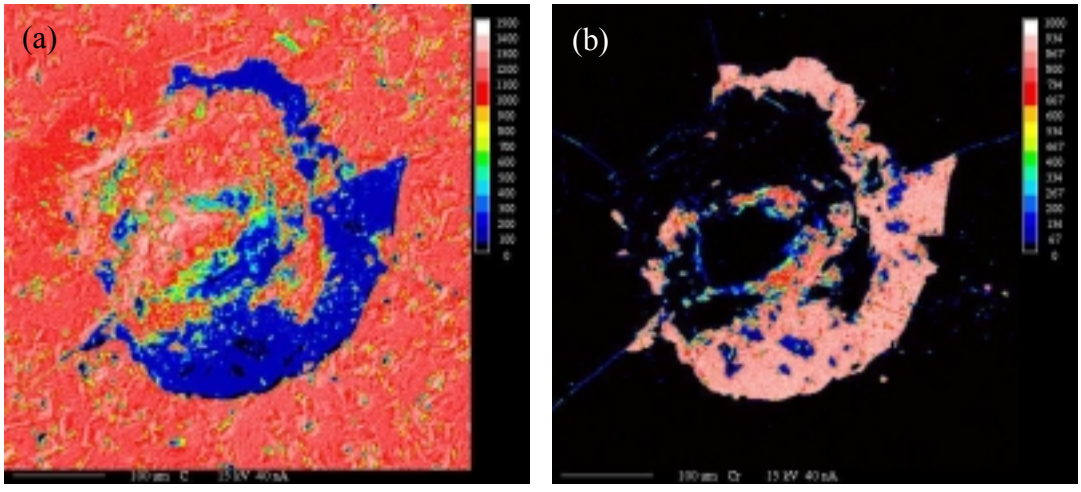

Figure 4.14: Electron probe microanalysis mapping of the Rockwell indentation region shown in Fig 5b. (a) C; (b) Cr; (c) W; (d) Co.

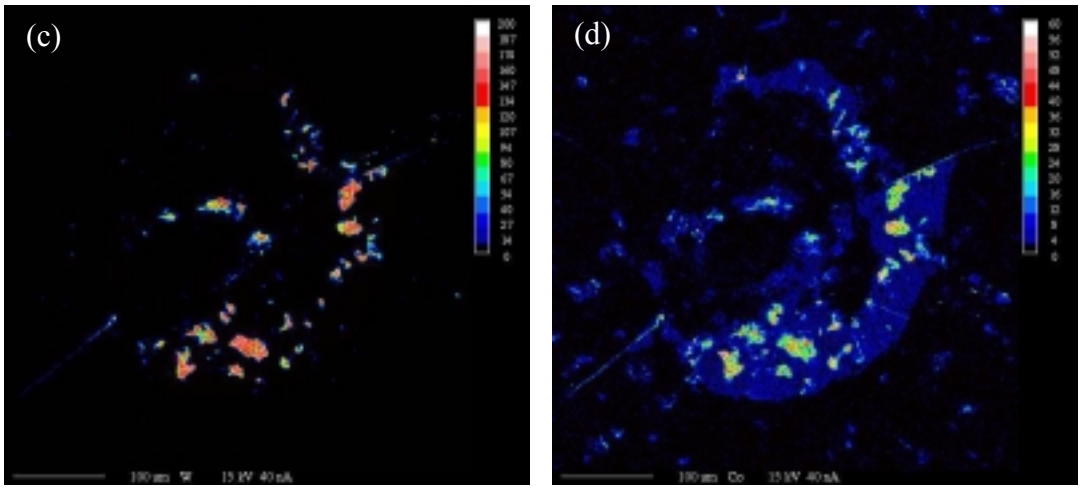

Figure 4.14: (Continued).

4.4 Residual Stress Analysis

4.4.1 Introduction

Diamond is considered as an ideal coating material for cutting tools with its unique characteristics, such as high hardness and wear resistance, good thermal conductivity, low friction and low coefficient of thermal expansion (CTE). However, poor adhesion between the diamond coating and the substrate resulting in coating delamination is the main obstacle for wide application of diamond coated tools. One of the reasons of poor adhesion is that high residual stresses inside the coating affects its micro hardness, wear resistance, and most importantly for diamond coating, the adhesion strength (*86, 87*). Hence, in order to understand the origin of the residual stresses and their variation due to process parameters and coating thickness, it becomes very important to produce highly adherent diamond coatings with low residual stress. It is common to separate the total residual stress into a thermal stress and an intrinsic stress component. The thermal stress is due to different CTE of the coating and the substrate during cooling down from high diamond deposition temperature, while the intrinsic stress is associated

with the film growth, structural defects and nondiamond materials at the grain boundaries. Residual stresses in thin films are typically measured by curvature measurements (*102*), X-Ray Diffraction (XRD) (*103*) and Raman (*104*) peak shift methods. Curvature method measures the sample curvature before and after deposition and the total residual stress could be calculated by the aid of Stoney's equation (*105*). Raman spectroscopy is a simple technique to evaluate the residual stress through diamond Raman peak shifts. However, multi-peaks attributed to peak splitting due to a degeneracy of the optical phonons may appear. The domain size effect [10], observed by line shape, may also gives difficulties for quantitative evaluation of the residual stresses. $Sin^2\psi$ technique is usually applied to obtain the residual stress by XRD. Compared to Raman spectroscopy, XRD allows measuring the residual stress over a large area and through film's whole depth.

Many studies have been conducted for diamond deposition for cutting tool applications (*95, 106, 107*), but very few references in the literature could be found on the residual stress analysis of diamond coatings grown on cemented tungsten carbide substrates. A better understating of the residual stress would allow more successful development of diamond coated tools with stronger adhesion strength and longer tool life. In this paper, we have investigated the relationship between the residual stresses in diamond films and the film thickness. A series of diamond films with thickness varying form 1.5 to 16.5 μm has been deposited on WC-Co substrates. In the first set of experiments, all growth conditions were maintained constant for all experiments. The only variable parameter was the growth time to obtain different film thickness. The optimal film thickness has been obtained to produce coating with low compressive

residual stresses. Comparisons of residual stresses obtained by three different methods have been discussed. In the second set of experiments, different percentage of methane has been utilized during deposition and the total residual stress as a function of methane concentration has been studied.

4.4.2 Experimental

1.9 mm x 37 mm thin rectangular cemented carbide samples (6 wt. % Co) were selected as the substrate for diamond growth. Substrates were first cleaned by acetone and methanol in an ultrasonic bath for 10 min. A thin Cr/CrN/Cr multi-interlayer system was deposited by an unbalanced magnetron sputtering system. This interlayer system works as a diffusion barrier to prevent Co leaching during CVD process. In order to achieve certain surface roughness to improve nucleation and adhesion, diamond powders peening of the substrates was carried out by a Raytech sandblasting machine. Diamond films were deposited by an ASTeX Microwave Plasma Enhanced Chemical Vapor Deposition (MPECVD) system. Hydrogen and methane were used under the following conditions: microwave power, 800 W; substrate temperature, 700 °C; pressure, 80 Torr; gas composition, H_2:CH_4 (mass flow rate: 500/5 sccm); deposition time, 1-12 h. The process conditions utilized here ensure the formation of continuous films on the substrate surface. Low temperature growth, as compared to 850 – 950 °C which is normally used, not only minimizes the thermal residual stress but also lessens the mobility of the cobalt, and results in a relatively more adherent film. The residual stress as a function of film thickness and methane concentration has also been investigated.

4.4.3 Results of different stress measurements

The thickness and surface morphology of the diamond coating was obtained from SEM micrographs. As the diamond growth time varied from 1.0 to 12.0 h, the film thickness increased from 2.0 to 16.5 μm and the grain size increased from 0.4 to 4.1 μm. Figure 4.15a shows the top view SEM micrograph of the diamond film deposited for 12 h. The surface morphology shows predominantly faceted pyramidal grain characteristics of the (111) textured growth. The average grain size of the film is around 4 μm. The cross sectional view SEM micrograph of this film is shown in Figure 4.15b. Columnar growth could be clearly observed and the film thickness is around 16.5 μm.

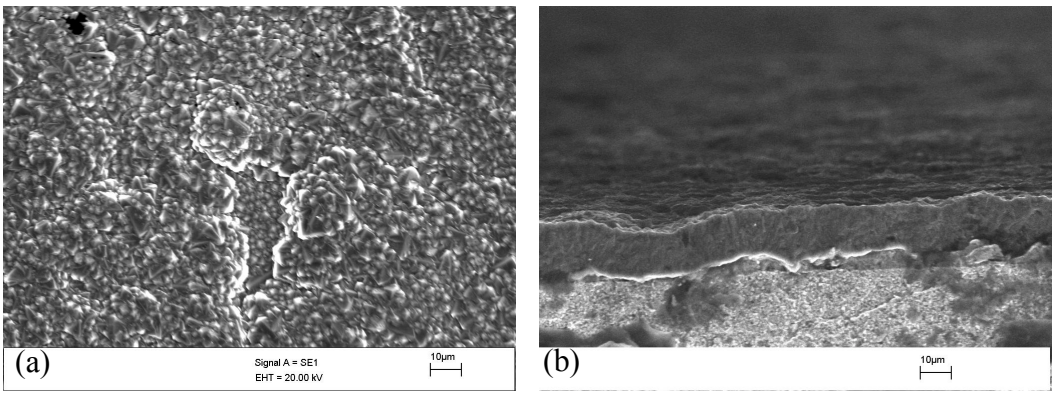

Figure 4.15: SEM micrographs of diamond film deposited on WC-Co substrate for 12 h. (a) top view of the coating; (b) cross sectional view.

The film thickness as a function of the growth time and the grain size as a function of the film thickness are plotted in Figure 4.16a and Figure 4.16b, respectively. A linear relationship between the film thickness and the growth time, as well as the grain size and the film thickness could be approximated.

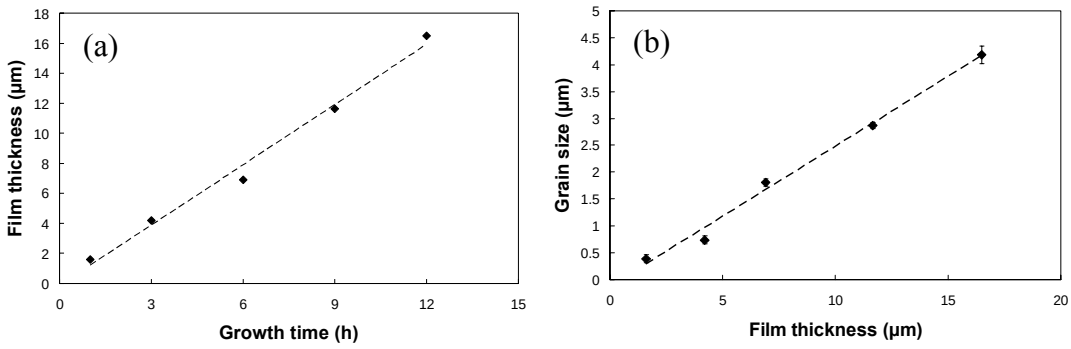

Figure 4.16: Diamond film growth on WC-Co. (a) Diamond film thickness as a function of growth time. (b) Diamond grain size as a function of film thickness.

4.4.3.1 Thermal stress

During cooling down from high growth temperature to room temperature, a thermal stress was built up due to the difference of CTE between the diamond coating and the WC-Co substrate. The analytical solution for the thermal stress in the samples could be computed by the following equation:

$$\sigma_f = \int_{T_0}^{T} \Delta\alpha \cdot \frac{E_f}{1+\upsilon} dT \qquad \text{(vi)}$$

Where E_f is the elastic modulus of the diamond coating, $\Delta\alpha$ is the difference of the CTE between the diamond film and the substrate, v is the Poisson's ratio, T is the deposition temperature and T_0 is the room temperature. For a typical low deposition temperature of 700°C, using the value of the biaxial Young's modulus, E/ (1-v), a thermal stress of about -3.48 GPa is calculated. Therefore, the intrinsic stress could be obtained by subtracting the thermal stress from the total residual stress.

4.4.3.2 Curvature method

A stressed thin film attached to a substrate imposes a curvature upon the substrate. This problem was first studied by Stoney. For elastically isotropic film/substrate systems where the film thickness, h_f, is uniform and much smaller than the substrate thickness, h_s, and the lateral dimensions are much larger than the thickness, following modified Stoney's equation (*108*) relates the curvature to the film stress:

$$\sigma_f = M_s \cdot \frac{h_s^2}{6h_f} \cdot \left(\frac{1}{R} - \frac{1}{R_0}\right) \cdot \left[1 + \frac{h_f}{h_s} \cdot \left(\frac{4M_f}{M_s} - 1\right)\right] \qquad \text{(vii)}$$

where M_s and M_f are the biaxial Young's modulus of the substrate and diamond film, R and R_0 are current and initial radii of sample's curvature. The substrate and the film thickness were measured on SEM cross sectional micrographs. Wyko optical profilometer was utilized to measure sample's curvature.

Figure 4.17 shows the plot of the total residual stress and the intrinsic stress as a function of film thickness from curvature measurements. It could be observed that the total residual stress starts tensile at a value of 1.85 GPa. It changes from tensile to compressive for films thicker than 3.7 μm and remains compressive for all the other samples. Note that the intrinsic stress, obtained by subtracting the thermal stress from the total residual stress, is always tensile.

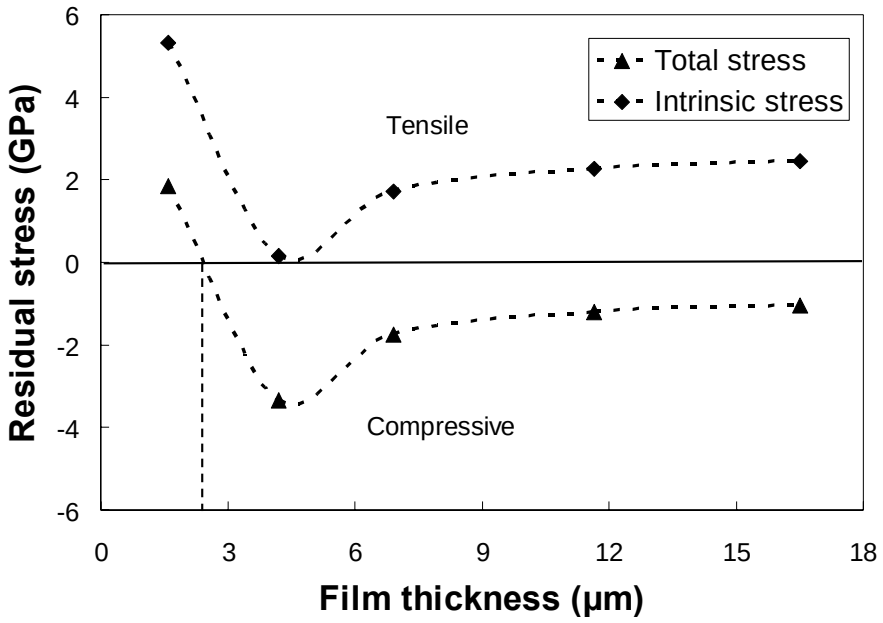

Figure 4.17: Total residual stress and intrinsic stress as a function of film thickness measured by curvature method.

4.4.3.3 XRD method

XRD is an important and non-destructive measurement technique that allows evaluating the residual stress over a large area (*109-111*). In additional, the high penetration depth of X-ray allows the measurement through the whole depth of the film. XRD measurements were performed by a Siemens D-500 diffractometer with a Cu X-ray tube. A 5.0 mm slit for the incident beam and a 1 mm receiving slit before the detector were selected for our purpose. The $\sin^2\psi$ method consists of measuring the lattice spacing d of a specific plane at different tilt angles ψ (inclined exposure). In this study, we choose (220) lattice plane to determine the residual stress. The θ/2θ scans were performed around (220) Bragg diffraction peak (2θ~75.6°) at tilt angles ψ between 0° and 35° for all the samples. The residual stress can be obtained from following equation

$$\frac{d_\psi - d_0}{d_0} = \frac{1+\upsilon}{E} \cdot \sigma_{total} \cdot \sin^2 \psi \qquad \text{(viii)}$$

where d_ψ is the lattice spacing at each ψ, and d_0 is the spacing when ψ=0°.

Figure 4.18 shows the plot of lattice spacing d_ψ versus $\sin^2\psi$ for the 12 h deposition sample. The linear behavior of the curve indicates a homogeneous stress in the film, and $\sin^2\psi$ method could be used for stress estimation. Note that the negative slope suggests that a compressive residual stress exists in the film. The value of $(d_\psi - d_0)/d_0$ was calculated and then plotted as a function of $\sin^2\psi$.

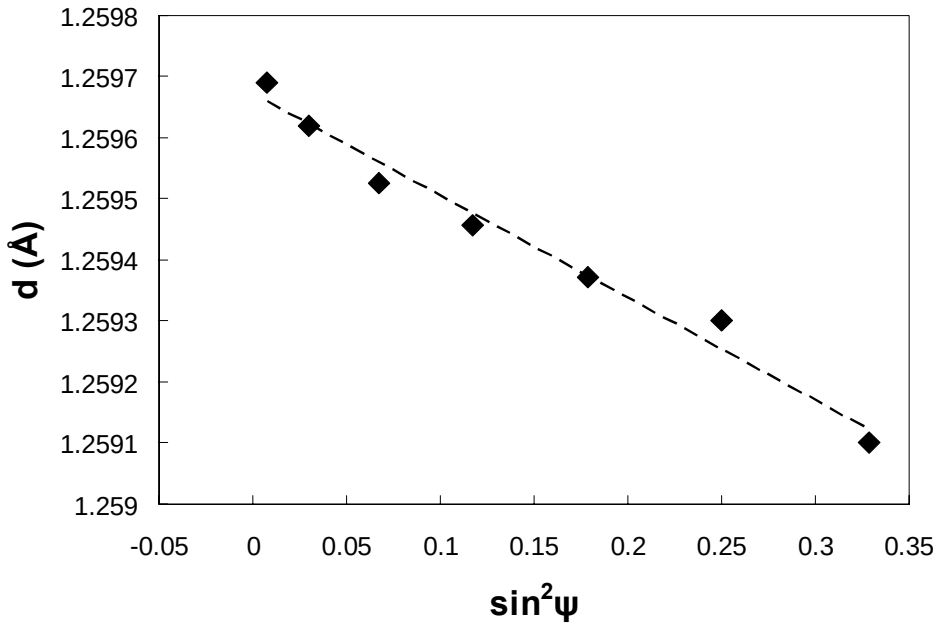

Figure 4.18: Lattice spacing versus sin2ψ for diamond film grown for 12h.

The total residual stress could be obtained from the slope using equation (3). The total residual stress as a function of film thickness, plotted in Figure 4.19, starts around 0.75 GPa (tensile) and then changes from tensile to compressive for film thicker than 2 μm and remains compressive up to film thickness of 16.5 μm. The high value of thermal

stress is the main reason for films showing compressive stress. Same as the curvature method, the intrinsic stress could be obtained by subtracting the thermal stress form the total residual stress and remains tensile for all the samples.

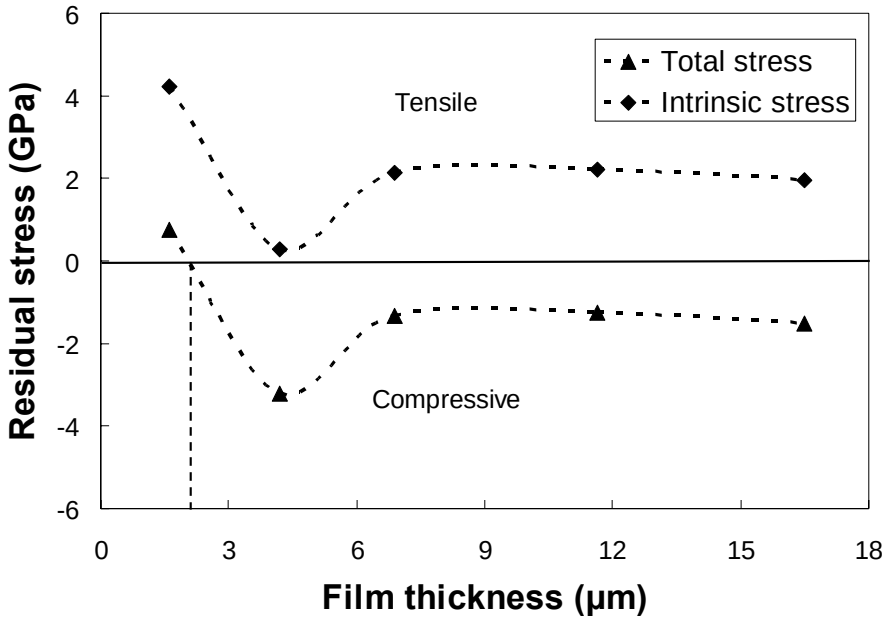

Figure 4.19: Total residual stress and intrinsic stress as a function of film thickness measured by XRD method.

4.4.3.4 Raman spectroscopy method

The micro Raman spectra were recorded by a Renishaw-1000 microscopy system using an argon-ion laser excitation line (514.5nm). It is well known that the shift of diamond Raman peak is related to the total residual stress in diamond films (*112-114*). Due to the possible inhomogeneous stress, five measurements have been taken at different locations for each sample. For each point, the spectra were scanned three times to minimize the effect of inhomogeneity. The stress could be related to the position of diamond peak by the following equation.

$$\sigma_f = -M_f \cdot \frac{\omega - \omega_0}{\omega_0 \gamma} \qquad \text{(ix)}$$

where ω_0 and ω are the position of the diamond peak under stress-free and stressed condition respectively, and γ is the Gruneisen parameter of the diamond (0.94~1.19). The diamond peak positions were averaged for all the measurements and found by curve fitting using software provided by Renishaw. Position of the stress free diamond peak is at 1332.5 cm^{-1}. The total residual stress as a function of film thickness is plotted in Figure 4.20. It could be seen that all the films exhibit compressive stresses. The error bars were evaluated from the standard deviation of all the data taken from Raman measurements.

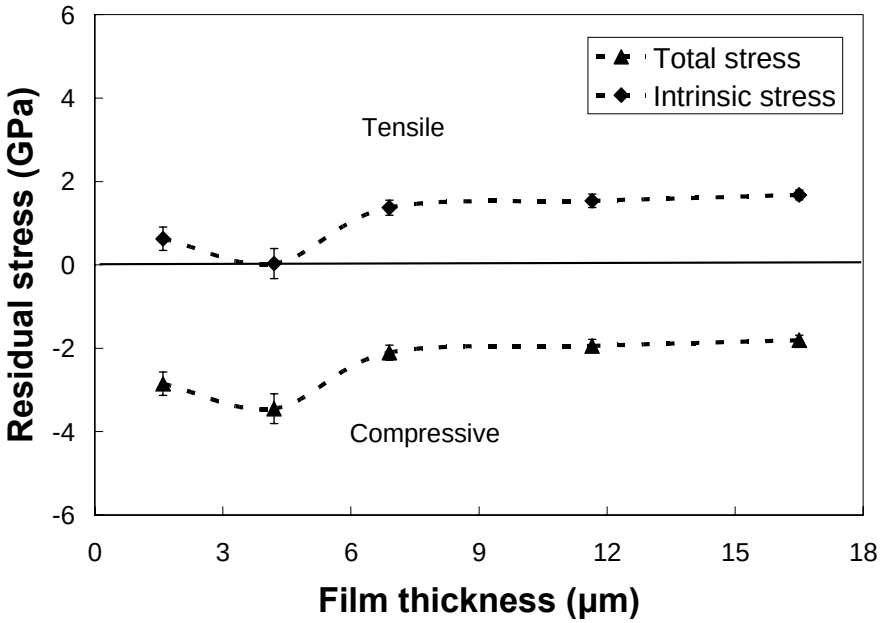

Figure 4.20: Total residual stress and intrinsic stress as a function of film thickness measured by Raman peak shift method.

4.4.3.5 Residual stresses as a function of CH_4 concentration

Diamond films grown with high methane concentration contain more nondiamond impurities. The intrinsic tensile stress would be relaxed by nondiamond phase in grain

boundaries. Therefore, the total residual stress of the film would increase if more methane is included during deposition. In our experiments, diamond films were deposited for 6 h with 1, 2, 3 % methane concentrations, respectively. Figure 4.21 shows the dependence of total residual stress in diamond films on methane concentration. Note that in some literature it is reported that the modulus of the diamond film decreases with increasing nondiamond content (*115*). However, the change of modulus is neglected in our calculations since it is relatively small compared to the change of the total residual stress, and hence does not effect the conclusion that less methane concentration results in films with lower total residual stress.

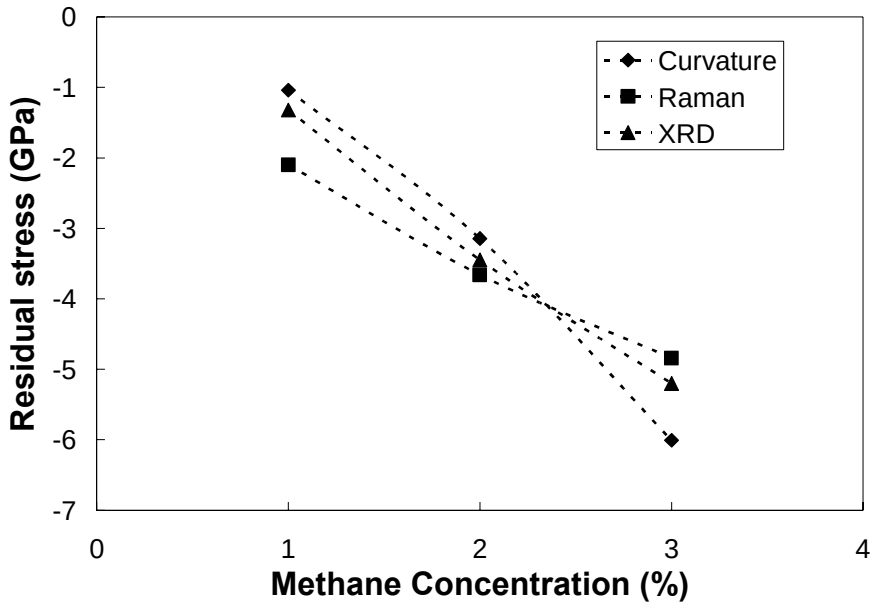

Figure 4.21: Total residual stress in diamond film as a function of methane concentration measured by Raman peak shift.

4.4.4 Discussion

The comparison of the total residual stress obtained from three different methods has been plotted in Figure 4.22. Note that for films thicker than 4 μm, due to large

mismatch of CTE, a compressive stress is dominant in the films because of the thermal stress. For film thinner than 2 μm, both curvature and XRD measurements show tensile while Raman measurement shows compressive. It is believed that this kind of divergence is associated to the domain size effect from different measurement techniques. For XRD and curvature measurements, residual stresses were obtained over a large area of sample through the whole depth of the film while micro-Raman spectroscopy could only measure relatively small area, only within 2.0 μm spot size in our case. So for film deposited for 1 h, the grain size is only around 0.3 μm, relatively smaller compared to the Raman spot. More grain boundaries were picked up by Raman measurements while the contribution of grain boundaries to the film is always compressive. On the other hand, curvature and XRD measurements show tensile stress due to large intrinsic stresses in the early stage of growth. The intrinsic tensile stress is believed to be associated with the coalescence of isolated grains into a continuous film. In the early stage of growth, when two free surfaces were converted into a grain boundary, tensile stresses are introduced to pull the two surfaces together in adjacent islands. After individual islands coalesce into a dense film, compressive stresses developed from thermal stresses become dominant which agrees with our experiment results. Analysis has been focused on the films produced with CH_4 variations, and higher residual stress is obtained for film deposited with more CH_4 concentration. The decrease of intrinsic tensile stress could be attributed to the nondiamond content produced at higher CH_4 concentration.

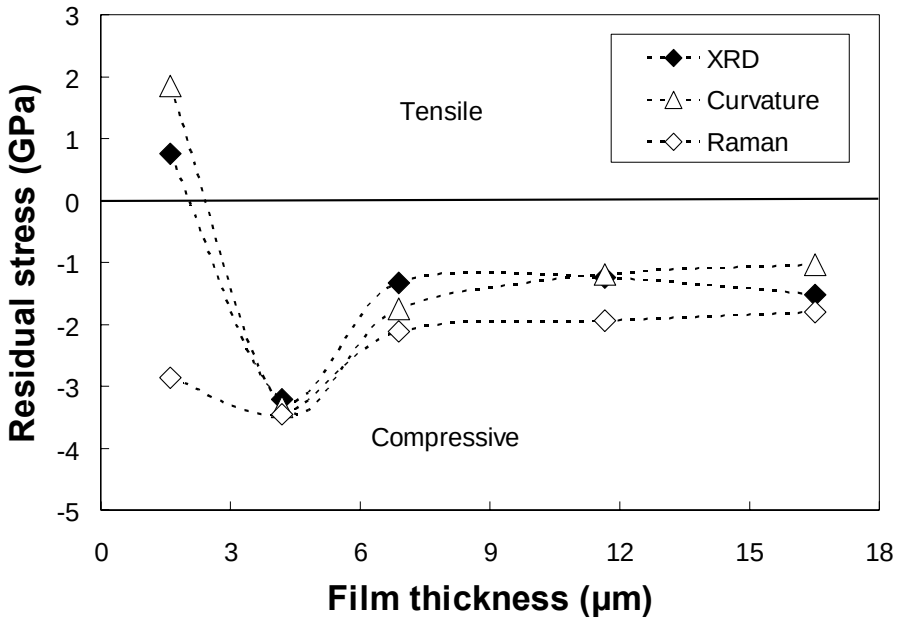

Figure 4.22: Comparison of the total residual stress between curvature, XRD and Raman measurements.

4.5 Results of Pin-on-disk Test

The diamond coated sample on blasted WC-Co/Cr substrate was also tested on a pin-on-disk machine. This pin-on-disk machine was used to test the wear resistance of the coating. The sample was fixed on the machine and rotated continuously. An aluminum pin rode on a diamond-coated surface is used to test the wear resistance of the sample. Figure 4.23 shows the wear track covered by aluminum after the test.

Aluminum was observed filling the valleys between the diamond grain peaks Figure 4.23a. Small chips and chunks of aluminum stuck between the diamond grains. After more than 40,000 rotations of pin-on-disk machine there was no wear of the diamond coating. The smallest wear that could have been detected in our SEM observations was less than 20 to 30 nanometers. However, no wear was observed, and the

diamond grains remained very sharp after the test (Figure 4.23b). This suggests that the diamond coating on a machining tool is likely to last for a long time.

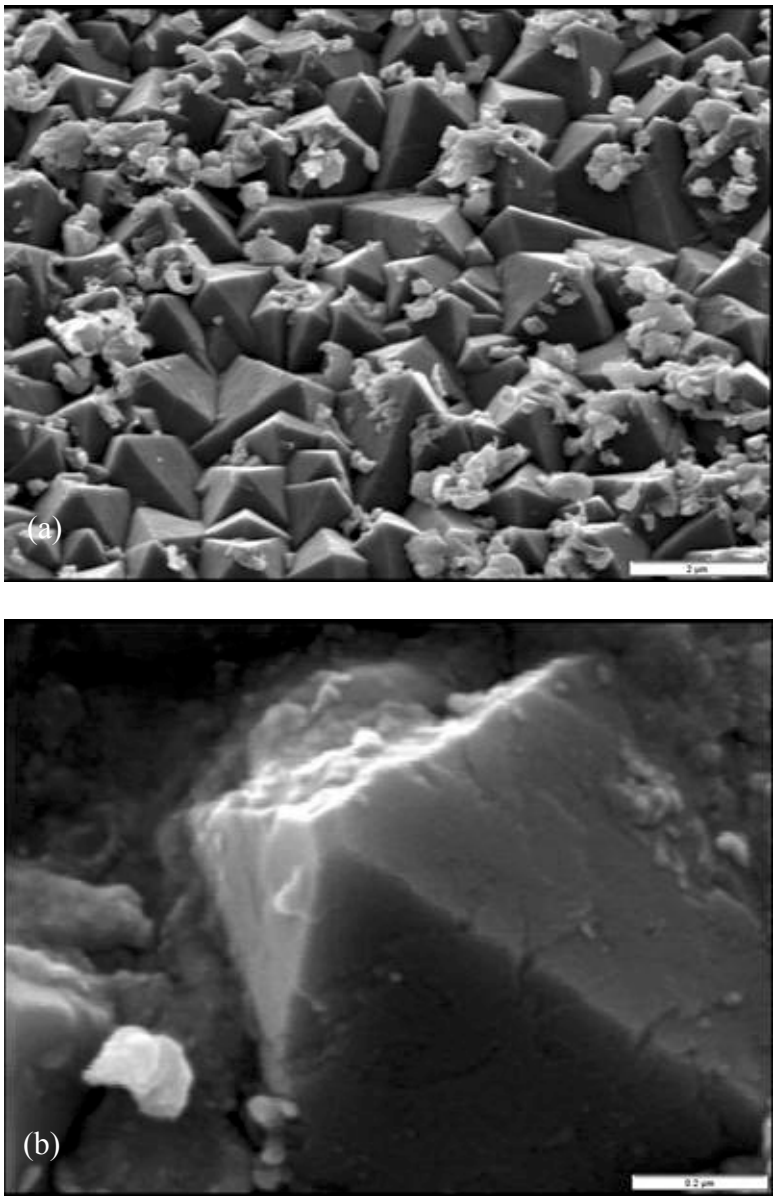

Figure 4.23: SEM micrographs of diamond after pin-on-disk test. (a) Diamond coating on cemented carbide substrate with a wear track; (b) diamond grain in the wear track after 400,000 rotations against an aluminum pin.

The coefficient of friction (COF) of the diamond film is around 0.23, shown in Figure 4.24. Note that the pin-on-disk experiment conditions are list as following: 10N load, 40,000 circles, linear speed 54.24 cm/s.

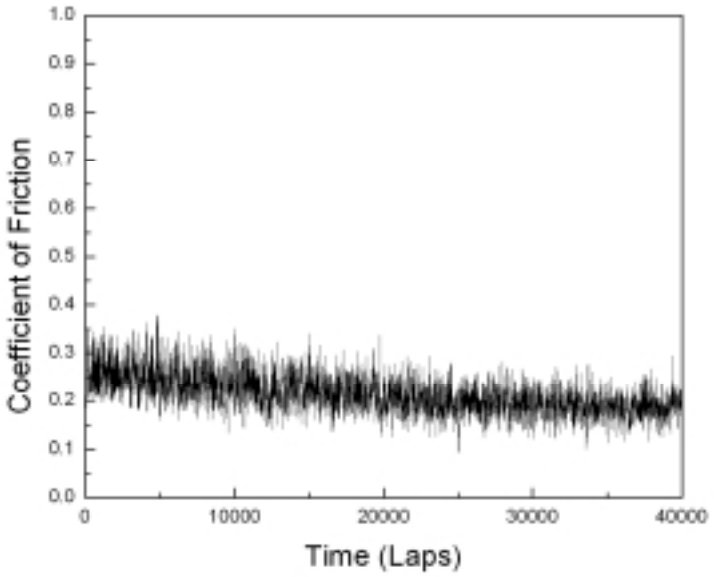

Figure 4.24: Coefficient of friction of diamond coating deposited on WC-Co substrate.

4.6 Summary

Well-adhered microcrystalline diamond (MCD) coatings have been deposited on WC-Co substrates by the microwave plasma enhanced chemical vapor deposition (MPECVD) method. A multi-interlayer system Cr/CrN/Cr was deposited on the cemented carbide substrate before diamond deposition to act as a diffusion barrier. The interlayer coated substrate was shortly peened by friable diamond powders with an average size of 150 μm to roughen the surface. Diamond coatings deposited on short peened substrates show higher nucleation density and stronger adhesion properties. The X-ray diffraction (XRD) pattern showed that an additional carbide compound layer (Cr_3C_2 and Cr_7C_3) was formed during the CVD diamond deposition to work as an intermediate bonding layer for

better adhesion. Rockwell indentation tests with a load of 1470 N were conducted to investigate the coating's adhesion. No delamination outside of the indentation zone was observed for the diamond coating deposited on the roughened sample. Electron probe microanalysis (EPMA) results showed that the delamination in the indentation zone occurred mainly at the diamond/Cr interface and very little Co (less than 1 wt. %) was detected on the Cr failure surface. This suggests that during the CVD process Co/C inter-diffusion was successfully prevented by the Cr/CrN/Cr buffer layers. Residual stresses in diamond films have been investigated by curvature, Raman, XRD methods. It has been found that for film thicker than 7 μm, the total residual stress in the coating reaches steady state with small compressive value around 1.8 GPa. For film thinner than 2μm, compared with other two techniques, Raman measurements show different type of residual stress due to the domain size effect. XRD and curvature measurements agreed very well for all the samples. The intrinsic stresses inside films were found always tensile. Film deposited with small fraction of methane has less total residual stress and is more suitable for cutting tool applications.

CHAPTER 5:

NCD ELECTRODES FOR BIOMEDICAL APPLICATIONS

5.1 Introduction

It is only recently that the outstanding properties of diamond as an interface to biological molecules and biological systems have been recognized (*58, 61*). The nanocrystalline diamond (NCD), with its unusual chemical, physical, electrical and biocompatible properties, has attracted much attention due to the need of a robust and stable bio interface for implantable biosensors that could work in physiological environment with comparatively harsh conditions.

Doping of diamond has attracted much attention with the development of CVD techniques. Most doped diamond depositions system use micro-wave-assisted CVD, which minimizes the film contamination with other materials. A special aspect of diamond is its capability of revealing a negative electron affinity (NEA) (*116-118*). NEA means that electrons can exit from conduction band edge into vacuum without further energy barrier. The only way to take advantage of this NEA is to form ohimic or tunnel contacts by n-type doping diamond. So far, nitrogen (*119*), sulfur (*120*) and phosphorus (*121*) have been used to produce n-type diamond.

There is a large volume of research in the area of implantable glucose sensors, which are intended to operate inside the body for either temporary or long-term glucose detection (*122, 123*). Generally, most of the glucose biosensor electrodes are made with

carbon (*124*) or noble metal electrode substrates such as Au or Pt (*125, 126*). Besides these materials, diamond is especially attractive since, in addition to having good electrical (*127*) and chemical properties (*51*), it is also biocompatible, and can be deposited on silicon substrates that are compatible with microelectronics processing. It has been reported recently that metal-modified boron-doped diamond (BDD) electrodes can be used for electrochemical analysis of glucose detection (*128, 129*). Copper-modified, nickel-modified and nickel-implanted BDD electrodes have been fabricated for glucose sensing. However, these metal-modified electrodes suffer from the problem of their low electrochemical stability. Moreover, since most of the noble metals are poisonous to human body these sensors lack the bio-compatibility to be used in vivo.

The electrochemical measurement involves the measurement of an electrical signal (e.g., potential, current or charge) associated with the oxidation or reduction of a redox analyte dissolved in solution, and relating this signal to the analyte concentration (*53*). Diamond electrodes possess a number of unique electrochemical properties compared to other sp^2 bonded carbon electrodes including linear dynamic range, limit of quantitation, fast response time and response stability.

Figure 5.1 shows the design of a typical cell used for electrochemical measurements (*130*). The three-neck cell is constructed of glass. Three electrodes, diamond working electrode, counter electrode (Pt) and reference electrode (Ag/AgCl), are clamped to the bottom of the glass cell. Diamond film is placed on the bottom of the cell and ohmic contact is made on the back side of the substrate for measurement.

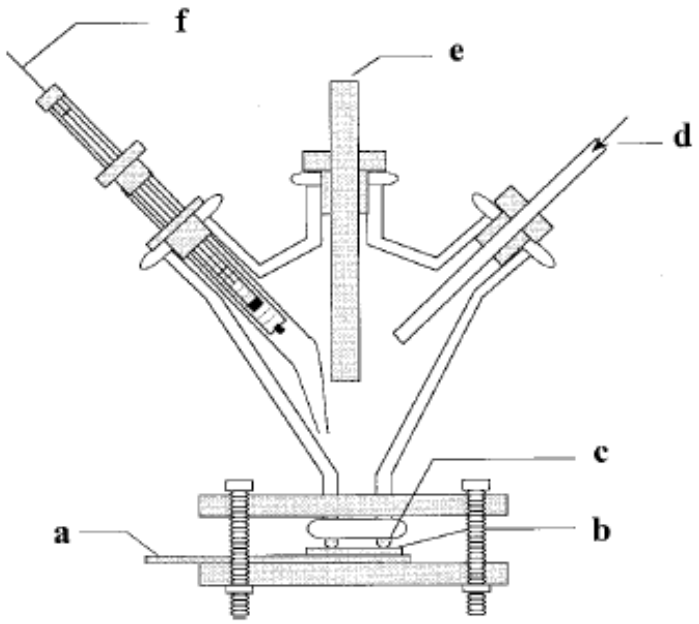

Figure 5.1: Diagram of the single-compartment, glass electrochemical cell used. (a) Cu or Al metal current collecting plate, (b) diamond film electrode, (c) Viton O-ring seal, (d) input for nitrogen purge gas, (e) carbon rod or Pt counter electrode, and (f) reference electrode inside a glass capillary tube with a cracked tip (*131*).

The nitrogen doped electrically conductive NCD films has been obtained by adding N_2 gas to Ar/CH_4 during deposition. The film deposited form $Ar/N_2/CH_4$ mixtures are a little rougher morphologically with an average cluster size of 150 nm. This kind of NCD films also possesses good electrochemical activity without any conventional pretreatment. They exhibit semimetal-like electronic properties over a wide potential range from at least 0.5 to -1.5 V vs. SCE, shown in Figure 5.2. It is clear that the responses of the electrodes are independent of the level of nitrogen doping. For all the film the background currents are mostly featureless within this potential range. Generally, disordered carbon electrodes exhibit oxidation and reduction peaks between -200 and 500 mV due to the formation of carbon-oxygen functionalities. But only very small anodic

and catholic peaks could be observed for NCD films. It is suggested that the low back ground current of diamond is attributed to two factors: a reduced pseudocapacitance from the absence of redox-active and or ioniable surface carbon-oxygen functional groups, and a slightly lower internal-charge carrier concentration, due to the semimetal –like electronic properties (*53*). Wide potential working window has also been obtained for nitrogen doped NCD films. For 0, 2, 4, 5% N_2 doped films, they have working potential windows of 4.27, 4.05, 3.85, and 3.87 V (*57*), respectively. These windows are 1 V greater than what is usually observed for glassy carbon.

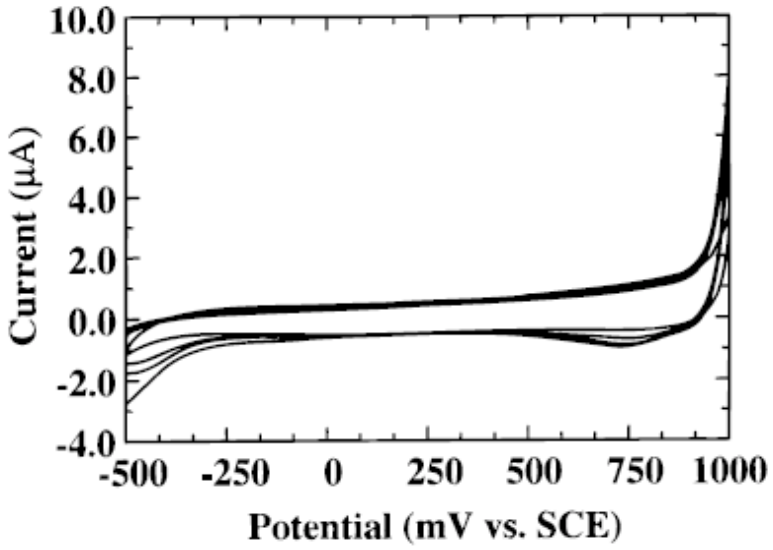

Figure 5.2: Cyclic voltammetric i-E curves of nanocrystalline diamond films (*57*).

The electrochemical detection of glucose has attracted many attentions in recent years due to its high accuracy, rapidity, low cost, simplicity and better detection limits. The most widely used electrochemical biosensors for glucose detection are the amperometric enzyme-based electrodes. The amperometric techniques are the most useful due to the possibility to obtain a signal linearly related to glucose concentration. This

linearity of the sensor response is of great importance for the sensitivity and selectivity of implantable glucose sensors (*132*).

In our study, we have immobilized glucose oxidase (GOX) onto a nitrogen-doped nanocrystalline diamond and used it as an electrode to directly detect the glucose in phosphate buffer solution. Compared to Boron-doped diamond, nitrogen-doped NCD exhibits a wide working potential window, a low back ground current and a good level of electrochemical response for electrochemical systems. There are several practical benefits of using nanocrystalline rather than microcrystalline diamond thin-films in electrochemistry, including the ability to deposit continuous films at nanometer range, easier coating of substrates with irregular geometries and the unique electrochemical behavior result from NCD film's different morphology and electronic properties compared to the microcrystalline films (*133*). Here, a glucose biosensor has been fabricated based on a modified nitrogen-doped nanocrystalline diamond electrode.

5.2 Experiments to Modify NCD Electrodes via Electrochemistry

Conductive nanocrystalline diamond thin films were synthesized on Si substrates using the 2.45 GHz microwave plasma enhanced chemical vapor deposition (MPECVD) system (ASTeX Corp.). Before the deposition, 0 to 0.5 μm diamond powders were used to polish the sample surface to increase the nucleation rate and the samples were ultrasonically cleaned in ethanol for 10 min. The films were grown under hydrogen-deficient conditions, using 1% CH_4, 79% Ar and 20% N_2 at 100 Torr pressure for 3 h. The temperature was kept at ~750ºC. Nitrogen gas was incorporated to make the films conductive. Films have been characterized by scanning electron microscopy (SEM) and

transmission electron microscopy (TEM). The conductivity of the nitrogen-doped NCD films was measured by four-point-probe method.

The schematic drawing of modification and functionalization of the diamond electrode surface is shown in Figure 5.3. After the deposition, the sample was first exposed to hydrogen plasma (750ºC, 30 torr) in MPECVD chamber for 30 minutes to terminate the surface with hydrogen. The hydrogenated sample was characterized by X-ray Photoelectron Spectroscopy (XPS). In order to achieve covalent immobilization of GOX, the NCD film was electrochemically functionalized in a 25 ml volume of 0.1 M sodium acetate acid to attach the carboxyl functional groups. A 25 µl volume of 0.1 M phosphate buffer solution containing 0.2mg (9.47 unit) GOX was coated onto the functionalized NCD electrodes at room temperature (20°C). The electrodes were stored in the dark at 4ºC for use. The electrochemical behaviors of the enzyme-modified electrodes were recorded by an electrochemical interface (Parstat 2263, Princeton Applied Research, USA). All the experiments were carried out in 0.1 M phosphate buffer solution (pH 7.2) with a three-electrode cell configuration. The modified NCD electrode was used as the working electrode, the Ag/AgCl electrode as the reference electrode and a platinum foil as the counter electrode. The geometric area of the working electrode was 60 mm^2. The scan rate used in cyclic voltammogram experiments was 50mV/s and the scan was performed between -0.8 to 0.8 V.

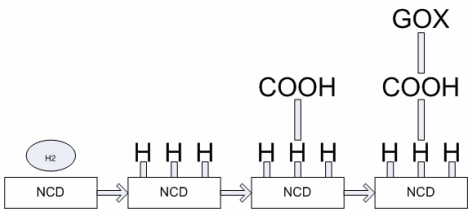

Figure 5.3: Schematic illustration of functionalization of NCD film.

5.3 Results of Electrochemical Modification

5.3.1 Nitrogen doping of NCD films

SEM micrographs of the nanocrystalline diamond films doped with 1 to 20 % N_2 have been shown in Figure 5.4. Continuous diamond nanocrystals have been observed. The thickness of the film was around 1.2 μm for 3 h deposition. The NCD film grown in Argon rich plasma has very low conductivity and could not work as an electrode in electrochemical analysis. To make the film conductive, it is necessary to incorporate nitrogen gas to the source gas mixture. It was found that both the grain size and the grain boundary-width increase with the addition of N_2. The average grain size of film doped with 20% N_2 is 2 to 3 times lager than film doped with 1% N_2.

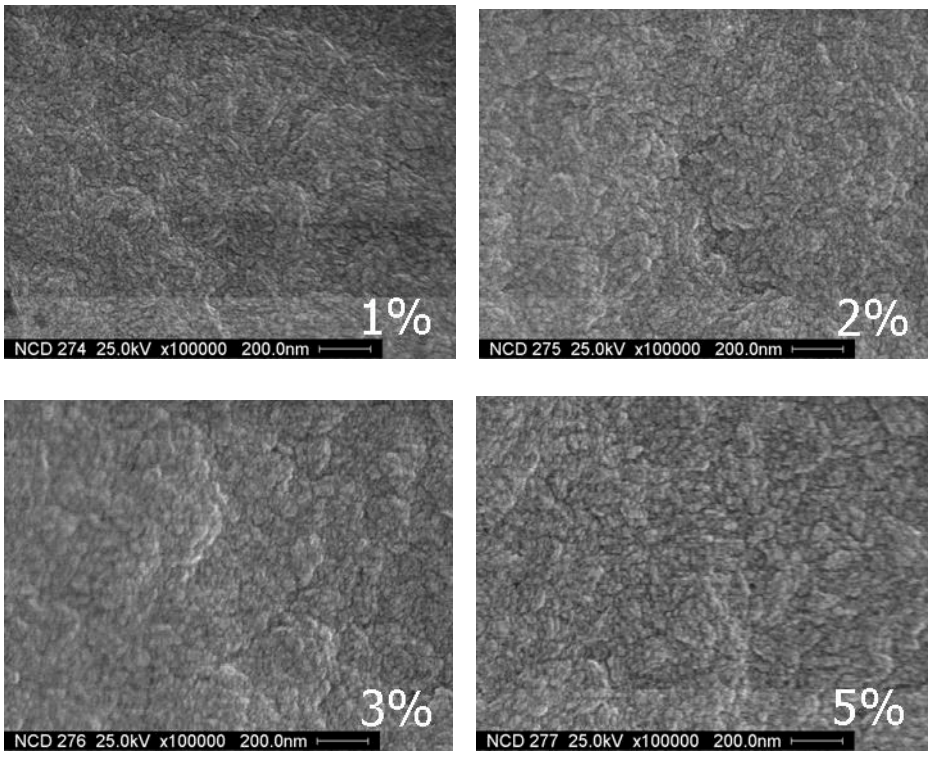

Figure 5.4: SEM micrographs of NCD doped with Nitrogen from 1% to 20%.

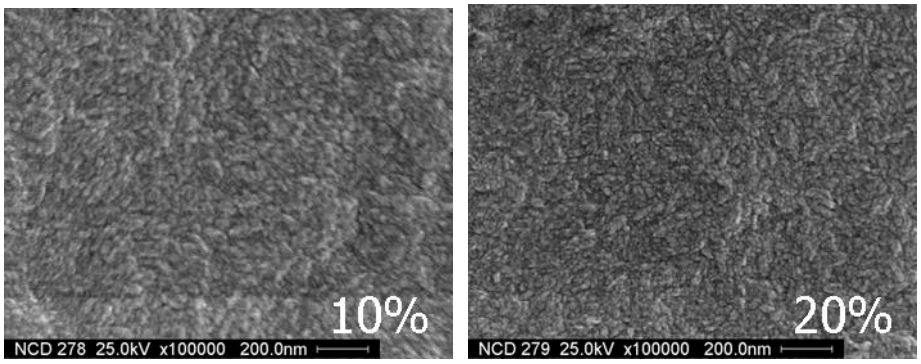

Figure 5.4: (Continued).

The incorporation of nitrogen introduces more sp^2 bonding in the grain boundaries and leads to better electrical conductivity. The dramatic increase of the conductivity was observed in Figure 5.5, increasing from 1.16 Ω^{-1} cm^{-1} (for 1% N_2) to 126.54 Ω^{-1} cm^{-1} (for 20% N_2), which represents an increase by roughly three orders of magnitude. Nitrogen-doped NCD differs from boron doped microcrystalline diamond mainly in its unique electrical properties. The nitrogen doping yields films with n-type semiconducting to semimetallic conductivities. Furthermore, the nitrogen-doped NCD possess some outstanding electrochemical properties especially its morphological stability and high electrochemical activity.

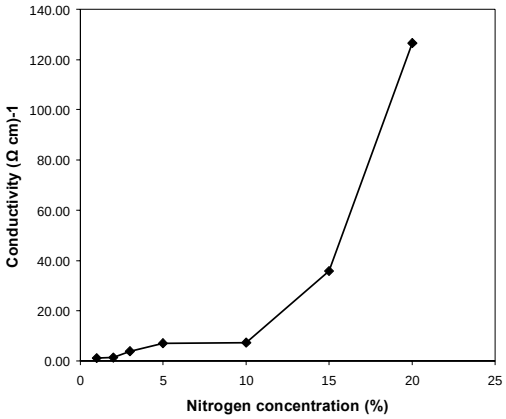

Figure 5.5: Electrical conductivity of NCD films as a function of nitrogen concentration in the plasma. The conductivity increases roughly three orders of magnitude.

Typical Raman spectrum of the conducting NCD film is shown in Figure 5.6. The Raman spectrum of the sample exhibits three features near 1140, 1332, 1480 and 1560 cm^{-1} respectively. The peak at 1332 cm^{-1} is well known as the diamond characteristic. The small feature around 1140 cm^{-1} is related to the carbon-hydrogen bonds in the grain boundaries (*134*). The broad band centered at 1480 and 1560 cm^{-1} is related to the G-band of graphite, indicating the presence of sp^2 bonded carbon within the films. However, compared these two spectra, there is no significant change between them. Since Raman spectroscopy is much more sensitive to sp^2, it is very hard to estimate the effect of nitrogen doping on the structure change of diamond film.

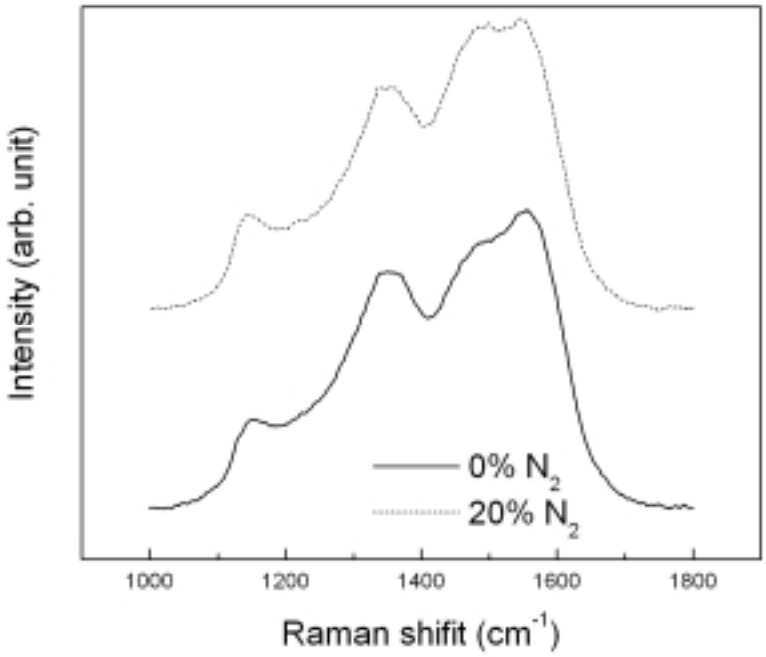

Figure 5.6: Raman spectrum of NCD films with and without nitrogen doping. Similar features have been observed.

Therefore, a technique that can distinguish between sp^2-bonded carbon (graphite) and sp^3-bonded carbon (diamond) would be very useful for the characterization of

nanocrystalline diamond films. X-ray core level reflectance and absorption spectrum is site and symmetry selective and the magnitudes and energy positions of the spectral features contain bonding information of the films. Thus, near edge x-ray absorption fine structure (NEXAFS) measurements have been carried out on conducting NCD films to determine the relative quantity of sp^2 or sp^3 bonding. From previous literatures, we have known that amorphous carbon shows the characteristic transition to sp^2 bonded σ^* orbitals at ~285 eV and bulk diamond shows a sharp peak at ~289.5 eV due to the bulk C-1s core exciton and characteristic transitions to sp^3 bonded π^* orbitals (*134*). These two features are directly related to the bonding structures of diamond and graphite and could be used to determine the sp^2 to sp^3 ratio in a film. The results of the total electron yield (TEY) NEXAFS experiments on un-doped and 20% nitrogen doped NCD are shown in Figure 5.7. Both films show nearly identical spectra compared to natural diamond (could be found in reference (*134*)), suggesting they are phase pure diamond with only a small fraction of sp^2-bonded carbon in the film. As nitrogen is added to the film, the sp^2 bonding slightly increases, as indicated by the decreasing diamond exciton peak at 289.5 eV and the increase of the π^* bonding peak at 285 eV. Therefore, the enhanced electrical conductivity could be attributed to the presence of more sp^2-bonded carbon with the addition of N_2.

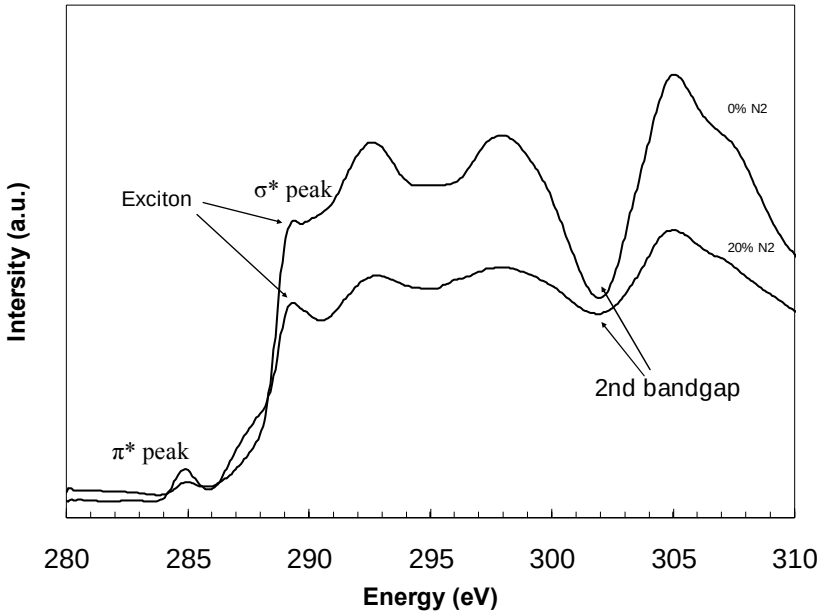

Figure 5.7: TEY NEXAFS spectra of NCD films with or without nitrogen doping

Moreover, the NEXAFS study of NCD films deposited with 10 to 40% of nitrogen was also conducted to investigate the amount of sp^2-bonded carbon in the film, shown in Figure 5.8. All the spectrum of nitrogen doped NCD are nearly identical to that of single crystal diamond, indicating that they have similar structure as diamond. As nitrogen is added to the film, the sp^2-bonding increases only slightly and the diamond exciton peak at 289.5 eV decreases. The relative amount of sp^2-bonded carbon to sp^3-bonded carbon as a function of nitrogen doping concentration is shown in Figure 5.9. The ratio increases from around 8% to more than 25% for film doped with 40% of nitrogen. This increase can be explained by the corresponding morphology change, in which wider grain boundaries compromise a larger percentage of the film as a whole. And it is consistent with the theory that nitrogen is preferentially incorporated into the grain boundaries and other reported data (*84*).

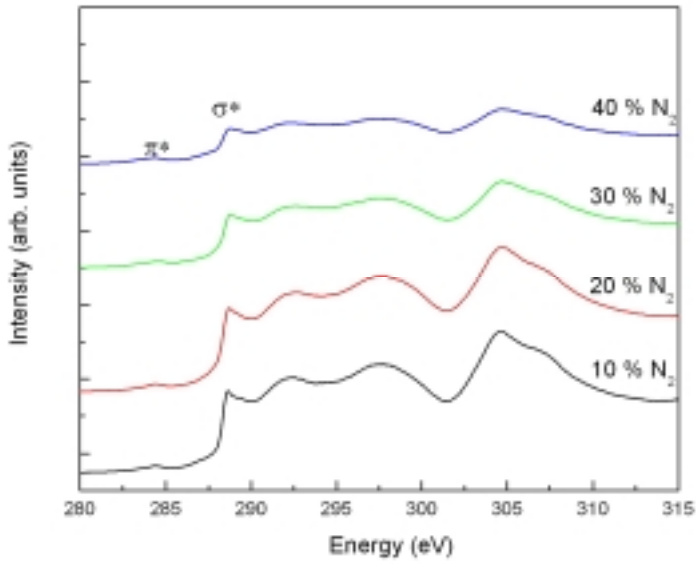

Figure 5.8: TEY NEXAFS spectra of nitrogen doped NCD thin films, showing a full scan of all the relevant features for diamond.

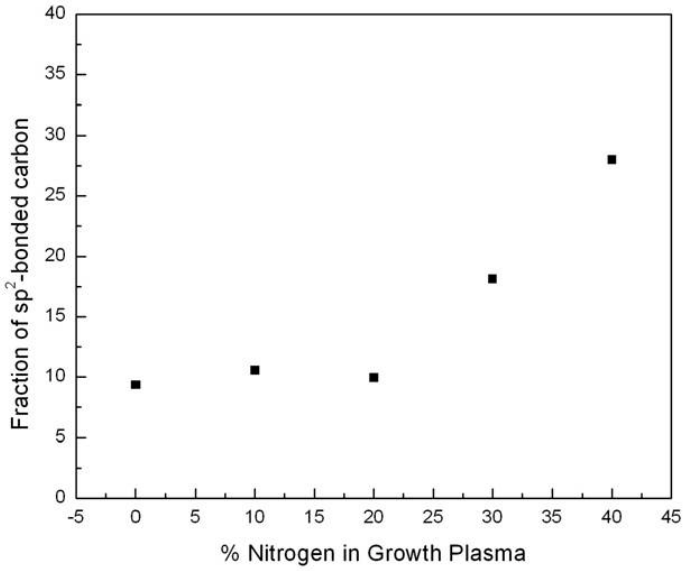

Figure 5.9: Ratio of sp^2-bonded carbon to sp^3-bonded carbon in nitrogen doped NCD.

5.3.2 Surface modification of NCD electrodes

The main method for the construction of electrochemical glucose biosensor is based on the enzyme glucose oxidase. GOX catalyzes the oxidation of glucose through a two-step process, [16] which can be expressed as follows:

$$\text{Glucose} + \text{GOX (FAD)} \rightarrow \text{Gluconolactone} + \text{GOX (FADH}_2\text{)} \quad \text{(ix)}$$

$$\text{GOX (FADH}_2\text{)} + \text{O}_2 \rightarrow \text{GOX (FAD)} + \text{H}_2\text{O}_2 \quad \text{(x)}$$

GOX (FAD) and GOX ($FADH_2$) represent the oxidized and reduced states of the flavin active site in GOX, respectively. A side product of these reactions is hydrogen peroxide (H_2O_2), whose electroactivity can be used to obtain a measurable current signal.

The NCD electrode could not be bonded with GOX glucose oxidase directly; therefore a surface modification step is required. We have selected carboxyl functional groups to functionalize the diamond surface and covalently immobilize the GOX. The hydrogen terminated NCD surface was obtained in order to attach the COOH functional groups. XPS measurements were performed on the NCD electrode before and after plasma treatment, as shown in Figure 5.10. In the C (1s) region, the untreated sample shows a small C (1s) peak at ~284.7 eV arising from oxidized form of carbon in addition to the large peak at 284.5 eV. After H-plasma treatment, the C (1s) peak is well defined at 284.5 eV.

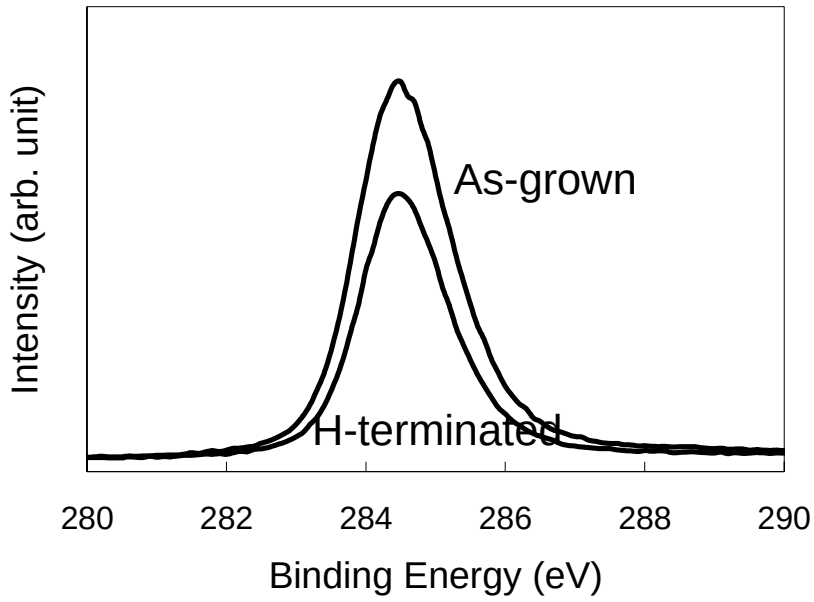

Figure 5.10: XPS scans of the C 1s spectra of nanocrystalline diamond film before and after hydrogen termination via exposure to hydrogen plasma.

Moreover, hydrogen plasma treatment can not only terminate the surface with hydrogen but also can etch the non-diamond content on the surface. The TEY NEXAFS scans have performed before and after hydrogen plasma treating. Figure 5.11 shows full scan spectrum of two films. After the hydrogen plasma treating, a significant increase of diamond exciton peak and the second band gap can be observed. A detailed scans of the π^* bonding peak and the second band gap peak has been shown in Figure 5.12a and Figure 5.12b. The height of the π^*-bonding peak decreases and the depth of the second bangap increases after treating, suggesting an increase of the ratio of the σ^*-bonding.

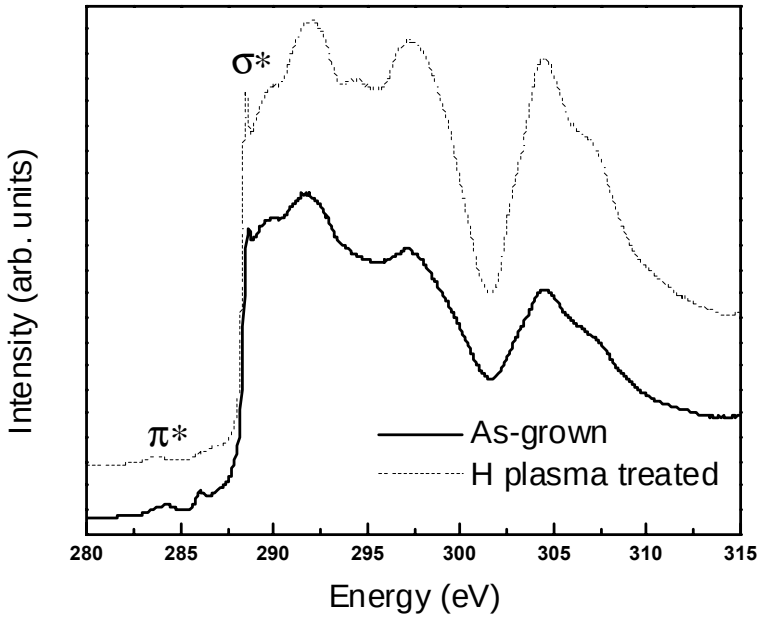

Figure 5.11: NEXAFS scans of nanocrystalline diamond film before and after hydrogen termination via exposure to hydrogen plasma.

The ratio of the sp^2-bonded carbon to sp^3-bonded carbon was calculated and shown in Figure 5.13. The ratio decreases from 7.8 % to 3.7 %, representing an etching effect of sp^2-bonded carbon during hydrogen plasma treating.

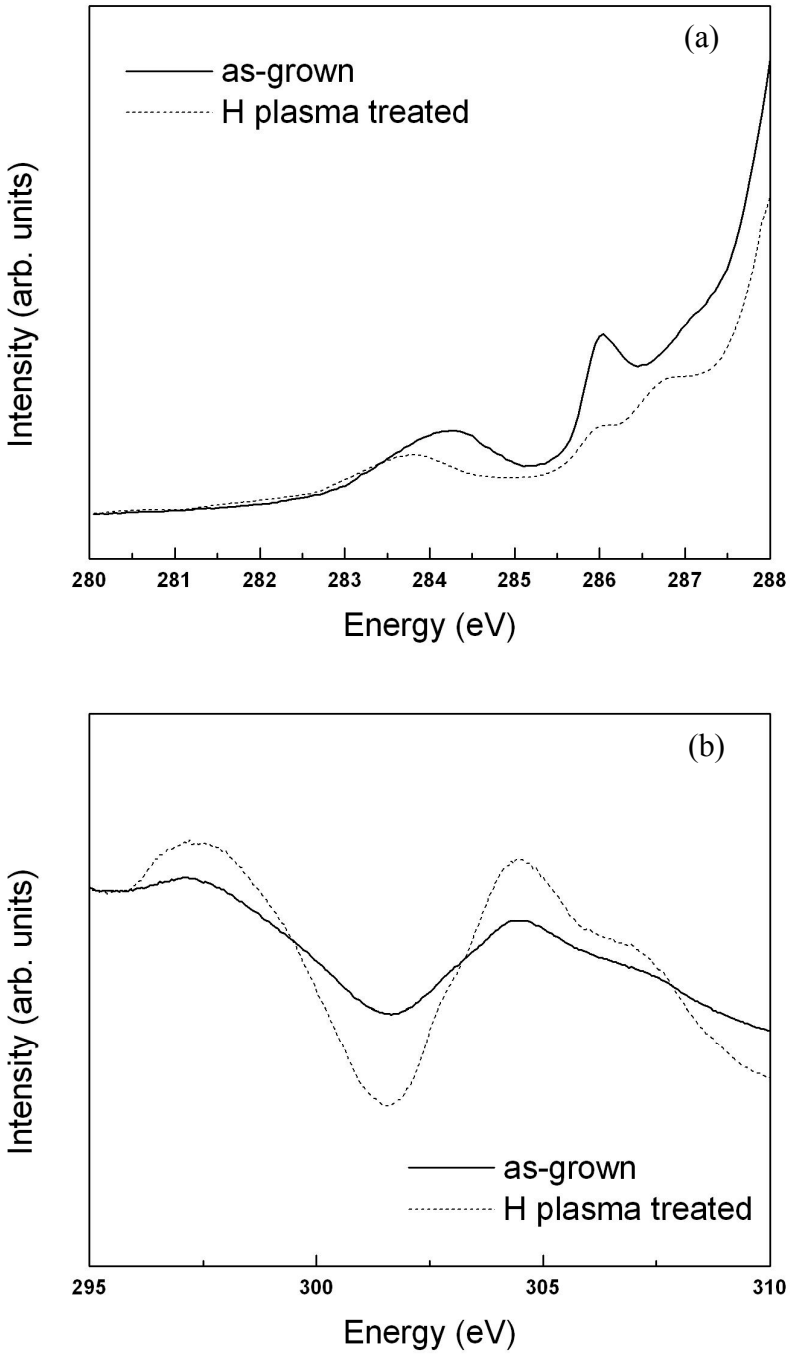

Figure 5.12: NEXAFS scans of NCD films before and after hydrogen plasma treatment. (a) π* peak at around 285 eV decreases which suggests the content of graphite was removed during treating; (b) the secondary bandgap increases after treating indicating the diamond structure was improved.

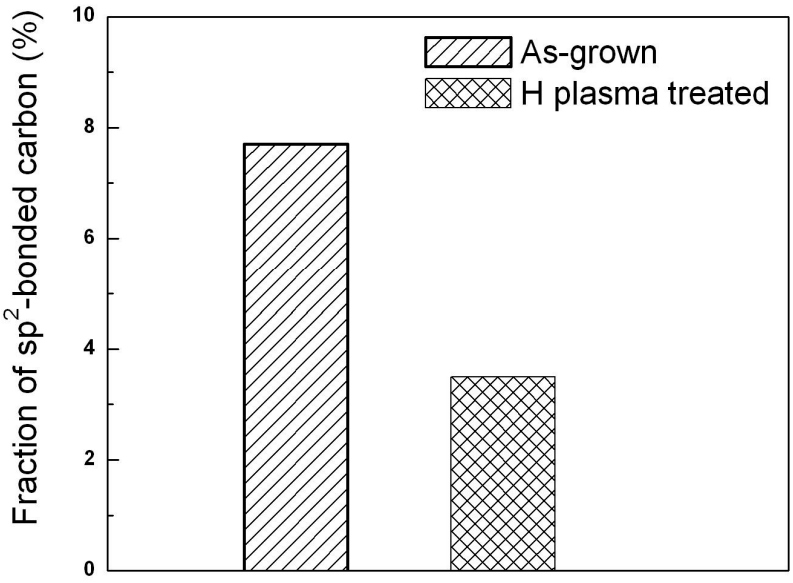

Figure 5.13: Sp^2 content of the NCD films decreases from 7.8% to 3.7% after hydrogen treating.

In order to confirm the immobilization of GOX, Fourier Transform Infrared Spectroscopy (FTIR) has been used. The amide I and II infrared bands have been widely utilized for monitoring conformational changes in proteins. As shown in Figure 5.14, two amide bands, within ranges of 1700–1600 cm^{-1} and 1600–1500 cm^{-1}, were observed. The presence of the absorption in the vicinity of 1570 cm^{-1}, which is the characteristic of GOX, suggests that the attachment of GOX onto carboxyl groups does not perturb the GOX conformations drastically. The weak peak at 1735 cm^{-1} reveals that some of the surface acetic acid is adsorbed with hydrogen bonding, which confirmed the attachment of the carboxyl group on the H-terminated NCD surface.

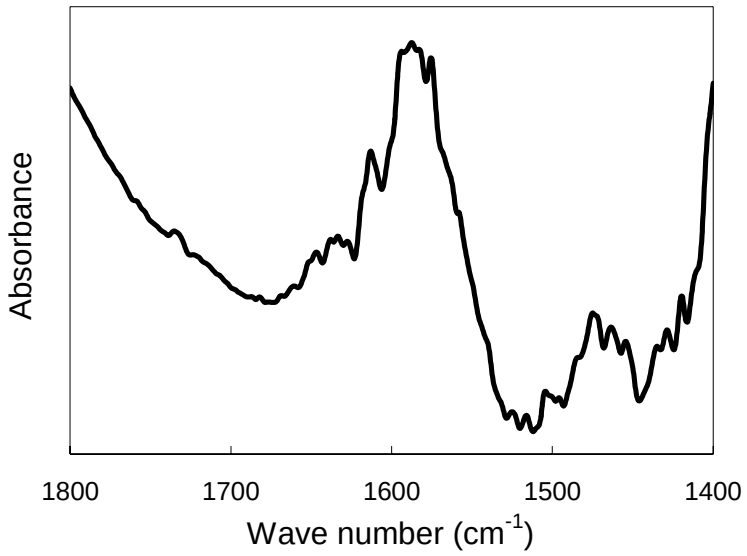

Figure 5.14: Infrared absorption spectrum of NCD film after GOX immobilization.

5.3.3 Amperometric detection of glucose

Electrochemical behavior of the enzyme modified NCD electrodes has been evaluated. Figure 5.15 shows the cyclic voltammograms and calibration curve of the modified NCD electrode with glucose concentration ranging from 0 to 15 mM. Cyclic voltammogram was first performed in the absence of glucose, which is shown as cycle 0 in Figure 5.15a. A 25 µl phosphate buffer solution containing 1 mM glucose was spiked into electrochemical cell and the response curve of the NCD electrode was recorded. A significant increase in the anodic peak current of cycle 1 can be observed. Injection has been done every 5 minutes for 15 times. The CV graphs of glucose concentration range from 0 to 7 mM have been plotted. The anodic peak current is found to be proportional to the glucose concentration. Figure 5.15b shows the calibration curve for the amperometric response with glucose ranging from 1 to 15 mM at the GOX-modified NCD electrode. The linear relationship between the glucose concentration and the response current was

found within the glucose concentration range of 1 to 13 mM. Normal concentrations of glucose in blood are less than 6.1 mM and a large excess of blood glucose (higher than 7.0 mM) is generally diagnosed as a symptom of diabetes. Therefore, the detection range of this sensor covers the normal to abnormal levels of diabetic patients. Note that all the experiments were performed in Phosphate buffer solution instead of the human serum proteins. Due to the NCD's bioinert and biocompatibility properties, it is expected that tests based on human serum protein will show similar results.

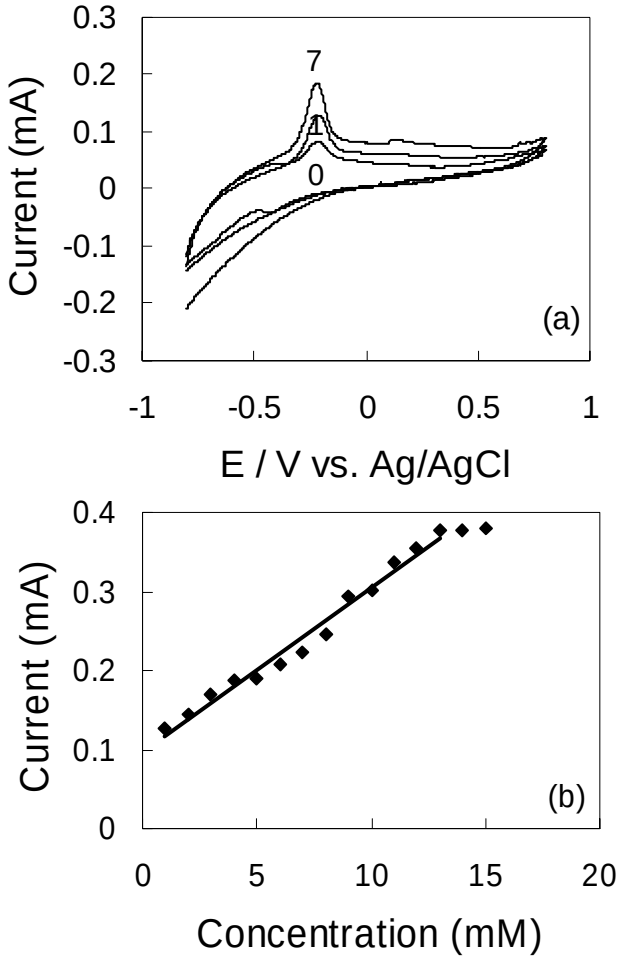

Figure 5.15: Response of the nitrogen doped NCD electrode. (a) Cyclic voltammograms. (b) Plots of anodic peak current as a function of glucose concentration over the range from 1 to 15 mM.

The temperature dependence studies were performed in phosphate buffer solution with 8 mM glucose over the temperature range from 20 to 45°C. Plots of the current respect to the temperature have been shown in Figure 5.16. The sensor shows very good temperature stability of detection with stand deviation around 2.1%, indicating the suitability of this enzyme modified NCD electrode for in vivo glucose detection under different environments.

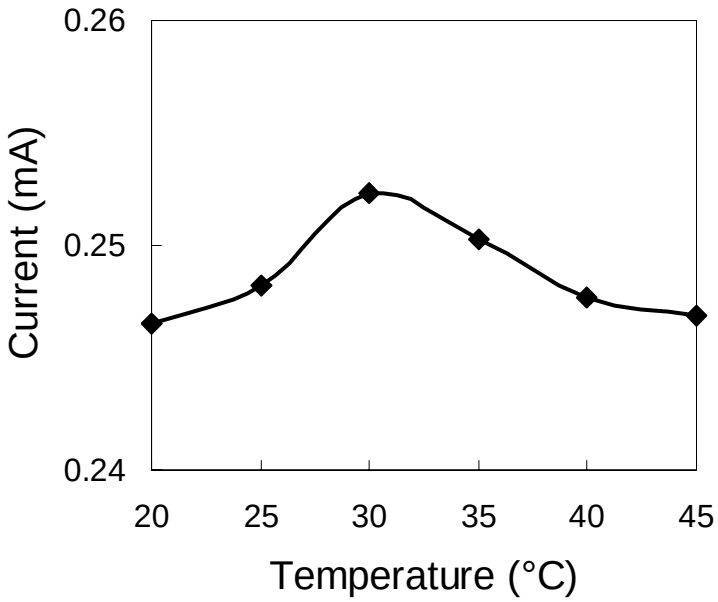

Figure 5.16: Effect of temperature (20 - 45°C) on the activity of glucose sensor. The stand deviation is about 2.1%.

The reproducibility of the electrodes was examined in 8 mM glucose solution. The relative standard deviation was 1.7% for 10 measurements. The long term stability of the NCD electrode was checked every 2 days by measuring 8 mM glucose concentration and keeping the sensor at 4 °C in 0.1 M phosphate buffer solution when not in use. The current response of the sensor to glucose remained stable during the first 10 days, and ~76% of the original response value after 3 weeks. This good reproducibility and storage

ability can be attributed to the excellent biocompatibility of NCD and the strong interaction between GOX and carboxyl group, and carboxyl group and NCD surface.

5.4 Experiments to Modify NCD Electrodes by Conducting Polymer

The electrochemical synthesis of PANI films was carried out in a compartment with a three electrode configuration using a Parstat 2263 potentionstat. The polyaniline films were deposited onto NCD films using a solution of 1 M HCl + 0.1 M aniline in D.I water. The deposition was performed by cyclic voltammetry (CV) technique at $1mVs^{-1}$ between -0.2 and 1.4 V for 5 cycles in the solution mentioned above. Electrodes were rinsed with DI water to remove any excess acid or aniline afterwards. All the experiments were performed at room temperature (20°C).

A 25 µl volume of 0.1 M Phosphate buffer solution (PBS) containing 0.2 mg (9.47 unit) glucose oxidase was coated onto the functionalized NCD electrode surface. The electrode was stored in the dark at 4ºC for use. The electrochemical responses of this modified electrode were characterized electrochemically. All experiments were carried out in 0.1 M PBS (pH 7.2) with a three-electrode cell configuration. The modified NCD electrode was used as a working electrode, the Ag/AgCl electrode as a reference electrode and a platinum electrode as a counter electrode. The geometric area of the working electrode is about 60 mm^2. The scan rate used in cyclic voltammogram experiments was 50 mV/s and the scan was performed between -0.2 to 1.4 V.

5.5 Results of PANI Modification

The surface morphology of the NCD film before and after polyaniline deposition has been observed using SEM. Figure 5.17a shows the SEM image of nanocrystalline diamond film with grain sizes ~15 to 20 nm. Atomic force microscopy (AFM) study shows a surface roughness of as low as 15 nm. For a 3 h deposition, a 0.75 μm thick film has been deposited, representing a growth rate about 0.25 μm/h. No columnar structure, which is common in conventional H_2/CH_4 diamond growth, has been observed, suggesting that NCD growth has high secondary nucleation rate resulting in fine structures. Figure 5.17b shows the presence of PANI films deposited on NCD by electrochemical method. Porous structures have been observed from the SEM micrograph.

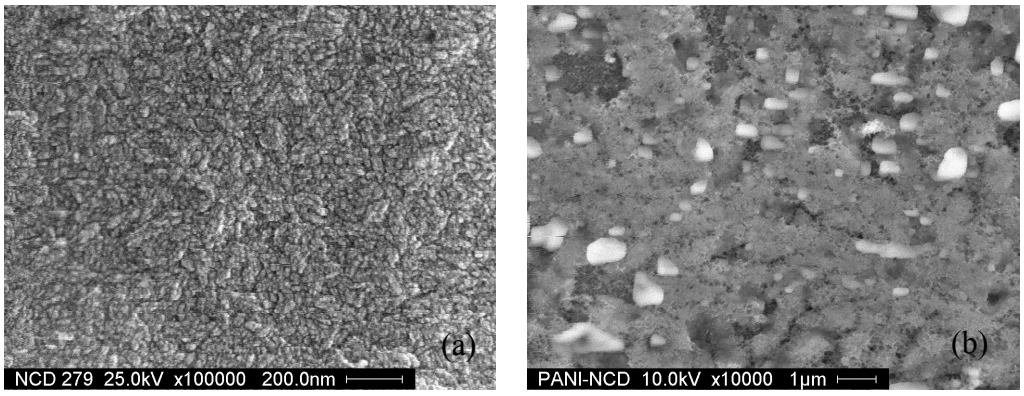

Figure 5.17: SEM micrographs of nanocrystalline diamond films (a) before and (b) after PANI deposition.

The deposition of PANI has been confirmed by Fourier transform infrared (FTIR) microscopy, shown in Figure 5.18. Peaks corresponding to the C=N and C=C stretching modes of the quinonoid (1565 cm^{-1}) and benzenoid units (1490 cm^{-1}) have been observed. These values agree well with previous studies of polyaniline (*135*).

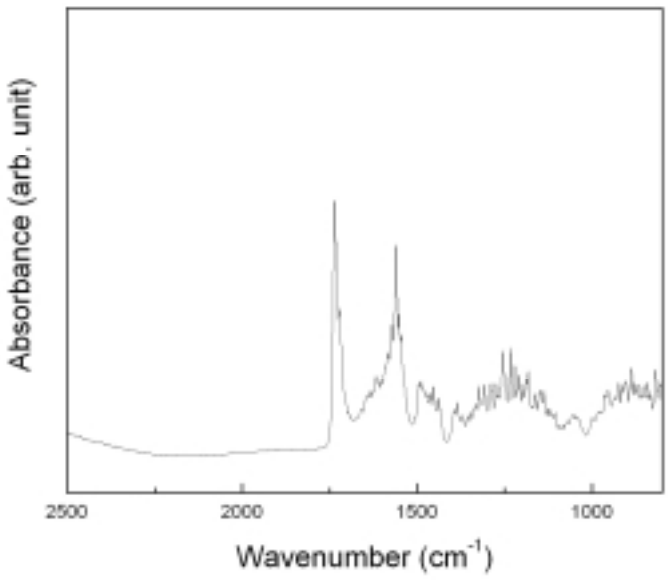

Figure 5.18: FTIR spectrum of PANI deposited diamond film.

Electrochemical behavior of the GOX/PANI/NCD electrode used for glucose sensing was characterized. A 25 µl PBS containing 1 M glucose was spiked into electrochemical cell containing 25 ml buffer and the response curve of the electrode was recorded. Figure 5.19 shows cyclic voltammograms obtained for the modified NCD electrode with and without the presence of 1 mM glucose. No peak was found in the absence of glucose whereas a significant increase in the anodic peak current was observed. It is widely known that hydrogen peroxide (H_2O_2) will be generated due to the reaction with glucose and glucose oxidase. Therefore, the anodic oxidation of H_2O_2 generates a current signal which is proportional to actual glucose concentration. With the interesting properties of NCD for electrochemical oxidation of H_2O_2, the direct detection of glucose becomes feasible via the direct anodic oxidation of H_2O_2. One of the key issues in the biosensor design is to establish fast and stable electrical communication

between the enzyme and the electrode surface. The porous feature of the PANI allows the immobilization of enzyme (GOX) and the entrapment of enzymes in conducting polymer films providing a controlled method of localizing the molecules in a defined area on the electrodes. Moreover, rapid and direct electron transfer could be achieved between the substrate and the surface (*136*). Injection of 1 mM glucose has been done in every 5 minutes for 15 times. The current value at 0.5 V as a function of glucose concentration has been plotted in Figure 5.19b. A roughly linear response to glucose concentration up to about 9 mM has been observed. The current/concentration ratio remains constant till the glucose concentration reaches 9 mM and then decreases afterwards. Normal concentrations of glucose in human blood are less than 6.1 mM and a large excess of blood glucose (higher than 7.0 mM) is generally diagnosed as a symptom of diabetes. Therefore, the approximately linear relationship between the glucose concentration and the response current is suitable for glucose sensing.

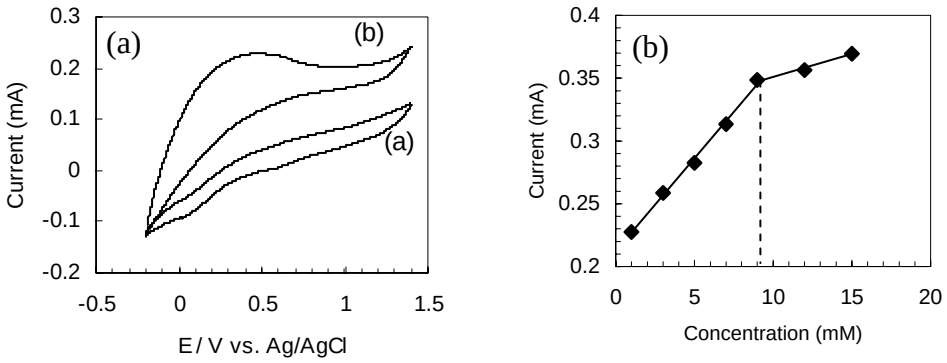

Figure 5.19: Cyclic voltammograms of GOX/PANI/NCD electrode in PBS (a) without and (b) with the presence of 1 mM glucose.

5.6 Summary

In this present study, electrochemical enzyme biosensor based on a nitrogen-doped NCD electrode has been developed and evaluated. Covalent immobilization of glucose oxidase was achieved using carboxyl functional groups, which was attached to the hydrogen-terminated NCD surface. Evaluation of glucose sensing was performed by electrochemical analyzer and the linear relationship between the response current and the glucose concentration has been found in the range of 1-13 mM. The electrodes exhibited good stability for the estimation of glucose over temperatures from 20 to 45°C.

In summary, nitrogen doped nanocrystalline diamond thin films have been deposited with $CH_4/Ar/N_2$ gas mixtures. NEXAFS studies demonstrated that nitrogen-doped NCD films were nearly phase pure diamond with a small fraction of sp^2-bonded carbon. With the addition of N_2 during deposition, the conductivity of the films increased due to the presence of more sp^2-bonded carbon in the grain boundaries. PANI modified nanocrystalline diamond electrodes have been developed and characterized for glucose detection. Evaluation of glucose sensing was performed by electrochemical analyzer and the linear relationship between the response current and the glucose concentration has been found up to 9 mM.

CHAPTER 6:

FABRICATION OF NCD WIRES

6.1 Introduction

Nanocrystalline diamond exhibits high hardness, exceptional thermal conductivity, chemical inertness, biocompatibility, and negative electron affinity (*14*). These unique properties make NCD a promising candidate for use as a protective coating with excellent tribological properties (*137*); a functional platform for biosensors (*58*); and structural material for micro-electro-mechanical systems (MEMS) (*36*). Particularly, diamond electrodes have attracted considerable interest in recent years due to their superb electrical, thermal and electrochemical properties (*50-52*). However, until now most of the diamond related work is based on a two dimensional form of NCD; in other words, a thin film that is deposited on Si substrate. The question is if we can grow diamond wire just like other semiconductor wires such as Si (*138, 139*) and ZnO (*140*) nanowires.

Diamond film has been deposited on metal wires such as Pt (*141, 142*) or W (*143*) for electrochemical, biological, and thermal applications. However, the diameter of these diamond coated wires is in the order of hundred micrometers which significantly limits the sensitivity and selectivity of these electrodes. Here we demonstrated, for the first time, a novel approach to synthesize NCD wires by depositing NCD coatings on SiNWs in typical microwave plasma enhanced chemical vapor deposition (MPECVD) growth conditions. The diameter of the wire is approximately in the range of 1-5 μm and the

length of the wire is more than 30 μm. By reducing the diameter from a couple hundred micrometers to a few micrometers, much higher surface to volume ratio can be obtained for better biological or electrochemical functionalization. Moreover, the diameter of the wire seems to be proportional to the growth time, providing a controlled method to fabricate nanocrystalline diamond wires.

6.2 Experimental

Our synthesis of SiNWs was conducted in a quartz tube furnace based on thermal evaporation of pure SiO powders under controlled temperature and pressure conditions with the presence of Au catalyst. The Si nanowire growth apparatus consisted of an evacuated quartz tube (diameter 76.2 mm, length 1219.2 mm) placed inside a tube furnace (Linderg blue, shown in Figure 6.1). Pure SiO powder (99.9%, Aldrich) was used as source and placed at the center of the quartz tube. A Si substrate coated with 6 nm thick Au was placed near the SiO powder to collect the Si nanowires. The carrier gas was argon (flow rate 100 sccm). The SiO source was heated to 1100 °C at a total pressure of 300 torr for 2 h.

In order to deposit nanocrystalline diamond on these nanowires, the sample was dipped into 25 ml methanol solution which contains 5 mg nanodiamond powder with an average particle size around 4 nm. Due to the high aspect ratio and large surface area of SiNWs small diamond particles might be left on the surface of the wire which will help the nucleation in the early stage of NCD growth. The diamond deposition was under Ar rich plasma environment with the following growth parameters: deposition time, 10-30 min; chamber pressure, 100 Torr; gas reactants, $Ar/H_2/CH_4$, 189/10/1 stand cubic

centimeters per minute (sccm); temperature, 750°C. The as-deposited products were characterized and analyzed by scanning electron miscopy (SEM) (Hitachi s4800), transmission electron microscopy (TEM) (FEI Technai F30 TEM), Raman spectroscopy (Renishaw 1000), and near edge X-ray absorption fine structure (NEXAFS) (Synchrotron Radiation center, Herman beam line). The energy disperse spectrometry (EDS) analysis was performed in the STEM mode using Tecnai Imaging & Analysis (TIA) software with the EDAX system.

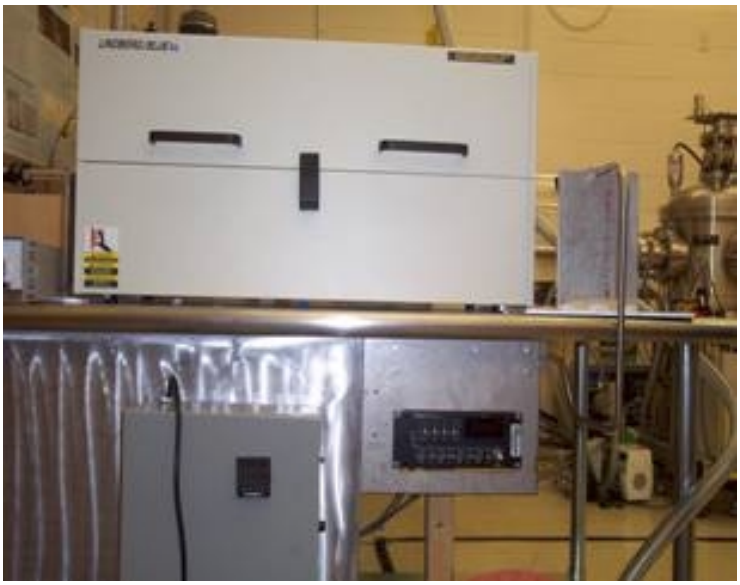

Figure 6.1: Linderg blue furnace at USF.

6.3 Results and Discussion

6.3.1 Synthesis of Si nanowires

In Figure 6.2, the SEM micrograph shows that the lengths of these SiNWs are in the range of several tens to several hundreds of micrometers and the diameters of these wires are approximately several hundreds of nanometers. It has been demonstrated that these SiNWs were composed of silicon nanoparticles as cores and amorphous silicon

oxide as shells (*138, 139*). These SiNWs are randomly oriented and stick to each other in some cases.

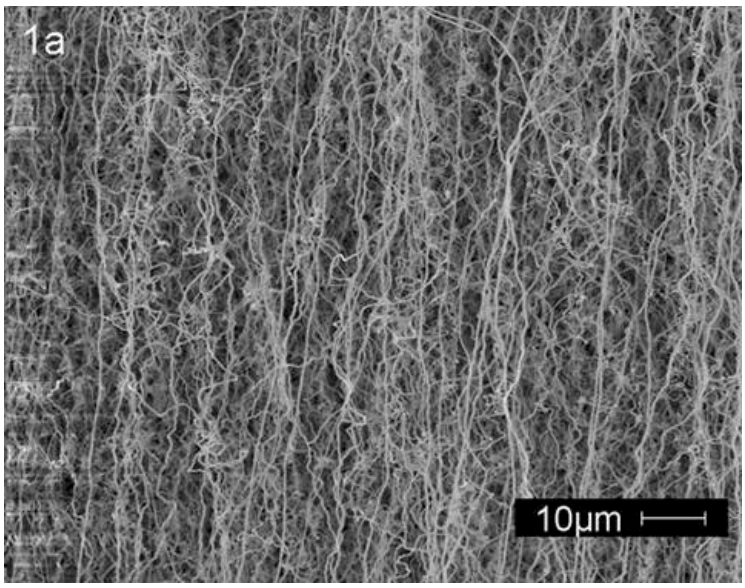

Figure 6.2: SEM micrograph of SiNWs deposited by thermal evaporation of SiO powder. The length of the SiNWs is in the order of hundred microns and the width is around 50 to 200 nm.

High resolution TEM analysis has been performed on these SiNWs, shown in Figure 6.4. These SiNWs are randomly oriented and stick to each other in some cases. The diameter of this particular SiNW is around 200 nm. A few Si nanoparticles can be observed in the Si nanowires. The EDX study shows that the out shell of the wire is composed of amorphous SiO and the inside particles consists of only Si. No gold particle can be observed on the top of these Si Nanowires, indicating that the growth mechanism of these SiNWs is more form oxide-assisted-growth instead of the vapor-liquid-solid (VLS) method. Detailed explanation can be found from reference(*139*).

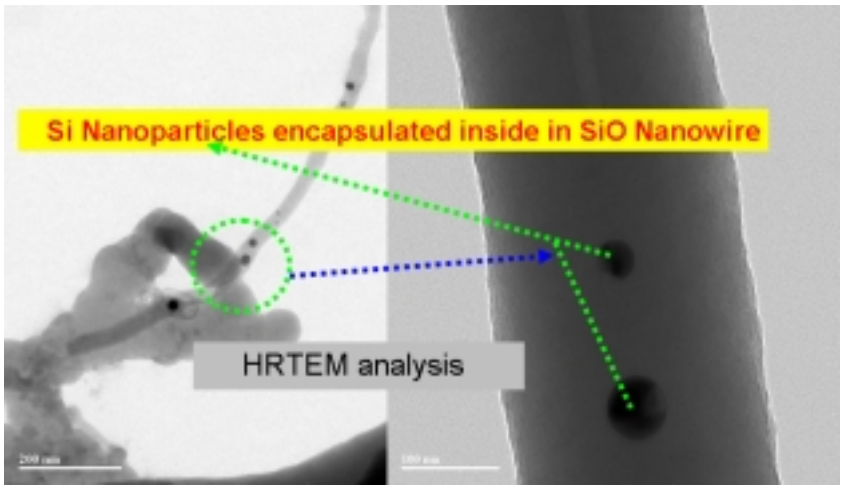

Figure 6.3: HRTEM analysis of SiNWs. Note that the Si nanoparticles are encapsulated inside the Si nanowires.

6.3.2 Deposition of diamond coating on SiNWs

Figure 6.4 shows after 10 min of diamond deposition, SiNWs are partially coated with a few nanocrystalline diamond supergrains. These supergrains, consisting of many nanometer-sized crystalline diamond grains, have also been observed in the deposition of hybrid structure of ultrananocrystalline diamond (UNCD) and carbon nanotubes (CNTs) (*144*). It is very interesting to note that diamond grew much faster on SiNWs than it did on flat Si substrate. The nanodiamond seeds left on SiNWs are believed to be responsible for such fast growth. It should be addressed that without seeding in the nanodiamond containing solution, no growth were observed. Hence, these small nanodiamond seeds play an important role in the growth of NCD wires. After 15 minutes of deposition; SiNWs are totally covered with NCD films. The diameters of these wires range between 1 and 2 μm. It was observed that the diameters of the wires increased to approximately 4-5 μm after 30 minutes of deposition. A continuous NCD coating was formed and covered all the SiNWs as well as the Si substrate after 1 h of deposition. Note that in Figure 6.5a,

NCD coating covers very nicely not only along the SiNWs but also on the tips of the wires. Two SiNWs connected to each other (shown in Figure 6.5b), suggesting the possibility to fabricate complicated NCD wire structures by patterning SiNWs. Since diamond can be doped with boron or nitrogen to make it electrically conductive, such structure may have interesting applications for MEMS fabrication. Moreover, with the outstanding mechanical properties of bulk diamond, these NCD wires are believed to have potential applications in areas that need materials with high strength and stiffness.

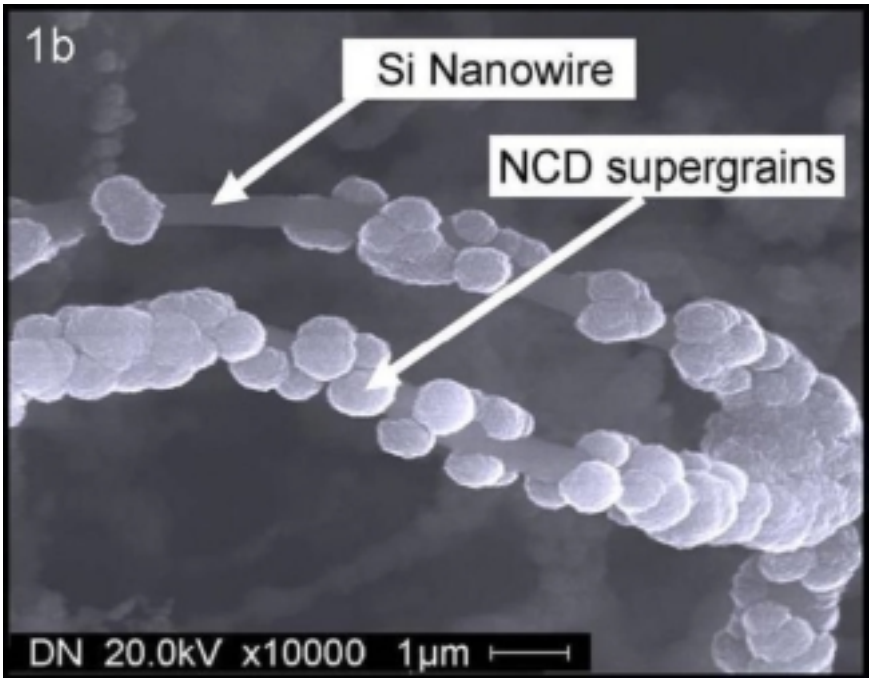

Figure 6.4: SEM image of diamond deposition for 10 min, showing some NCD super grains have been deposited.

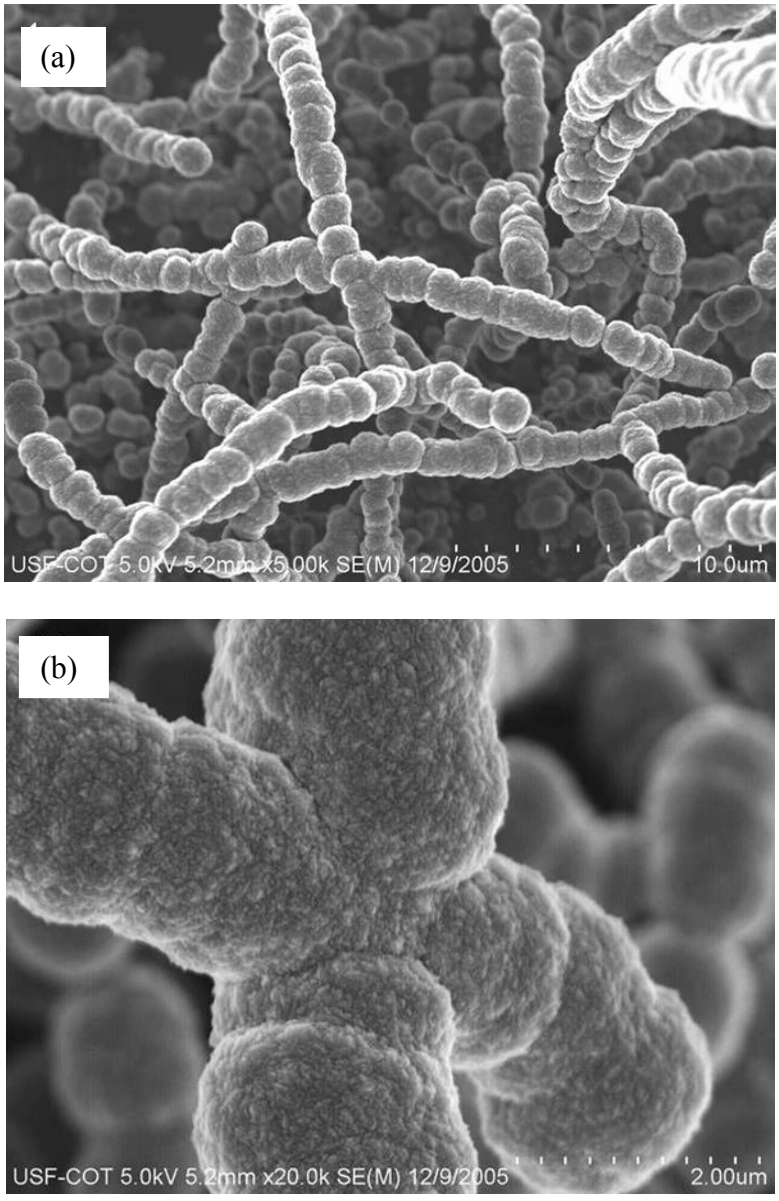

Figure 6.5: SEM micrograph of NCD wires: (a) After 15 min deposition, all SiNWs were coated with NCD; (b) High resolution SEM image, showing two NCD wires join together.

6.3.3 Characterization of NCD wires

Figure 6.6 shows the micro-Raman scattering spectra of SiNWs and NCD wires. The SiNWs spectrum, shown in the inset picture, reveals a prominent Raman feature at around 520 cm^{-1}. Note that there is no obvious Raman frequency down-shift caused by

size confinement effect which was observed frequently for SiNWs (*138*). Since the average diameter of our SiNWs is larger than 100 nm and the wires are randomly oriented, it is understandable that no significant frequency change was observed. In addition, the characteristic peak at 520 cm^{-1} becomes broadened in width compared to first-order optical phonon mode of single-crystal silicon. The full width at half maximum (FWHM) of the spectrum is about 10 wave numbers, which is similar to other published values (*145*). Raman analysis has also been performed after the SiNWs were seeded in nanodiamond solution, identical spectrum was obtained and no features other than Si peak have been observed. After 15 min deposition, the Raman spectrum shows typical NCD patterns with a diamond characteristic peak at 1334 cm^{-1} overlapping with a D-band peak at 1340 cm^{-1}, a small hump at 1140 cm^{-1} and a broad peak centered at 1560 cm^{-1}. The 1140 hump is recently proposed to be attributed to great amount of hydrogen presented in NCD grain boundaries (*146*). The broad peak at 1560 cm^{-1} is the G-mode Raman peak, which is well known for disordered carbon films and arises from the in-plane stretching modes of sp^2 bonded carbon at grain boundaries of NCD (*147*).

Figure 6.7 shows the electron energy loss spectroscopy (EELS) analysis of the NCD wires. The EELS is sensitive to the crystal structure. For trigonal sp^2 -bonded carbon, the spectrum can be separated into two broad features, corresponding to the π^* states between 282 and 288 eV and the σ^* states between 290 and 320 eV, while for tetrahedral sp^3 -bonded carbon only the σ^* peak is observed between 289 and 320 eV (*148*). For NCD wires, only one peak at 291 eV is observed, representing typical diamond structure. NEXAFS spectroscopy is also a useful tool to unambiguously distinguish the sp^2 bonds from the sp^3 bonds in carbon materials (*149*).

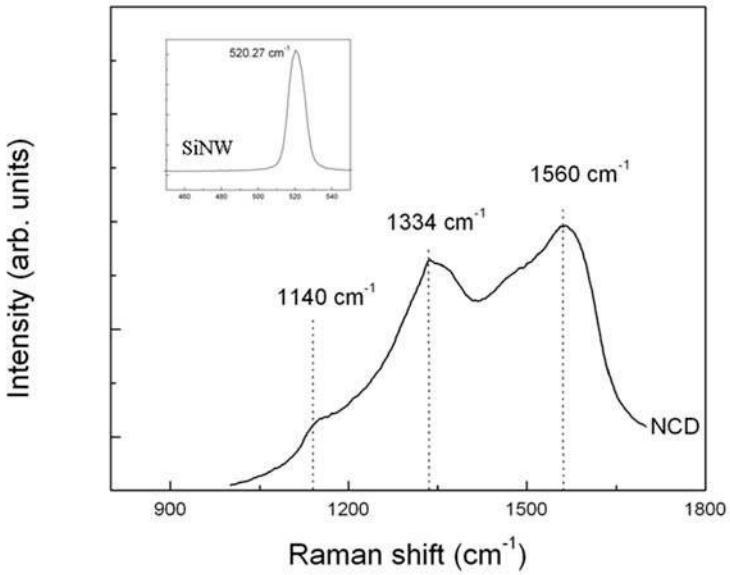

Figure 6.6: Raman spectra of Si Nanowire and NCD wires. The inset picture shows the Si peak of SiNW with FWHM value about 10 wave numbers.

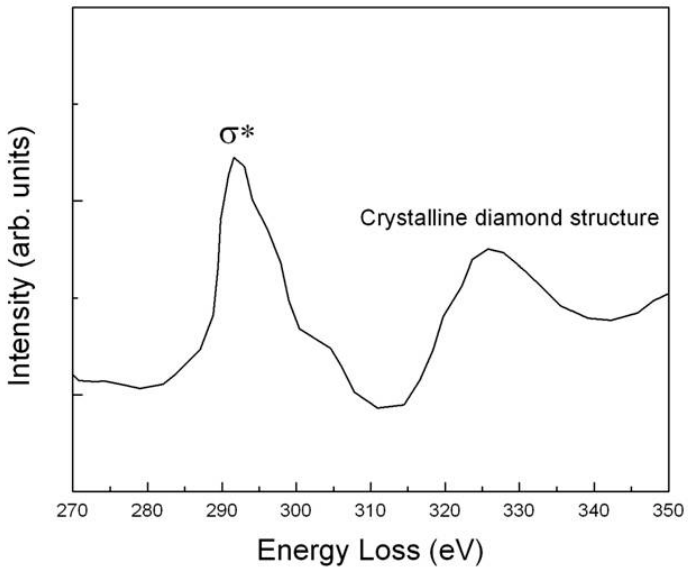

Figure 6.7: EELS analysis of NCD wires.

Figure 6.8 shows the C (1s) photoabsorption data obtained from NCD wires. The spectrum looks very similar to high quality single-crystal diamond (*84*). It is well known

that amorphous carbon shows the characteristic transition to sp^2 bonded π^* orbitals at ~285 eV and bulk diamond shows a sharp peak at ~289.5 eV due to the bulk C-1s core exciton and characteristic transitions to sp^3 bonded σ^*orbitals. These two features are directly related to the bonding structures of diamond and graphite, and could be used to determine the sp^2 to sp^3 ratio in a film. In Figure 6.8 we can clearly see that all the qualitative features of sp^3 bonding are presented in our sample. A distinct second band gap dip at 302.5 eV is also observed, which is not presented in sp^2 bonded carbon. A very small peak at 285 eV reveals that these wires are phase pure diamond with very a small amount of sp^2 bonded carbon in the film. The fraction of sp^2 bonded carbon to sp^3 bonded carbon in NCD is around 5 ~ 10 % according to a previous report (*84*).

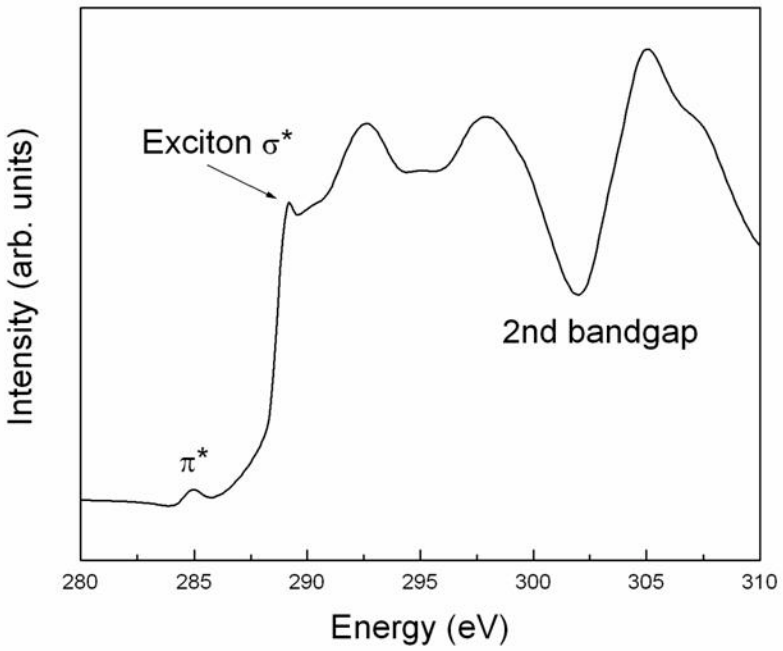

Figure 6.8: NEXAFS analysis of NCD wires.

In order to investigate the structure of these NCD wires, one small piece of wire was cut from the substrate by focus ion beam (FIB) and then was transferred to copper

grid for TEM analysis. Figure 6.9 shows a SEM image of one single diamond piece of NCD wires cut by FIB.

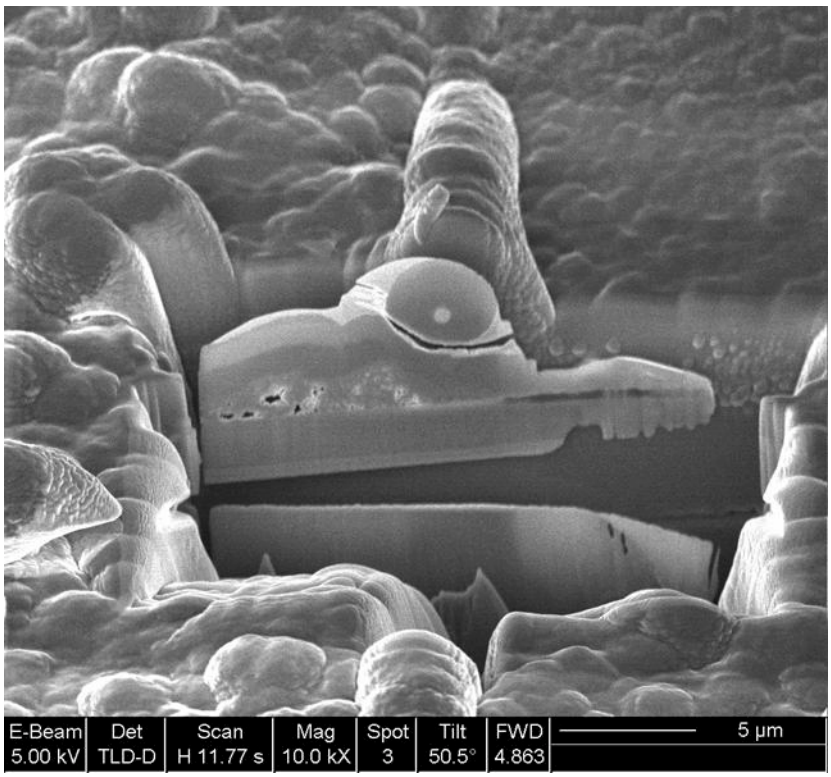

Figure 6.9: SEM micrograph of one single piece of NCD wire cut by FIB.

Figure 6.10 shows a cross section TEM image of one single diamond wire. The diameter of this wire is about 4 µm (30 min deposition). The NCD wire contains two regions, the core and the shell. Note that in the core region there are three SiNWs encapsulated in one diamond shell. As mentioned before, some SiNWs might stick together after the growth and they were never separated afterwards. During CVD process, diamond supergrains grew outside of the wires and then quickly connected to each other.

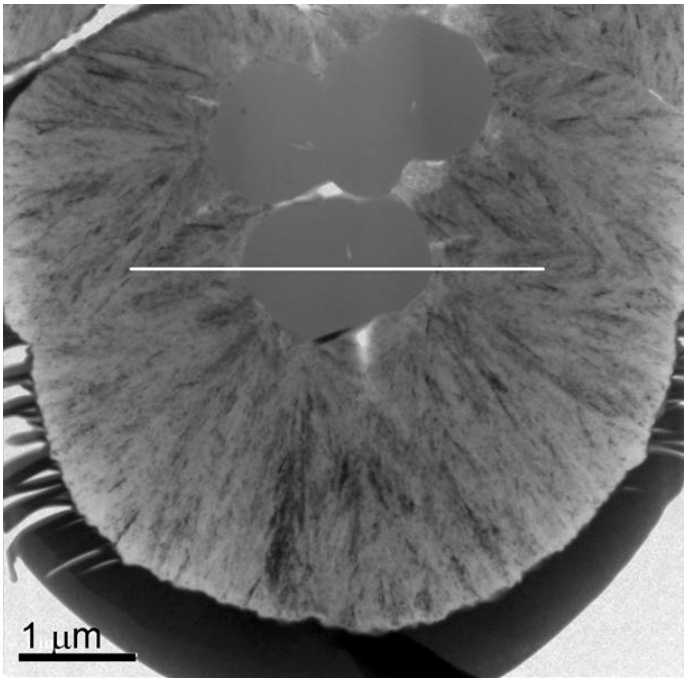

Figure 6.10: TEM cross section image of the as-deposited NCD wire.

The quantification analysis in the SiNW core region indicates the atomic percentage of Si is 40% and the atomic percentage of O is 60%, suggesting that the SiNWs are composed of amorphous silicon oxide. EDS study has been done on three different locations of the wire: core, interface and shell, shown in Figure 6.11a. In the core region, silicon and O peaks were observed at 1.74 and 0.52 keV, respectively. In the shell region, a dominant C peak at 0.28 keV suggested that the outside shell only consist of carbon. At the interface, all three peaks, C, O, and Si are visible. In the core region, only Si and O peaks are presented. Figure 6.11b shows the 1 line profile Si-O-C map along the cross section of the wire. Similar to EDS results, the NCD wire core contains Si and O while the outside shell contains only carbon.

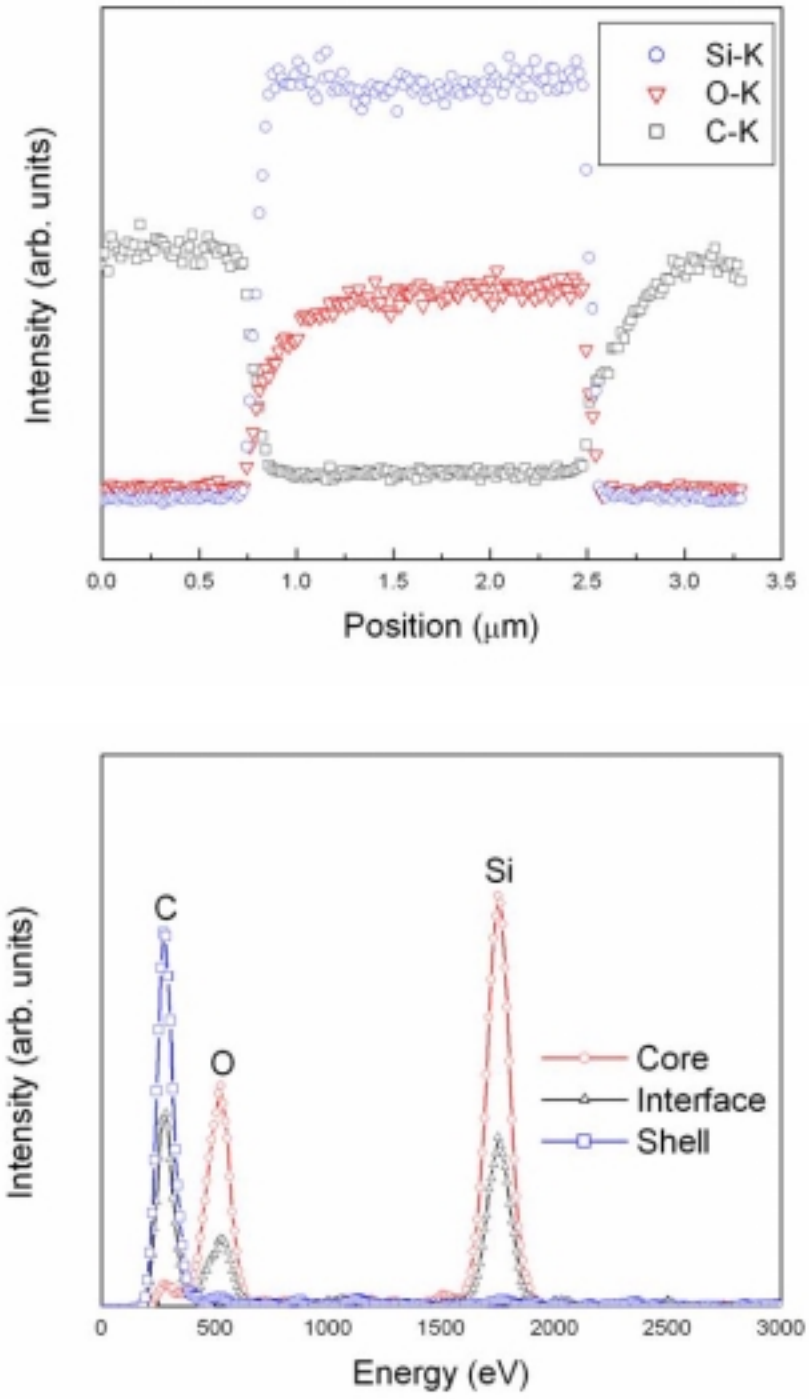

Figure 6.11: Cross section analysis of NCD wire. (a) One line profile Si-O-C mapping along the line indicated in Fig. 6.10. (b) EDS analysis performed at three positions: SiNW core, interface and diamond shell.

The high resolution tranasmission electron microscopy (HRTEM) image shows the interface between the diamond and the Si nanowire (Figure 6.12a). The diamond grains seen here are about 5-8 nm in diameter and the *d*-spacing for the (111) plane in diamond is 0.206 nm. Note that the no clear crystallinity of Si can be observed, suggesting the amorphous nature of the SiNWs. In the selected area electron diffraction (SAED) pattern taken at the diamond shell region (Figure 6.12b), sharp (111), (220), and (311) Bragg reflections are visible, indicating good crystallinity of NCD.

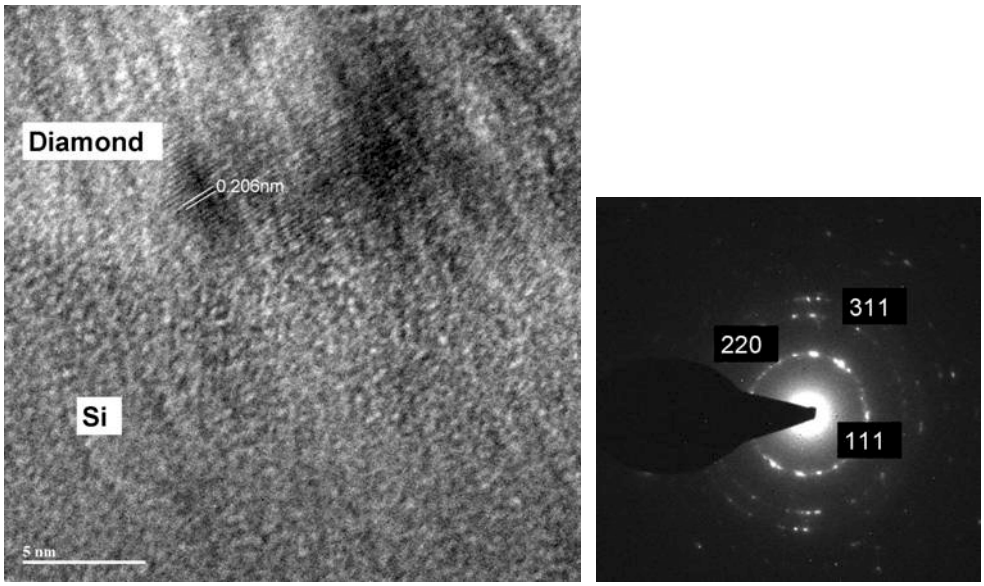

Figure 6.12: HRTEM analysis of NCD wire. (a) HRTEM image of diamond-SiNW interface, d spacing of (111) diamond plane is 0.206 nm. (b) SAED pattern of diamond shell shows good crystallinity.

6.4 Summary

To our knowledge, this is the first time to report synthesis of nanocrystalline diamond wires with diameter in the order of several micrometers. Our studies demonstrated that by seeding the SiNWs in solutions containing nanodiamond powers, NCD wires can be fabricated in typical CVD growth conditions within a very short time.

Raman, EELS, NEXAFS, and TEM analysis revealed that NCD were deposited on SiNWs to form NCD wires. This new type of diamond structure will find numerous applications by taking advantage of NCD's extreme properties. NCD wire may enable the production of molecular sieves, high surface area electrodes and other applications where diamond films are not applicable. Remarkable electron and high current density has been achieved using thin film NCD (*150*) while NCD wires may further improve the field emission properties with their unique geometry. Conducting wires can also be fabricated by nitrogen incorporation during deposition to be used as electrodes in chemically aggressive environments.

CHAPTER 7:

SUMMARY AND FUTURE WORK

Micro and Nanocrystalline diamond thin films have been deposited by microwave plasma enhanced chemical vapor deposition. The primary goal of this research was to develop certain applications based on this outstanding material, diamond, taking advantage of the unique physical, electrical, chemical as well as mechanical properties. As a consequence, a parameter study was done to study the synthesis of CVD diamond films. Special attention was paid to investigate the deposition of diamond films from micro- to nanocrystallinity. The change of the surface morphology as well as the physical properties has been extensively characterized by SEM, TEM, Raman, NEXAFS, and Nanoindentation.

Based on the earlier work done on the development of diamond coated cutting tools, a new surfaced pretreatment method including deposition of interlayer and surface roughening was proposed and studied. Instead of removing Co binder phase by acid etching, this new method introduced a diffusion barrier to prevent Co leaching, a proper surface roughness and an intermediate carbide forming layer to give the diamond coating a strong adhesion property. Moreover, unlike the existing acid etching way, this new method does not reduce the substrate fracture toughness at all. However, due to the limitation of the time and lack of facilities, the author was not able to test the machining performance of these diamond-coated inserts and tools. Further testing can be done on

these tools to investigate the adhesion and wear resistance when machining against non ferrous materials without and materials removal fluid. A theoretical study can also be conducted to simulate the indentation testing by finite element analysis (FEA). By indenting thick diamond films, a large enough region of delamination can be initiated and a simulate model will be established to apply the Drory-Hutchinson model to estimate interfacial strength. Therefore, by changing the properties and the dimensions of the interlayer and the diamond coating, it is much easier to optimize the experimental conditions and design guidelines to achieve a maximum interfacial strength.

With the successful synthesis of nanocrystalline diamond films, where the grain size is around 2-5 nm in size with little or no graphitic impurities at the grain boundaries; we have found that these films have great potential for use in electronics, MEMS, and biochemical sensors, since they combine many of the superb properties of diamond with a smoothness on the nm scale. The ability to functionalize diamond films with functional groups and the superb electrochemistry nature of diamond makes NCD a candidate for future biosensors and bioimplantable devices. In this research, conducting NCD films were functionalized by carboxyl functional group and conducting polymer to covalent immobilize of redox active enzymes (e.g. glucose oxidase) onto UNCD surface for biosensing. The surface morphology and chemistry of chemically modified UNCD films in conjunction with charge transfer kinetics at the modified electrode/electrolyte interface play critical roles for the attachment of biomolecules. We have demonstrated that glucose detection based on nitrogen doped electrodes could be achieved with excellent sensitivity and stability. However, the study of NCD based biosensor is still very preliminary. The lack of chemical and biological background makes this research very difficult to be

continued. Further investigation need to be done not only by material scientist, but also by biologist and chemist.

During my last year of research, an exciting result has been obtained by a simple idea. Since diamond can be coated on W wires to form electrodes with diameter around several hundred microns; we should also be able to deposit diamond on those small wires such as SiNWs, ZnO wires or carbon nanotubes. Among them, we have found that diamond could be successfully coated on SiNWs to form NCD wires. Extensive characterization has been done on this new type of wire such as SEM, TEM, and NEXAFS. The mechanical properties of this wire are now under investigation by nanoindentation. The applications of the NCD wire, including the enhanced electrochemical properties due to the larger surface to volume ratio and the self assemble field emission emitters, are now being fabricated.

REFERENCES

1. R. F. Davis, *Diamond Films and Coatings* (1993).

2. J. C. Angus, H. A. Will, and W. S. Stanko, *J. Appl. Phys.* 39, 2916 (1968).

3. B. V. Derryagin, V. A. Ryabov, D. V. Fedoseev, B. V. Spitsyn, V. M. Lukyanovich, and K. S. Uspensakya, *Second All Union Symposium Process for Nucleation and Growth of Crystas and Films of Semiconducting Compounds* (1969).

4. S. Matosumoto, Y. Sato, M. Kamo, and N. Setaka, *Journal of Materials Science* 17, 3106 (1982).

5. W. G. Eversole, *U.S. Patents No. 3,030,187 and 3,030,188* (1962).

6. S. Jin, and T. D. Moustakas, *Apply. Phys. Lett.* 63, 2354 (1993).

7. R. Samlenski, C. Huang, R. Breen, C. Wild, R. Locher, and P. Koidl, *Appl. Phys. Lett.* 67, 2798 (1995).

8. R. B. Heinmann, S. E. Evsyukov, and Y. Koga *Carbon* 35, 1654 (1997).

9. M. Inogaki, *New carbons* (2000).

10. V. L. Kuznetsov, A. L. Chuvilin, and Y. V. Butenko, *Chem. Phys. Lett.* 209, 72 (1994).

11. B. Banhart, and P. M. Ajayan, *Nature* 382, 433 (1996).

12. J. A. Viecelli, S. Bastea, J. N. Glosli, and F. H. Ree, *J. Chem. Phys.* 115, 2730 (2001).

13. I. Ahmed, *Master Thesis, University of South Alabama* (1997).

14. D. M. Gruen, *Annu. Rev. Mater. Sci.* 29, 211 (1999).

15. S. J. Harris, and D. G. Goodwin, *J. Phys. Chem* 97, 23 (1993).

16. O. Matsumoto, T. Katagirl, *Thin Solid Films* 146, 283 (1987).

17. D. M. Gruen, S. Liu, A. R. Krauss, J. Luo, and X. Pan, *Appl. Phys. Lett.* 64, 1502 (1994).

18. P. C. Redfern, D. A. Horner, L. A. Curtiss, and D. M. Gruen, *J. Phys. Chem* 100, 11654 (1996).

19. D. Zhou, D. M. Gruen, L. C. Qin, T. G. McCauley, and A. R. Karuss, *J. Appl. Phys.* 84, 1981 (1998).

20. M. Sternberg, P. Zapol, and L. A. Curtiss, *Phys. Rev. B* 68, 205330 (2003).

21. R. Haubner, A. Lindlbauer, B. Lux, *Diam. Relat. Mater.* 2, 1505 (1993).

22. H. Baker, *ASM Handbook, Ohio, USA* 3 (1997).

23. K. Shibuki, M. Yagi, K. Saijo, S. Takatsu, *Surf. Coat. Technol.* 36, 295 (1988).

24. F. M. Pan, J. L. Chen, T. Chou, T. S. Lin, and L. Chang, *J. Vac. Sci. Technol. A* 12, 1519 (1994).

25. X. Chen, J. Narayan, *J. Appl. Phys.* 74, 4168 (1993).

26. J. Oakes, X. X. Pan, R. Haubner, B. Lux, *Surf. Coat. Technol.* 47, 600 (1991).

27. M. G. Peters, R. H. Cummings, *European Patent 0519587* A1 (1992).

28. F. Deuerler, H. Berg, R. Tabersky, A. Freundlieb, M. Pies, V. Buck, *Diam. Relat. Mater.* 5, 1478 (1996).

29. C. R. Lin, C. T. Kuo, R. M. Chang, *Thin Solid Films* 308-309, 273 (1997).

30. J. K. Wright, R. L. Williamson, and K. J. Maggs, *Mater. Sci. Eng. A* 187, 87 (1994).

31. M. Neslader, J. Spinnewyn, C. Asinari, R. Lebout, R. Lorent, *Diam. Relat. Mater.* 3, 98 (1993).

32. S. L. D. Jian X.G., Chen M., Sun F.H.,, *Diam. Relat. Mater.* 15, 313 (2006).

33. A. P. Lee, A. P. Pisano, and M. G. Lim, *Mater. Res. Soc. Sym. Proc.* 276, 67 (1992).

34. P. Sniegowski, *Tribology Issues and Opportunities in MEMS, edited by B. Bushan*, 325 (1998).

35. L. Tong, M. Mehregany, and L. G.Matus, *Appl. Phys. Lett.* 60, 2992 (1992).

36. A. R. Krauss, O. Auciello, D. M. Gruen, A. Jayatissa, A. Sumant, J. Tucek, D. C. Mancini, N. Moldovan, A. Erdemir, D. Ersoy, M. N. Gardos, H. G. Busmann, E. M. Meyer, M. Q. Ding, *Diam. Relat. Mater.* 10, 1952 (2001).

37. T. Uemura, S. Fujii, H. Kitabayashi, K. Itakura, A. Hachigo, and H. Nakahaata, *J. Appl. Phys.* 41, 3476 (2002).

38. O. Elmazria, M. Hakiki, V. Mortet, M. B. Assouar, M. Nesladek, and M. Vanecek, *Ferroeletr. Freq. Control* 51, 1704 (2004).

39. O. Elmazria, F. Benedic, M. Hakiki, H. Moubchir, M. B. Assouar, M. Nesladek, and F. Silva, *Diam. Relat. Mater.* in press (2005).

40. Y. Gurbuz, O. Esame, I. Tekin, W.P. Kang , and J. L. Davison, *Solid State Electronics* 49, 1055 (2005).

41. J. E. Gerbi, O. Auciello, J. Birrell, D. M. Gruen, B. W. Alphenaar, and J. A. Carlisle, *J. Appl. Phys.* 83, 2001 (2003).

42. A. Aleksov, M. Kubovic, M. Kasu, P. Schmid, D. Grobe, S. Ertl, M. Schreck, B. Strizker, and E. Kohn, *Diam. Relat. Mater.* 13, 233 (2004).

43. J. F. Prins, *Appl. Phys. Lett.* 41, 950 (1982).

44. A. Aleksov, A. Denisenko, and E. Kohn, *Solid State Electronics* 44, 369 (2000).

45. T. Zimmermann, M. Kubovic, A. Denisenko, K. Janischowsky, *Diam. Relat. Mater.* 14, 416 (2005).

46. J. Kusterer, F.J. Hernandez, S. Haroon, P. Schmid, A. Munding, R. Muller, and E. Kohn, *Diam. Relat. Mater.* in press (2006).

47. M. Iwaki, S. Sato, K. Takahashi *Nucl. Instrum. Methods Phys. Res.* 209-210, 1129 (1983).

48. Y. V. Pleskov, A. Y. Sakharova, M. D. Krotova, L. L. Bouilov, and B. V. Spitsyn, *J. Electroanal. Chem.* 228, 19 (1987).

49. G. M. Swain, and R. Ramesham, *Anal. Chem.* 65, 345 (1993).

50. G. M. Swain, A. B. Anderson, and J. C. Augus *MRS Bull* 23, 56 (1998).

51. H. B. Martin, A. Argoitia,, U. Landau,, A. B. Anderson, and J. C. Angus, *J. Electroanal. Chem* 143, L133 (1996).

52. H. B. Martin, J. C. Angus,, and U. Landau, *J. Electrochem. Soc.* 146, 2959 (1999).

53. G. M. Swain, *in Thin-Film Diamond II, Semiconductors and Semimetals* 77, 97 (2004).

54. C. Levy-Clement, F. Zenia, N. A. Ndao, and A. Deneuville, *New Diamond Frontier Carbon Tech.* 9, 189 (1999).

55. S. C. Eaton, A. B. Anderson,, J. C. Angus, Y. E. Evstefeeva, and Y. V. Pleskov, *Electrochem Solid-State Lett.* 5, G65 (2002).

56. B. Fausett, M. C. Granger, M. L. Hupert, J. Wang, G. M. Swain, and D. M. Gruen, *Electronanlysis* 12, 7 (1999).

57. Q. Chen, D. M. Gruen, A. R. Krauss, T. D. Corrigan, M. Witek, and G. M. Swain, *J. Electrochem. Soc.* 148, E44 (2001).

58. W. Yang, O. Auciello, J. Butler, W. Cai, J. A. Carlise, J. E. Gerbi, D. M. Gruen, T. Knickerbocker, T. L. Lasseter, J. N. Russell, L. M. Smith, and J. Hamers, *Nature Mater.* 1, 253 (2002).

59. J. Wang, J. A. Carlise, *Diam. Relat. Mater.* in press (2005).

60. A. Hartl, E. Schmich, J. A. Garrido, J. Hernando, S. C. R. Catharino, S. Walter, P. Feulner, A. Kromka, D. Steinmuller, and M. Stutzman, *Nature Mater.* 12, 1 (2004).

61. W. Yang, R. J. Hamers, *Appl. Phys. Lett.* 85, 3626 (2004).

62. M. Lu, T. Knickerbocker, W. Cai, W. Yang, R. J. Hamers, and L. M. Smith, *Biopolymers* 73, 606 (2003).

63. Z. Remes, A. Choukourov, J. Stuchlik, J. Potmesil, M. Vanecek, *Diam. Relat. Mater.* in press (2005).

64. L. C. L. Huang, and H. C. Chang, *Langumir* 20, 5879 (2004).

65. C. A. Spindt, *J. Appl. Phys.* 39, 3504 (1968).

66. C. A. Spindt, C. E. Holland, A. Rosengreen, and I. Brodie, *IEEE Trans. on Electron Devices* 38, 2355 (1991).

67. T. Sakai, T. Ono, M. Nakamoto, and N. Sakuma, *J. Vac. Sci. Technol. B* 16, 770 (1998).

68. J. Liu, V. V. Zhirnov, A. F. Myers, *J. Vac. Sci. Technol. B* 13, 422 (1994).

69. J. Liu, V. V. Zhirnov, and G. J. Wojak, *Appl. Phys. Lett.* 22, 2842 (1994).

70. F. Y. Chuang, C. Y. Sun, H. F. Cheng, C. M. Huang , and I. N. Lin, *Appl. Phys. Lett.* 68, 1666 (1996).

71. I. L. Krainsky, V. M. Asnin, G. T. Mearini, and J. A. Dayton, *Phys. Rev. B* 53, 7650 (1996).

72. C. Wang, A. Garcia, D. C. Ingram, M. Lake, and M. E. Kordesch, *Electron Lett.* 27, 1459 (1991).

73. W. Zhu, G. P. Kochanski, S. Jin, and L. Seibles, *J. Appl. Phys.* 78, 2707 (1995).

74. M. W. Geis, N. N. Efremow, K. E. Krohn, J. C. Twichell, T. M. Lyszczara, R. Kalish, J. A. Greer, and M. D. Tabat, *Nature (London)* 393, 431 (1998).

75. K. Okano, A. Hiraki, T. Yamada, S. Koizumi, and J. Itoh, *Ultramicroscopy* 73, 43 (1998).

76. D. Zhou, A. R. Krauss, T. D. Corrigan, T. G .McCauley, R. P. H. Chang, and D. M. Gruen, *J. Electrochem. Soc.* 144, l224 (1997).

77. Krauss A.R., et al., *J. Appl. Phys.* 89, 2958 (2001).

78. K. Subramanian, W. P. Kang , J. L. Davidson, R. S. Takalkar, B. K. Choi, M. Howell, and D. V. Kerns, *Diam. Relat. Mater.* in press (2006).

79. K. Subramanian, W. P. Kang, J. L. Davidson, and W. H. Hofmeister, *Diam. Relat. Mater.* 14, 404 (2005).

80. M. Hajra, C. E. Hunt, M. Ding, O. Auciello, J. Carlise, and D. M. Gruen, *J. Appl. Phys.* 94, 4079 (2003).

81. Drift A., *philips Res. Rep.* 22, 267 (1967).

82. A. Drift, *Philips Res. Rep.* 22, 267 (1967).

83. A. Chaiken, L. J. Terminello, J. Wong, G. L. Doll, and C. A. Taylor, *Appl. Phys. Lett.* 63, 2112 (1993).

84. J. Birrell, O. Auciello, J. M. Gibson, D. M. Gruen, and J. A. Carlisle, *J. Appl. Phys.* 93, 5606 (2003).

85. D. M. Gruenm, A. R. Krauss, C. D. Zuiker, R. Csencsits, L. J. Terminello, J. A. Carlise, I. Jimenez, D. G. J. Sutherland, D. K. Shuh, W. Tong, and F. J. Himpsel, *Appl. Phys. Lett.* 68, 1640 (1996).

86. T. Leyendecker, O. Lemmer, A. Jurgens, S. Esser, and J. Ebberink, *Surf. Coat. Technol.* 48, 253 (1991).

87. M. Murakawa, and S. Takeuchi, *Surf. Coat. Technol.* 49, 359 (1991).

88. J. Reineck, S. Soderbery, P. Eckholm, and K. Westergren, *Surf. Coat. Technol.* 57, 47 (1993).

89. K. Kanda, S. Takehana, S. Yoshida, R. Watanabe, S. Takano, H. Ando, and F. Shimakura, *Surf. Coat. Technol.* 75, 115 (1995).

90. S. Amirhaghi, H. S. Reehal, R. J. K. Wood, and D. W. Wheeler, *Surf. Coat. Technol.* 135, 126 (2001).

91. M. S. Raghuveer, S.N. Yoganand, K. Jagannadham, R.L. Lemaster, and J. Bailey, *Wear* 253, 1194 (2002).

92. H. Sein, W. Ahmed, M. Jackson, R. Woodwards, and R. Polini, *Thin Solid Films* 447, 455 (2004).

93. S. Silva, V. P. Mammana, M. C. Salvadori, O. R. Monteiro, and I. G. Brown, *Diamond Relat. Mater.* 8, 1913 (1999).

94. W. Ahmed, H. Sein, N. Ali, J. Gracio, and R. Woodwards, *Diamond Relat. Mater.* 12, 1300 (2003).

95. Z. Ma, J. Wang, Q. Wu, and C.Wang, *Thin Solid Films* 390, 104 (2001).

96. Z. Xu, A. Kumar, L. Lev, M. Lukitsch, and A.K. Sikder, *Mater. Res. Soc. Symp. Proc.* 843, T 3.33 (2005).

97. J. M. Lopez, V. G. Babaev, V. V. Khvostov, and J. M. Albella, *J. Mater. Res.* 13, 2841 (1998).

98. J. G. Buijnsters, P. Shankar, W. Fleischer, W. J. P. van Enckevort, J. J. Schermer, and J. J. ter Meulen, *Diamond Relat. Mater.* 11, 536 (2002).

99. J. G. Buijnsters, P. Shankar, W. J. P. van Enckevort, J. J. Schermer and J. J. ter Meulen, *Diamond Relat. Mater.* 13, 848 (2004).

100. D. M. Drory, and J. W. Hutchinson, *Science* 263, 1753 (1994).

101. K. Mallika, and R. Komanduri, *Wear* 224, 245 (1999).

102. H. Windischmann, and G.F. Epps, *J. Appl. Phys.* 69, 2231 (1991).

103. D. Rats, L. Bimbault, L. Vandenbulcke, R. Herbin, and K.F. Badawi, *J. Appl. Phys.* 78, 4994 (1995).

104. H. Windischmann, and K.J. Gray, *Diamond Relat. Mater.* 4, 837 (1995).

105. G.G. Stoney, *Proc. Roy. Soc. London.* A82, 172 (1909).

106. M.S. Raghuveer, S.N. Yoganand, K. Jagannadham, R.L. Lemaster and J. Bailey, *Wear* 253, 1194 (2002).

107. Z. Xu, L. Lev, M. Lukitsch, and A. Kumar, *Mater. Res. Soc. Symp. Proc. 890, Warrendale, PA,* 890, 0890 (2005).

108. A. Brenner, and S. Senderoff, *J. Res. Natl. Bur. Stand.* 42, 105 (1949).

109. S. Chowdhury, M.T. Laugier and J. Henry, *Int. J. Refractory Met. Hard Mater.* in press (2006).

110. H. J. C. V. Baranauskas, A.C. Peterlevitz and M. Fontana, *Surf. Coat. Technol.* 200, 2343 (2005).

111. P. Goudeau, L. Vandenbulcke, C. Met, M.I. De Barros, P. AndreAzza, D. Thiaudiere and M. Gailhanou, *Surf. Coat. Technol.* 200, 170 (2005).

112. A. V. Diniz, N. G. Ferreira, E. J. Corat and V. J. Trava-Airoldi, *Diamond Relat. Mater.* 13, 526 (2004).

113. A. F. Azevedo, R. C. Mendes de Barros, S. H. P. Serrano, and N. G. Ferreira, *Surf. Coat. Technol.* in press (2005).

114. N. G. Ferreira, E. Abramof, E. J. Corat, and V. J. Trava-Airoldi, *Carbon* 41, 1301 (2003).

115. J. G. Kim, and J. Yu, *Scripta Mater.* 39, 807 (1998).

116. J. Weide, Z. Zhang, P. K.Baumann, M. G. Wemnsell, J. Bernhold, and R. J. Nemanich, *Phys. Rev. B* 50, 5803 (1994).

117. F. J. Himpsel, J. A. Knapp, V. Vechten, and D. E. Eastman, *Phys. Rev. B* 20, 624 (1979).

118. C. Bandis, and B. B. Pate, *Appl. Phys. Lett.* 69, 366 (1996).

119. S.Bhattacharyya, O. Auciello, J. Birrell, J. A. Carlise, L. A. Curtiss, A. N. Goyette, D. M. Gruen , A. R. Krauss, J. Schlueter, A. Sumant, and P. Zapol, *Appl. Phys. Lett.* 79, 1441 (2001).

120. I.Sakaguchi, M. N. Gamo, Y. Kikuchi, E. Yasu, and H. Haneda, *Phys. Rev. B* 60, R2139 (1999).

121. M. Katagiri, J. Isoya, S. Koizumi, H. Kanda, *Appl. Phys. Lett.* 85 (2004).

122. G. W. John Harwood, and Colin W. Pouton, *Advanced Drug Delivery Reviews* 18, 163 (1996).

123. E. Wilkins, and P. Aanasov, *Med. Eng. Phys.* 18, 273 (1996).

124. M. Florescu, and C.M.A. Brett, *Talanta* 65, 306 (2005).

125. M. H. Gil, J. P. Sardinha, M. T. Vieira, M. Vivan, D. Costa, C. Rodrigues, F. M. Matysik, and A. M. Oliveria Brett, *Biotechnol. Tech.* 13, 595 (1999).

126. N. Matsumoto, X. Chen and G. S. Wilson, *Anal. Chem.* 74, 362 (2002).

127. G.M. Swain, and M. Ramesham, *Anal. Chem.* 65, 345 (1993).

128. K. Ohnishi, Y. Einaga, H. Notsu, C. Terashima, T.N. Rao, S.G. Park and A. Fujishima, *Electronchem. Solid-State Lett.* 5, D1 (2001).

129. R. Uchikado, T.N. Rao, D.A. Tryk and A. Fujishima, *Chem. Lett.* 5, 144 (2001).

130. W. M. Granger M.C., Xu J., Wang J., Hupter M., Hank A., Koppang M.D., Butler J.E., Lucazeau G., Mermoux M., and Strojek J.W.,, *Anal. Chem.* 73, 908 (2001).

131. M. C. Granger, M.Witek , J. Xu, J. Wang, M. Hupter, A. Hank, M. D. Koppang, J. E. Butler, G. Lucazeau, M. Mermoux, and J. W. Strojek, *Anal. Chem.* 73, 908 (2001).

132. G. Reach, and G.S. Wilson, *Anal. Chem.* 64, 381A (199).

133. Y. Show, M. A. Witek, P. Sonthalia, and G.M. Swain, *Chem. Mater.* 15, 879 (2003).

134. S. Bhattacharyya, O. Auciello, J. Birrell, J. A. Carlise, L. A. Curtiss, A. N. Goyette, D. M. Gruen , A. R. Krauss, J. Schlueter, A. Sumant, and P. Zapol, *Appl. Phys. Lett.* 79, 1441 (2001).

135. L. Werake, J. Story, M. Bertino, S. Pillalamarri and F. Blum, *Nanotechnology* 16, 2833 (2005).

136. N. S. S. S. Annapoorni, S. S. Pandey, and B. D. Malhotra, *J. Appl. Phys.* 74, 2109 (1993).

137. Y. Hayashi, T. Soga, *Tribology International* 37, 965 (2004).

138. N. Wang, Y. H. Tang, Y. F. Zhang, C. S. Lee, I. Bello, S. T. Lee, *Chem. Phy. Lett.* 299, 237 (1999).

139. S. T. Lee, N. Wang, C. S. Lee, *Mater. Sci. Eng. A* 286, 16 (2000).

140. M. H. Huang, Y. Wu, H. Feick, N. Tran, E. Weber, P. Yang, *Adv. Mater.* 13, 113 (2001).

141. J. Park, V. Q. Mocok, K. Peckova, J. J. Galligan, G. D. Fink, G. M. Swain, *Diam. Relat. Mater.* 15, 761 (2006).

142. J. M. Halpern, S. Xie, G. P. Sutton, B. T. Higashikubo, C. A. Chestek, H. Lu, H. J. Chiel, H. B. Martin, *Diam. Relat. Mater.* 15, 183 (2006).

143. P. W. May, R. Portman, K. N. Rosser, *Diam. Relat. Mater.* 14, 598 (2005).

144. X. Xiao, J. W. Elam, S. Trasobares, O. Auciello, J. A. Carlise, *Adv. Mater.* 17, 1496 (2005).

145. W. Shi, H. Peng, Y. Zheng, N. Wang, N. Shang, Z. Pan, C. Lee, S. T. Lee, *Adv. Mater.* 12, 1343 (2000).

146. J. Birrell, J. E. Gerbi, O. Auciello, J. M. Gibson, J. Johnson, J. A. Carlisle, *Diam. Relat. Mater.* 14, 86 (2005).

147. A. C. Ferrari, J. Robertson, *Phys. Rev., B* 61, 14095 (2000).

148. K. Okada, K. Kimoto, S. Komatsu, S. Matsumoto, *J. Appl. Phys.* 93, 3120 (2003).

149. J. Stohr, *NEXAFS Spectroscopy, Springer Series in Surface Sciences* (Springer, Heidelberg, 1996).

150. W. P. Kang, J. L. Davidson, Y. M. Wong, K. Holmes, *Diam. Relat. Mater.* 13, 975 (2004).

ABOUT THE AUTHOR

Zhenqing Xu was born in Shanghai, P.R. China. He received his Master of Science degree in Mechanical Engineering from the University of South Florida, Tampa, FL, USA in 2003. His thesis was titled “modification and optimization of MPECVD system for diamond growth”. He will be receiving his Ph.D. in Mechanical Engineering in August 2007 with dissertation title “Synthesis, characterization and applications of CVD micro- and nanocrystalline diamond films”. Prior to his graduate study, he completed his B.E. degree in Mechanical Engineering from Shanghai Jiaotong University, Shanghai, P.R. China. As the first author, Mr. Xu has published 5 journal articles, either published or under communication, 2 book chapters, and 3 conference papers. The author has been an active member in the Materials Research Society since 2003.